THE UNIVERSITY OF CHICAGO

ON THE GENERATION OF GRAVITY WAVES IN ASTROPHYSICAL ENVIRONMENTS

A DISSERTATION SUBMITTED TO
THE FACULTY OF THE DIVISION OF THE PHYSICAL SCIENCES
IN CANDIDACY FOR THE DEGREE OF
DOCTOR OF PHILOSOPHY

DEPARTMENT OF PHYSICS

BY
ALEXANDROS ALEXAKIS

CHICAGO, ILLINOIS
APRIL 5, 2004

Dedicated to the memory of my godfather, **Georgios Saridakis**,

who passed away a few months before this work was completed.

ABSTRACT

Typical ejecta of classical nova explosions (thermonuclear runaways of accreted H/He envelopes on the surfaces of a white dwarfs) are enriched in CNO and Ne, elements that are not product of the nuclear reactions involved. We investigate how this enrichment might originate from mixing of the white dwarf material (mainly composed of CNO&Ne) to the He/H envelope, due to large-scale flow and gravity wave interaction, prior to the explosion. In our simplified mixing model shear flow amplifies the waves, which eventually form cusps and break. This wave breaking injects a spray of C/O into the superincumbent H/He forming a layer with mixed material. Material from this layer are mixed through out the white dwarfs envelope by convective motions. We perform an extensive study of the interaction shear flows with interfacial gravity modes by (a) examining the stability properties of such flows using linear theory, (b) investigating the evolution of marginally unstable modes using weakly non-linear theory and (c) using two-dimensional numerical simulations to follow the non-linear evolution of the system. Our results allow us to formulate a quantitative expression for the amount of C/O per unit area that can be entrained into the H/He. The fraction of the envelope that is enriched depends on the horizontal distribution of shear velocity and the density contrast between the C/O white dwarf and the H/He layer. Using this parameterization to model the mixed mass, we then perform several one-dimensional Lagrangian calculations of an accreting white dwarf envelope. Our final results indicate that the envelope can be enriched by $\sim 25\%$ of C/O by mass (consistent with that observed in some ejecta) for shear velocities, over the surface, with Mach numbers ~ 0.4.

ACKNOWLEDGEMENTS

I would like to thank all the people that contributed to the completion of this work. In particular I would like to thank my advisor Robert Rosner for his help and suggestions through out the progress of this work. I would like to thank Yuan-Nan Young for helping me with the linear and weakly non-linear part of this work. The help of Alan Calder, Jonathan Dursi and Bruce Fryxel with the numerical part of this work is greatly appreciated. I would also like to thank James Truran, Edward Brown and Alex Heger for helping me with the astrophysical part of this work.

TABLE OF CONTENTS

LIST OF FIGURES

LIST OF TABLES

CHAPTER 1

INTRODUCTION

1.1 An astrophysical problem

Classical novae are a manifestation of thermonuclear runaways in accreted hydrogen shells on the surfaces of white dwarf stars in close binary systems [1]. Compelling observational data indicate that the material ejected by some classical novae can be significantly enriched in C, N, O, and Ne, by 30% by mass or more ([1, 2]). Since the abundance of CNO catalysts constrains the rate of energy release, such high levels of CNO enrichment are required in the fastest novae [3], for which the hydrogen burning reactions (via the CNO cycle) increase the entropy of the envelope faster than it can adjust. It was recognized early that if some of the underlying white dwarf matter[1] could be mixed into the accreted envelope prior to the final stages of the thermonuclear runaway, then the explosion would be more energetic and the ejecta more enriched in CNONe elements [4]. One-dimensional models that best reproduce observations typically accrete material "seeded" with a super-solar composition [5, 6].

The question of how the accreted envelope is enriched has challenged theory for several decades [2]. For very slow accretion ($\leq 10^{-10} M_{\odot}\,\mathrm{yr}^{-1}$), the downward diffusion of H into the underlying C/O or O/Ne layers [7, 8] could trigger ignition in the H diffusive tail and drive convective mixing of heavy elements into the envelope during the early stages of runaway. It is unclear, however, whether there is time at higher accretion rates for this process to be relevant.

The general problem of shear mixing was considered by many [9, 10, 11], but to date no self-consistent calculations of these effects have been performed. Kippenhahn

1. By "white dwarf," we mean the predominantly C/O substrate; we shall refer to the accumulated H/He layer as the "atmosphere" or "envelope."

& Thomas (1978) [9] considered shearing from differential rotation in the envelope and estimated the amount of mass mixed by assuming that the envelope was marginally stable according to the Richardson criterion. MacDonald (1983) [10] considered non-axisymmetric perturbations and the resulting redistribution of matter and angular momentum. Fujimoto (1988) [11] emphasized the role of barotropic and baroclinic instabilities in transporting angular momentum through the envelope. A variation on this was envisaged by Sparks & Kutter (1987) [12] and [13] (1989), who suggested that convection just prior to the runaway would transport angular momentum inward and lead to a large horizontal shear above the C/O white dwarf. However, all these estimates were based on linear-theory arguments and assumptions that cannot be justified a priori.

The possibility of mixing via convective overshoot was first considered by Woosley (1986) [14]. Numerical simulations of convective penetration and mixing at the core-envelope interface have been carried out in both two dimensions [15, 16] and three [17]. From comparisons of two- and three-dimensional simulations and a careful resolution study, Kercek et al. (1998,1999) [16, 17] concluded that convective penetration would not significantly enrich the accreted envelope. In particular, the resolution studies showed *less* mixing as grid resolution was increased. This can be readily understood if the boundary layer between the stellar surface and the accreted (convecting) envelope is laminar: in that case, since diffusivity in these simulations is numerical, increased resolution would lead to *less* mixing as the grid resolution is increased. The above argument depends entirely on the assertion that the boundary layer is laminar: if it were turbulent instead, mixing is expected become independent of the viscosity and diffusivity. However, presently attainable numerical resolutions cannot resolve a turbulent boundary layer while capturing the large scale astrophysical flows. For this reason, we have recently re-examined the physics of boundary layer shear flow

mixing[18, 19, 20, 21, 22]. The question we sought to answer is whether we can understand the physics involved in a turbulent boundary layer and model its mixing properties in order to feed back the larger scale numerical simulations.

1.2 An oceanographic problem

Before examining directly the astrophysical problem it is worth looking at a similar problem in oceanography, ie. the mixing of vapor from the ocean in the atmosphere. It is well known [23] that this process of mixing is largely governed by the formation and breaking of interfacial gravity waves that have been amplified by the wind. The generation of surface waves by winds has been a problem under study for well over a century. Helmholtz [24] and Lord Kelvin [25] investigated the stability of fluid interfaces using a simple model of a step function wind shear profile. It was noticed early on that the Kelvin-Helmholtz theory (from now on KH) predicted a minimum velocity of the wind for the instability to occur that did not agree with observations in the ocean [26]. This puzzle was resolved with the work of Miles (1957)[27], which showed that waves can be amplified by a resonant mechanism. Detailed calculations of linear theory, using a more realistic wind profile than KH, show that there is an influx of energy from the wind to the gravity wave as long as there is a height at which the wind velocity equals the phase velocity of the gravity wave [27, 28]. At this height, the linear eigenvalue problem is singular and a layer known as the critical layer is formed. The formation of this critical layer allows the pressure perturbation to be in phase with the slope of the wave rather than its trough, thus driving the wave unstable. Vortices therefore that travel with the same velocity as the wave (resonant condition) amplify it. The resulting minimum velocity to excite gravity waves is smaller by a factor of $\sqrt{\rho_1/\rho_2}$ than the minimum velocity obtained by KH

theory and is in much better agreement with experiments and observations.

Although, the generation of gravity waves seems to be well understood in oceanography, their non-linear evolution is a problem of on-going research. Of particular interest is answering the questions, how the presence of waves change the wind profile, what is the exact process that leads to wave breaking, and what is the resulting amount of vapor mixed. The different time-scales and length scales involved in such a system makes the answer to these questions a challenging one.

Returning to the astrophysical problem it is clear that in order to understand mixing from a shear boundary layer in this terrestrial environment the physics of the critical layer instabilities, like in the oceanography case, have to be included. However the oceanographic work was largely confined to the parameter regime characteristic of the water/air interface; (ie. very small density ratio), while in the astrophysical problem we are considering the density ratio is of order one. In order therefore, to model correctly the the mixing, we need to perform a systematic study of the critical layer instability.

1.3 A mixing Model

Before investigating the properties of shear boundary layer mixing we describe a simplified model to guide our research. Consider a 'wind' originating either from the accretion process, or from convection at the base of the envelope. The interaction of the wind with the gravity waves will lead to the formation of a mixed layer at the base of the envelope. Material from this mixed layer can spread out through out the envelope by penetrating convecting roles. Figure 1.1 demonstrates this model.

Let us further assume that the mixing properties of a turbulent boundary layer are known, and that turbulent mixing results on a time scale $\tau_{M.L.}$ in a layer of thickness

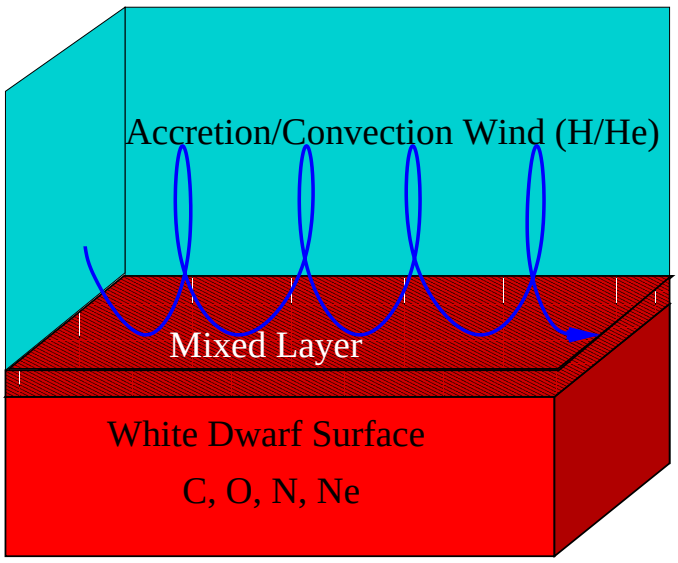

Figure 1.1: A diagram describing the mixing model.

$\lambda_{\rm M.L.}$ in which an amount of $m_{\rm M.L.}$ of mass from the lower fluid (C/O) has been mixed. Additional mixing is prevented by the stabilization of the flow due to the additional density (chemical) stratification. The time scale on which the boundary mixing layer is swept out by large scale flows (i.e. a penetrating convective roll), is just $\tau_{\rm L.S.} \sim \Lambda/U_{\rm L.S.}$ where Λ and U are the characteristic length scale and velocity of the large-scale circulation. If the time scale $\tau_{M.L.}$ is smaller than the "sweep-out time" $\tau_{\rm L.S.}$ then the rate of mixing is going to be controlled by the large scale flows and is going to be given by $\dot{M}_{C/O} = m_{\rm M.L.}/\tau_{\rm L.S.}$. If on the other hand $\tau_{M.L.}$ is larger than $\tau_{\rm L.S.}$ the rate of mixing is going to be controlled by the boundary layer mixing rate, $\dot{M}_{C/O} = m_{\rm M.L.}/\tau_{\rm M.L.}$. The accretion process itself lasts for $\tau_{acr} \sim 10^4$ years while convection starts a few months before the runaway (τ_{conv}). We would like therefore to know if in this time (τ_{acr} or τ_{conv}) a sufficient amount of C/O has been mixed. If for example convection is driving the mixing the total amount of mass mixed would

be:

$$M_{C/O} = \dot{M}_{C/O}\tau_{conv} = \tau_{conv} m_{\text{M.L.}} / \min\{\tau_{\text{L.S.}}, \tau_{\text{M.L.}}\})$$

If therefore we could measure $m_{\text{M.L.}}$ and $\tau_{\text{M.L.}}$ from numerical simulations of a turbulent boundary layer and $\tau_{\text{L.S.}}$ from numerical simulations of the large scale flows we can give an estimate of the amount of mass mixed by shear mixing.

CHAPTER 2

LINEAR THEORY

2.1 Introduction

Linear theory is always to be examined first in the study of an instability. Although it is not informative about the fully nonlinear structures the system develops, it imposes constraints on the spectrum of the unstable modes and determines the time scales involved given by the linear growth rate. The stability of fluid interfaces in the presence of shear flows has been studied for almost half a century; and was largely motivated by the problem of accounting for observations of surface water waves in the presence of winds. As early as the 1950's, it was realized that classical Kelvin-Helmholtz instability [29] could not account for the observed water waves (cf. [27, 28]), and efforts were initiated to study the full range of possible unstable modes via which interfaces such as represented by the water/air interface could become unstable. By the early 1960's, the basic mechanism was understood, largely on the basis of work by Miles [30, 31, 32] and Howard [33]: It was discovered that interfacial waves for which gravity provided the restoring force (e.g., waves that can be identified with so-called deep water waves) can be driven unstable via a resonant interaction with the ambient wind; this work was also one of the first applications in which resonant (or critical) layers played an essential role in both the physics and the mathematics. Work carried out at that time showed that the precise form of the vertical wind shear profile was critical to the nature of the instability; typically, it was assumed that the wind immediately above the water surface could be characterized by a logarithmic profile of the form

$$U(z) = U_o + U_{\log} \log(y/\delta + 1) \ , \tag{2.1}$$

where U_o is the velocity jump (if any) at the water/air interface, y is the vertical coordinate (with $y = 0$ marking the initial water-air interface), and δ is the characteristic scale length of the shear flow in the air.[1] The idea was then to demonstrate that surface gravity waves whose phase speed is given by $c = \sqrt{g\lambda\mathcal{A}_t}$ (g the gravitational acceleration, λ the perturbation mode wavelength, and $\mathcal{A}_t \equiv (\rho_2 - \rho_1)/(\rho_2 + \rho_1)$ the Atwood number for a density interface between fluids of density ρ_1 [upper fluid] and ρ_2 [lower fluid], with $\rho_1 < \rho_2$) can couple to this wind profile at a height z where $c \sim U(z)$. At the time, it was not possible to construct a self-consistent description of the problem, such that a logarithmic wind profile automatically emerged from the analysis; and much of subsequent work has focused on establishing the nature of this wind shear profile (e.g., [34]). Finally, we note that these studies have since been applied to a number of other contexts, including especially shear flows in atmospheric boundary layers, where they have been extensively expanded, including into the weakly compressible regime [35].

However, the earlier work, motivated by oceanography was largely focused on the case of very large density differences between the two fluids separated by an interface, and primarily considered the fully incompressible case (the weakly compressible case has been considered by [35]). Our aim is therefore to generalize to arbitrary density ratios, and to the compressible case.

1. Such velocity profiles are commonly observed in the boundary layer of winds blowing over the surface of extensive bodies of water; cf. Miles (1957).

2.2 Formulation

2.2.1 The general problem

We consider a two-dimensional flow with x the horizontal direction and y the vertical. The system consists a layer of light fluid (density ρ_1) on top of a layer of heavy fluid (density ρ_2). In most of our analysis ρ_1 and ρ_2 are constant in each layer, and in the most general scenario both layers can be stratified (densities are functions of y). The two layers are separated by an interface given by $y = h(x;t)$, which initially is taken to be flat ($y = h(x;0) = 0$). The upper layer (ρ_1) is moving with velocity U(y) in the x direction parallel to the initial flat interface, while the lower layer (ρ_2) remains still.

As already mentioned, the instability of such stratified shear flow has been investigated (cf. [27, 33]), albeit under limited physical circumstances. We study this problem in full generality, allowing for a variety of effects (including broad ranges in the values of the Atwood number/gravity and in compressibility) with the motivation that one can establish the role of the relevant instabilities under more general astrophysical circumstances.

A wind (shear flow) is assumed to flow only in the layer of light fluid (ρ_1) and is zero in the heavy fluid (ρ_2). Within each layer, the governing equations are the continuity equation

$$\partial_t \rho + \nabla \cdot (\rho \mathbf{u}) = 0, \tag{2.2}$$

and the two-dimensional Euler equation

$$\rho \partial_t \mathbf{u} + \rho \mathbf{u} \cdot \nabla \mathbf{u} = -\nabla P + \rho \mathbf{g}. \tag{2.3}$$

The equation of state closes the system, which is expressed in dynamical terms:

$$(\partial_t + \mathbf{u}\cdot\nabla)\mathrm{P} = \frac{\mathrm{DP}}{\mathrm{D}t} = \frac{\gamma \mathrm{P}}{\rho}\frac{\mathrm{D}\rho}{\mathrm{D}t}, \tag{2.4}$$

where γ is the polytropic exponent. The background density and pressure are in hydrostatic equilibrium, $\partial_y P_o = -\rho_o g$. The basic state is then defined by a shear flow $\mathrm{U}(y)$ in the upper layer, and hydrostatic pressure (P_o) and density profiles (ρ_o). We perturb around this basic state

$$\mathbf{u} = \mathrm{U}(y)\mathbf{i} + \mathbf{u}', \quad \rho = \rho_o(y) + \rho', \quad \mathrm{P} = \mathrm{P}_o(y) + p', \tag{2.5}$$

and study the growth of the perturbations (primed variables). From equation 2.4, the density and pressure perturbations satisfy the relation.

$$\frac{\mathrm{D}p'}{\mathrm{D}t} = c_s^2\frac{\mathrm{D}\rho'}{\mathrm{D}t} + w'(g\rho_o + c_s^2\partial_y\rho_o), \tag{2.6}$$

where w' is the vertical component of the perturbation velocity, g is the gravitational acceleration, and $c_s = \sqrt{\gamma P_o/\rho_o}$ is the sound speed for the background state. Upon expanding the perturbations in normal modes $e^{ik(x-ct)}$, we obtain the linearized equations in the perturbation quantities (where we have dropped the primes for convenience):

$$\begin{aligned}
ik(\mathrm{U}-c)u \quad &+wU_{,y} \quad &&= -ik\rho_o^{-1}p\,,\\
ik(\mathrm{U}-c)w \quad & \quad &&= -\rho_o^{-1}p_{,y} - \rho_o^{-1}g\rho\,,\\
ik(\mathrm{U}-c)\rho \quad & \quad &&= -\rho_o(iku + w_{,y}) - w\rho_{o,y}\,,\\
ik(\mathrm{U}-c)p \quad &-wg\rho_o \quad &&= c_s^2\left(ik(U-c)\rho + w\rho_{o,y}\right)\,.
\end{aligned} \tag{2.7}$$

Here we have used the standard notational device of comma-prefaced subscripts

to denote partial derivatives, e.g.,

$$f_{,x} \equiv \partial f / \partial x \, .$$

The above equations 2.6 form an eigenvalue problem for the complex number c. One immediately sees that the incompressibility condition $\nabla \cdot \vec{u} = 0$ can be obtained by taking the limit $c_s \to \infty$. Our problem simplifies greatly with this assumption. Therefore we first present our results for the incompressible case, and then examine how compressibility modifies the stability properties.

2.2.2 The incompressible case

For the incompressible case our analysis simplifies if we define a stream function Ψ such that $u = \partial_y \Psi$ and $w = -\partial_x \Psi$. The 2-D Euler 2.3 equation thus reads

$$\partial_t \nabla^2 \Psi - \Psi_{,x} \nabla^2 \Psi_{,y} + \Psi_{,y} \nabla^2 \Psi_{,x} = 0, \quad y \neq h. \tag{2.8}$$

The total stream function $\Psi = \Psi_0 + \psi$ consists of a background stream function $\Psi_0 = \int_0^y \mathrm{U}(z) dz$ and a perturbation $\psi = \phi(y) e^{ik(x-ct)}$. Ignoring the non-linear terms in ψ in equation 2.2.2 We obtain the well-studied Rayleigh equation,

$$\phi_{,yy} - \Big(k^2 + \frac{\mathrm{U}_{,yy}}{\mathrm{U} - c}\Big)\phi = 0. \tag{2.9}$$

The boundary conditions at the interface for the continuity of the normal component of the velocity and pressure are:

$$(\mathrm{U} - c)\hat{h} - \phi^{\pm} \;\; = \;\; 0, \tag{2.10}$$

$$\Delta[\rho_i((\mathrm{U}-c)\phi_{,y}-\mathrm{U}_{,y}\phi)]+g\hat{h}(\rho_1-\rho_2), \tag{2.11}$$

where Δ indicates the difference across the interface and $\tilde{h}$ is the amplitude of the perturbed interface, $h=\hat{h}e^{ik(x-ct)}$.

2.2.3 The compressible case

When the sound speed c_s is comparable to the background shear flow and/or the density stratification is non-negligible on the scales of interests the incompressible flow approximation is not valid and the full set of equations 2.7 needs to be considered. By eliminating ρ and u we obtain the following equations:

$$\begin{aligned}\rho_o(k^2U_G^2+gk_g+gk_s)w &= ikU_G(\partial_y+k_g)p\,,\\ ik^2(U_G^2/c_s^2-1)p &= \rho_o k(k_gU_G+U_{G,y}-U_G\partial_y)w\,,\end{aligned} \tag{2.12}$$

where $U_G=U-c$ is the Galilean-transformed velocity in the reference frame of the wave, $k_s=\rho_{o,y}/\rho_o$ is the inverse stratification length scale, and $k_g=g/c_s^2$. We further simplify the equations by applying the transformation [36]

$$p=f^{-1}\tilde{p},\quad w=iU_Gqf,\quad \tilde{\rho}_o=\rho_of^2\quad\text{with}\quad f=e^{\int_0^y k_g(z)dz}.$$

Equations 2.12 are then rewritten in terms of these new variables as follows:

$$\begin{aligned}\tilde{\rho}(k^2U_G^2+gk_g+gk_s)q &= k\tilde{p}_{,y},\\ k^2\left(1-U_G^2/c_s^2\right)\tilde{p} &= \tilde{\rho}_okU_G^2q_{,y},\end{aligned} \tag{2.13}$$

which can be combined to give [35]

$$\partial_y\left(\frac{\tilde{\rho}_oU_G^2q_{,y}}{1-U_G^2/c_s^2}\right)-\tilde{\rho}_o\Big[k^2U_G^2+g(k_s+k_g)\Big]q=0\,. \tag{2.14}$$

We re-write the above equation into canonical form. The resulting equation is similar to the Rayleigh equation for the incompressible flow, except for an additional stratification term $-g(k_s + k_g)/\tilde{\mathrm{U}}_G^2\phi$:

$$\phi_{,yy} - \left[\kappa^2 + g\tilde{\rho}_o\frac{k_s + k_g}{\tilde{\mathrm{U}}_G^2} + \frac{\tilde{\mathrm{U}}_{G,yy}}{\tilde{\mathrm{U}}_G}\right]\phi = 0 \tag{2.15}$$

where $\kappa^2 = k^2\left(1 - U_G^2/c_s^2\right)$, $\tilde{\mathrm{U}}_G = kU_G\sqrt{\tilde{\rho}_o}/\kappa$ and $\phi = q\tilde{\mathrm{U}}_G/k$. It can be shown that the stratified Rayleigh equation can be recovered by taking the limit of $c_s \to \infty$.

$$\partial_y^2\phi - \left[k^2 + g\frac{k_s}{\mathrm{U}_G^2} + \frac{\partial_y^2(\mathrm{U}_G\sqrt{\rho_o})}{\mathrm{U}_G\sqrt{\rho_o}}\right]\phi = 0 \tag{2.16}$$

Furthermore, we recover the unstratified Rayleigh equation in the same limit, if $k_s + k_g = 0$ (which corresponds to an adiabatic atmosphere, as we will show later on). Finally, the boundary conditions at the interface are expressed in terms of $\tilde{\mathrm{U}}_G$ and ϕ:

$$q = \frac{\phi^+}{\mathrm{U}_G^+} = \frac{\phi^-}{\mathrm{U}_G^-} = \hat{h} \tag{2.17}$$

using the continuity of q and integrating 2.14 across the interface we obtain

$$\Delta\left[\tilde{U}_G\phi_{,y} - (\tilde{U}_{G,y})\phi - g\tilde{\rho}\phi/\tilde{\mathrm{U}}_G\right] = 0\,. \tag{2.18}$$

2.2.4 Wind profiles

In general, it is not trivial to determine the wind profile: strictly speaking, the wind profile should be determined as part of the solution of the evolution equation for the wind shear interface. However, it has been customary to simplify the problem by assuming an a a priori analytical form for the wind profile, and to use this in order

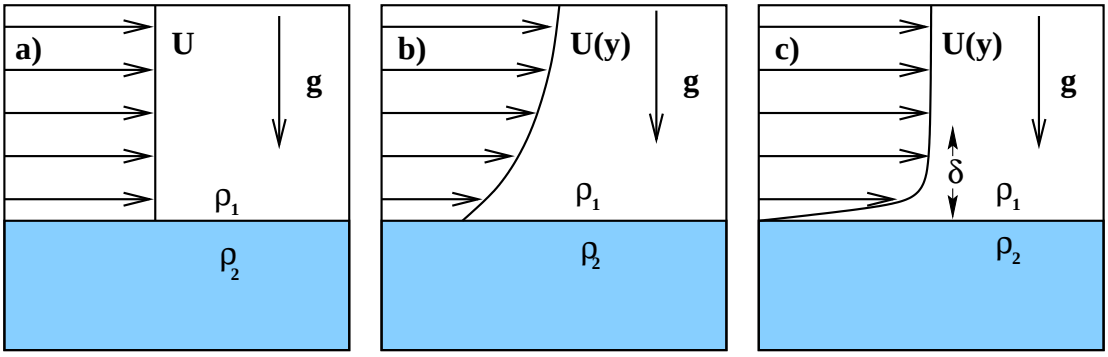

Figure 2.1: Different wind profiles assumed for the generation of gravity waves. (a) Kelvin-Helmholtz step function wind profile, (b) logarithmic wind profile with discontinuity, (c) a bounded wind profile.

to study the stability properties of the interface; thus, Miles [27] used a logarithmic wind profile from turbulent boundary layer theory to model the wind profile in the air over the ocean. In this example, the turbulence level in the wind is simply defined by the scale height of the wind profile, which in turn simply depends on how "rough" the boundary is.

In our formulation we shall also assume the wind profile to be of simple form, and scale distance with respect to the length scale of the wind boundary layer. In order to explore the sensitivity of our results to the nature of this wind boundary layer, we will examine two different kinds of wind profiles: the first is the logarithmic wind profile $\mathrm{U}(y) = U_0 + U_{\log} \log(y/\delta + 1)$, which is derived from turbulent boundary layer theory for the average flow above the sea surface; the second kind is given by bounded wind profiles like $\mathrm{U}(y) = U_{\max} \tanh(y/\delta)$ or $\mathrm{U}(y) = U_{\max}(1 - \exp(-y/\delta))$, which have the more realistic feature of reaching a constant finite flow speed above the interface. A sketch of the wind profiles are shown in figure 2.1. Panel (a) shows the wind profile envisioned by Kelvin and Helmholtz, panel (b) shows a logarithmic wind profile with a velocity jump at the interface and panel (c) shows a bounded wind profile. We

note here, that in oceanography the exact shape of the wind profile can be measured and theoretical predictions of the wave growth rates can be directly compared with observations, thus a logarithmic profile that fits the wind profile measurements is more relevant. On the other hand for the astrophysical problem only estimates of the maximum velocity of the wind can be made and therefore information about the instability of a bounded wind profile is of more practical use.

2.3 Linear analysis: incompressible case

We start with the stability analysis of the incompressible case with constant densities in the two layers. The fluid is described by the Rayleigh equation 2.9 within each layer. We solve the following equation in each layer:

$$\phi_{,yy} - \Big(k^2 + \frac{U_{,yy}}{U-c}\Big)\phi = 0, \qquad \phi|_{y\to\pm\infty} = 0, \tag{2.19}$$

with boundary condition at $y = 0$ (including the surface tension term)

$$\rho_2 k c^2 - \rho_1\Big[(U-c)^2\phi_{,y} - (U-c)U_{,y}\Big] - g(\rho_2 - \rho_1) - \sigma k^2 = 0, \tag{2.20}$$

where σ is the surface tension and we have normalized ϕ by setting $\phi|_{y=0} = 1$.

We scale lengths by δ, the characteristic length of the wind profile [2] and the velocity by the reference velocity $U_{\log}$ or $U_{\max}$. The dimensionless equation thus reads

$$\phi_{,yy} - \Big(K^2 + \frac{V_{,yy}}{V-C}\Big)\phi = 0, \quad \phi|_{y=0} = 1, \quad \phi|_{y=\infty} = 0; \tag{2.21}$$

2. In oceanography, such a length scale is referred to as the "roughness" of the wind profile.

and the boundary condition at the interface now becomes

$$KC^2 - r\Big[(V_0 - C)^2\phi_{,y} - (V_0 - C)V_{,y}\Big] - G(1-r) - \mathcal{T}K^2 = 0. \tag{2.22}$$

where $C = c/U_1$, $K = k\delta$, $G = g/\mathrm{U}_1^2 a$, $V_0 = \mathrm{U}(0)/\mathrm{U}_1$, $r = \rho_1/\rho_2$, and $\mathcal{T} = \sigma/(\delta U_1^2 \rho_2)$.

For a given wind profile, the system then is characterized by the four parameters $(V_0, G, r, \mathcal{T})$. We are mainly going to focus on the case $V_0 = 0$ and refer the reader to [19] for the $V_0 \neq 0$ case. Parameter G is a measure of the wind strength (G is related to the Froude number as $G = F^{-2}$). In the case of accretion flow on the surface of a white dwarf $G \sim 1$, while in the case of oceanic waves driven by winds, $0.01 < G < 1.0$. Table 2.1 lists the values of G for a variety of physical conditions.

The aim of our linear analysis then is to find the value of C in the complex plane as a function of these 4 parameters, and to establish the stability boundaries in the space $(K, G, r, \mathcal{T})$; note that in our convention, $\Im\{C\} > 0$ implies instability (where $\Im\{\cdot\}$ refers to taking the imaginary part).

2.3.1 Kelvin-Helmholtz and Critical Layer instability

First we give a short summary of the KH instability that can be obtained in our present setup by setting $U_1 = 0$ (see figure 2.1) . In this setup the phase velocity of the waves is given by [29]:

$$c = \frac{\rho_1}{\rho_1 + \rho_2} U \pm \sqrt{\frac{g}{k}\left(\frac{\rho_2 - \rho_1}{\rho_1 + \rho_2} + \frac{k^2\sigma}{g(\rho_1 + \rho_2)}\right) - \frac{\rho_1\rho_2}{(\rho_1 + \rho_2)^2}U^2}. \tag{2.23}$$

Instability is present if the argument inside the square root is negative. In the absence of surface tension the unstable wave numbers satisfy:

$$k > g(\rho_2^2 - \rho_1^2)/(U^2 \rho_1 \rho_2) \tag{2.24}$$

while in the presence of unstable wave numbers we have instability if

$$U_o^2 > 2\frac{\rho_1 + \rho_2}{\rho_1 \rho_2}\sqrt{\sigma g(\rho_2 - \rho_1)} \tag{2.25}$$

As we show next the resonant instability has a much different behavior. We first make some general remarks about the set of equations 2.21 - 2.22 are required. We observe that in the inviscid limit, if C is an eigenvalue, then so is C^*; therefore we will have a stable wave only if $\Im\{C\} = 0$. If that is the case, then at the height where $V_c \equiv V(y_{cr}) = C$ (assuming such a height exists) the Rayleigh equation has a singularity; this location $y = y_{cr}$ is called the critical layer, and is well-discussed in the literature [38, 37] The existence of such a critical layer is crucial for the presence of instability. One can prove (A.1) that our system can be unstable only if $C_r \equiv \Re\{C\} \leq V_{\max}$ and further more $\Re\{C\}^2 + \Im\{C\}^2 \leq V_{\max}^2$. This last result is known as Howard's semi-circle theorem [33] and it was proven for smooth velocity and density profiles, however it is easy to show that it holds for our case too (A.1).

The solutions of 2.21 near the critical layer for small or zero C_i have a singular behavior. The solution close to the point where $y = y_{cr}$ can be given in terms of the two Frobenius solutions:

$$\phi_a = z + \left(\frac{V_{,yy}}{2V_{,y}}\right)_{cr} z^2 + \ldots , \tag{2.26}$$

$$\phi_b = 1 + \left(\frac{k^2}{2} + \frac{V_{,yyy}}{2V_{,y}} + \frac{V_{,yy}^2}{V_{,y}^2} \right)_{cr} z^2 + \ldots + \left(\frac{V_{,yy}}{V_{,y}} \right)_{cr} \phi_a(z) \log |z| \ , \qquad (2.27)$$

where $z = y - y_{cr}$ (subscript cr means "evaluated at the critical point"). The singular behavior appears in the first derivative of ϕ_b. The singularity is removed either because $C_i \neq 0$, in which case the Frobenius solutions have the same form but y_{cr} is now complex (so z never becomes zero); or because viscosity becomes important in this narrow region, in which case the inner solution can be expressed in terms of generalized Airy functions [38]. In either case, the basic result is that there is a phase change across the critical layer, by which we mean that if $\phi = a\phi_a + b\phi_b$ is the solution for the stream function above the critical layer, then the solution below would be $\phi = (a + i\pi b)\phi_a + b\phi_b$ in the previous formula. Physically this means that the perturbation wave above the critical layer is not in phase with the wave below this layer. Moreover, when we apply the boundary conditions at the interface, since $\partial_y \phi|_0$ is now in general complex, the solution of equation 2.22 will give a complex value of C. That is, the pressure gradient reaches minimum value not on top of the crests, but rather in front of the crests, where gravity does not act as effectively as a restoring force. In particular, the destabilizing force is now non-zero at the nodes of the boundary displacement field (i.e., where $h = 0$), where the gravitational restoring force vanishes, but where the vertical velocity of the interface is maximum; thus, the forcing resembles pushing a pendulum at its point of maximum velocity but minimum displacement.

Having discussed the physical mechanisms for destabilization, we now turn to the implications for our choices of initial wind profiles. If we use the logarithmic wind profile, we obtain unstable waves for all wavenumbers because $\log(y + 1)$ is an unbounded function, therefore a point y where $C_r = V(y)$ exists for every value of C_r. This however is not true for the tanh wind profile. Because waves with $C_r > V_{\max}$ are

stable and C_r (in the absence of surface tension) is a decreasing function of K, there must be a lower bound on K, K_{min}, so that waves with $K < K_{min}$ are stable, and unstable otherwise. The value of K_{min} in general will depend on the exact form of the wind profile. In appendix A.2 we find the exact value of K_{min} for a wind profile of the form $V = 1 - e^{-y}$,

$$K_{min} = \frac{G(1-r) + r - r\sqrt{(G(1-r)+r)^2 + (1-r^2)}}{1-r^2} \quad . \tag{2.28}$$

The stability bound comes from the modes that have phase velocity $C = 1$ (ie. $c = U_1$), in which case the solution of equation (2.36) becomes $\phi = e^{-\kappa y}$ with $\kappa = \sqrt{1+K^2}$. Applying the boundary conditions leads to the result above 2.28. We note that, unlike the Kelvin-Helmholtz case, in the limit $r \to 0$, K_{min} remains finite and equal to G (however, the growth rate goes to 0 linearly with r i.e., $KC_i \sim r$); this confirms that for small density ratios CL-modes dominate. Finally by writing the wind profile in its dimensional form $U = U_1(1 - e^{-y/\delta})$ and taking the limit $\delta \to 0$ (which takes the wind profile to the limiting form of a step-function, $U = U_1$ for $y > 0$ and $U_1 = 0$ otherwise) we get $k_{min} = g(1-r)/U^2$ which is different from the result Kelvin-Helmholtz instability gives. This stability boundary illustrated in figure 2.2 where it is compared with the one for KH instability. The unstable modes can be further restricted if we assume the presence of surface tension or magnetic fields. This will lead to the additional term $\mathcal{T}K^2$ in boundary condition at the interface, where $\mathcal{T} = \sigma/(\rho_2 U_1^2 l)$ and σ is the surface tension[3]. Then the unstable modes lie in the region $K_{min} \leq K \leq K_{\max}$, where K_{min} and $K_{\max}$ are given by the positive real

3. We note that a magnetic field whose direction is aligned with the interface will have the same effect as surface tension, with $\sigma(K) = B^2/(2\pi\mu K)$ [29].

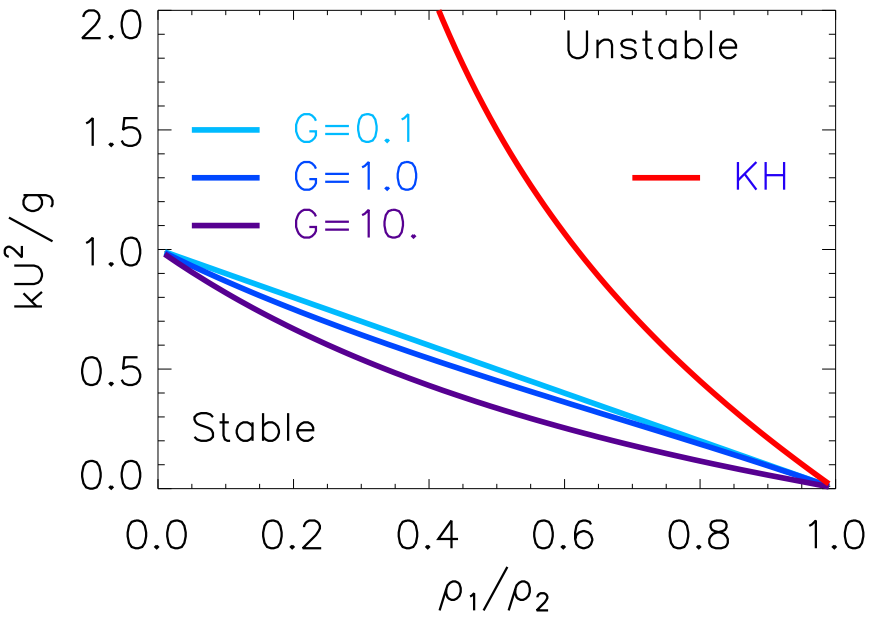

Figure 2.2: Stability diagram in the $r = \rho_1/\rho_2, k$ space for the KH-instability (red line) and for the critical layer instability for three different values of G (blue lines). Note that we scaled k with the length scale U_1^2/g which is independent of δ so that the boundaries of the two instabilities can be compared.

solutions of

$$K + r\sqrt{1+K^2} - (G(1-r) + r + \mathcal{T}K^2) = 0\,. \tag{2.29}$$

Furthermore, there is a value of $\mathcal{T}$ below which the above equation has no positive real solutions, and therefore no unstable modes exist. The physics behind these bounds is simple: In order for a mode to become unstable for the above wind profile, the phase velocity of the wave must lie in the range $0 < c < U_{\max}$. With the inclusion of surface tension, the phase velocity is not monotonically decreasing with K, but rather increases without bound for large K. This leaves only a finite region in K space with phase velocity smaller than $U_{\max}$; moreover, if the surface tension is large enough, the minimum phase velocity is larger than $U_{\max}$, and therefore no unstable mode exists. For large $G \gg 1$, which is the limit we investigate in the next chapter, equation 2.29 implies that for instability we must have $4\mathcal{T}G \leq (r+1)^2/(1-r)$. In the limit $r \to 0$ the condition for instability becomes $\mathcal{T}G \leq 1/4$ to zeroth order in r.

2.3.2 Small density ratio

We are now ready to present results from the linear analysis for the logarithmic and the bounded wind profiles. The existing literature has primarily covered the case of small r, with the other parameters assumed to be of order one. In contrast, we are interested in covering a wider range of the control parameters, and thus provide a complete description of the full dispersion relation $C = C(K)$. We therefore briefly summarize Miles' results and move on to the general case.

Assuming the mass density ratio r is a small number (which is true for the air over water case) and the other parameters are of order one, Miles [27] expanded the

eigenfunction and the wave velocity C with respect to r

$$\phi = \phi_0 + r\phi_1 + r^2\phi_2 + \ldots, \qquad C = C_0 + rC_1 + r^2C_2 + \ldots \; ; \tag{2.30}$$

one then obtains the zeroth order solution as a linear gravity wave with constant amplitude and phase speed $C_0 = \sqrt{G/K}$. At first order $\mathcal{O}(r)$, one finds

$$\phi_{0,yy} - \left(K^2 + \frac{V_{,yy}}{V_0 - C_0}\right)\phi_0 = 0, \tag{2.31}$$

$$2KC_0C_1 - (V_0 - C_0)^2\phi_{0,y} + (V_0 - C_0) + G = 0. \tag{2.32}$$

The asymptotic expansion breaks down at the critical point $y = y_{cr}$ since to first order C_0 is real. Using the phase change of "$i\pi$ rule" across the critical layer from theory [37],[38], Miles obtains the growth rate of the perturbation at leading order in r:

$$\Im(C_1) = \frac{1}{2K}(V_0 - C_0)^2\Im\{\phi_{0,y}\} = -\pi\frac{(V_0 - C_0)^2}{2K}\left(\frac{V_{,yy}}{V_{,y}}\right)_{cr}|\phi_{cr}|^2, \tag{2.33}$$

where the last relation is obtained by multiplying equation 2.21 with the complex conjugate of ϕ and taking the principal value integral, with the contour going below the singularity; the subscript "cr" means evaluated at the critical point.

The dispersion relation $\Im\{C(K)\}$ is shown in figure 2.3a,b for the logarithmic and for the tanh wind profile for various values of G. The only difference between the two wind profiles appears at small wavenumbers: the tanh wind profile (whose asymptotic wind speed is bounded) does not permit waves traveling faster than the wind to become unstable. For this reason there is a cut-off which can be found in our small r approximation to be at $K = G$ for the tanh wind profile.

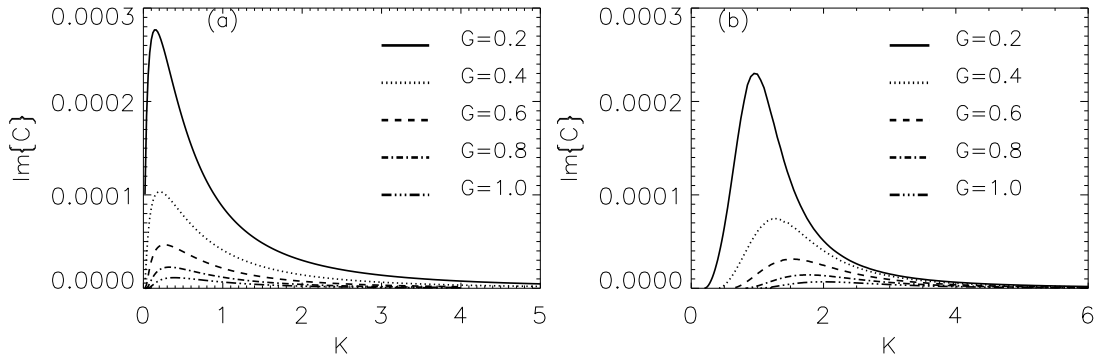

Figure 2.3: The imaginary part of C as a function of the wave number for density ratio $r = 10^{-3}$. Panel (a) is for a logarithmic wind profile and panel (b) is for a tanh wind profile.

2.3.3 Large density ratio

For large density ratio, we solve the system of equations 2.21–2.22 directly. We focus on the instability properties of special interest, such as the maximum growth rate, the wavelength of the fastest growing mode, and the dependence of the the stability boundaries on the parameters of the model. We solve equations 2.21- 2.22 numerically using a Newton-Ralphson method. We present results in figures 2.4 and 2.5. The plots suggest that for small enough r the dependence on r is linear (e.g. the $r = 0.001$ case is proportional to the $r = 0.01$ case by a factor of 10.0). For larger values of r the dependence is stronger than linear, and the smaller K modes seem to become more unstable.

2.3.4 General features of the CL instability

The main goal of our linear theory analysis is to establish the relevance of the critical-layer instability under various astrophysical or geophysical conditions. With this motivation in mind, we show here how the growth rate behaves as functions of the physical parameters G and r.

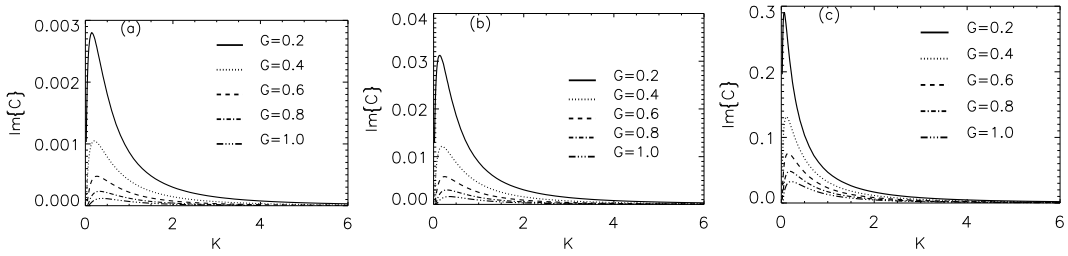

Figure 2.4: The Imaginary part of C as a function of the wavenumber for a logarithmic wind profile and (a) $r = 0.01$, (b) $r = 0.1$ and (c) $r = 0.5$.

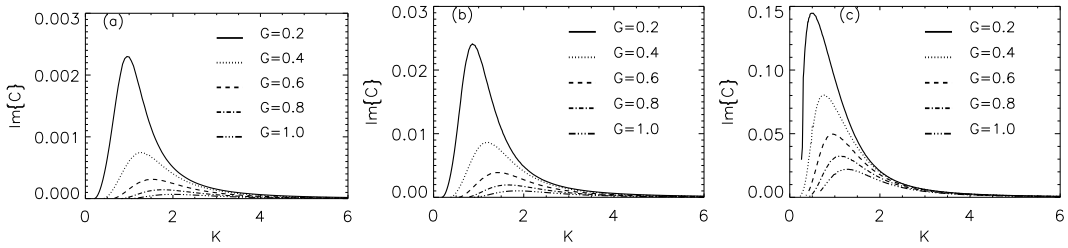

Figure 2.5: The Imaginary part of C as a function of the wavenumber for a tanh wind profile and (a) $r = 0.01$, (b) $r = 0.1$ and (c) $r = 0.5$.

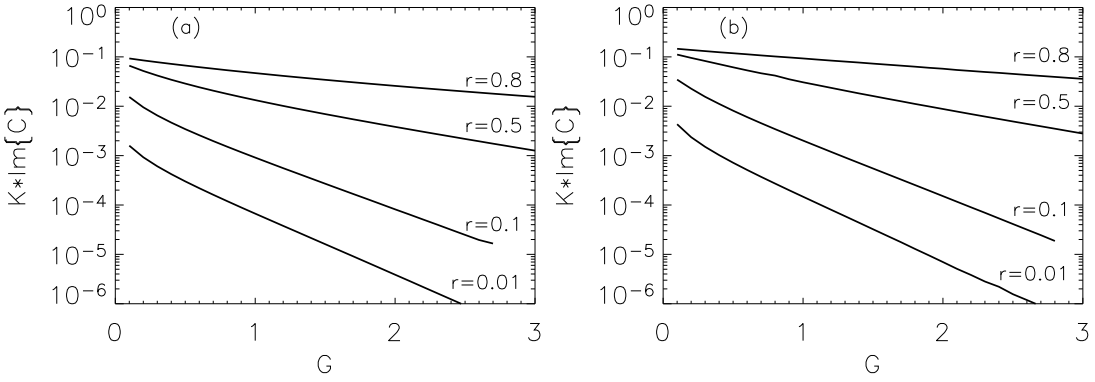

Figure 2.6: Growth rate of the fastest growing mode as a function of G (a) logarithmic wing profile, (b) tanh wind profile.

In figures 2.6a-b we have plotted the maximum growth rate $\gamma \equiv \Im\{CK\}_{\max}$ of the perturbation as a function of the control parameter G for the wind profiles (logarithmic and tanh) and for different values of r. It is clear in all cases that there is an exponential dependence on G for $G \geq 1$. This might be expected because increasing gravity leads to an increase of the real part of C; therefore the imaginary part of ϕ, that falls exponentially with the distance from the critical layer, will have an exponentially smaller component at the interface. In appendix A.3, we carry out an asymptotic analysis for large G for the wind profile $U = U_{\max}(1 - e^{-y/\delta})$, and derive this exponential dependence. More specifically, the growth rate of the most unstable mode is found to be

$$\max(K \ \mathrm{Im}\{C\}) \sim e^{-2q_m \mathcal{A}_t G}, \tag{2.34}$$

where weaker algebraic dependencies have been ignored here; $q_m \simeq 2.45\ldots$ is the root of a transcendental equation. The zeroth order of the real part of the phase speed C is $\mathrm{Re}\{C\} = \sqrt{\mathcal{A}_t G/K}$. The exact formula is given in the Appendix (A.3). As is shown there, the stream function Ψ below the critical layer is composed of an exponentially increasing and an exponentially decreasing component. Since the boundary condition must be satisfied, the exponentially large component must be in phase with h, which leaves us with the exponentially small, out of phase, component to drive the wave unstable. Further calculation then leads to the result given above. In figure 2.7 we show a comparison of the asymptotic results with the ones predicted numerically. A similar behavior is expected for other wind profiles but we do not pursue the asymptotic analysis further here.

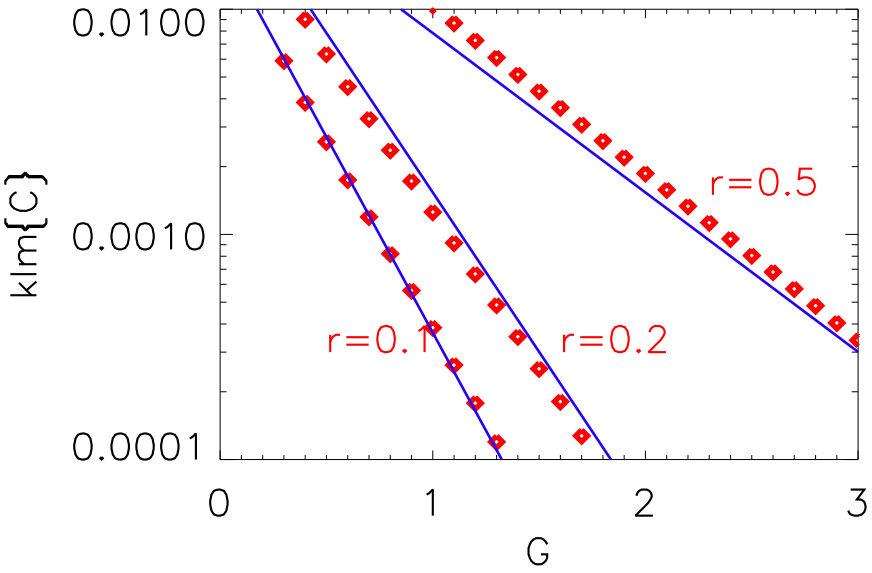

Figure 2.7: A comparison of the asymptotic exponential dependence of the maximum growth rate (blue lines) with G with numerical results (red diamonds); for the wind profile $U(y) = U_1(1 - \exp(y/\delta))$.

2.4 Surface Tension

For the sake of completeness, we have also examined the case in which surface tension at the density interface is included[4]. We again assume a wind shear profile of the form $\log(y+1)$ and $\tanh(y)$. The only change in our set of equations to solve is then an additional term in the boundary condition, equation 2.22. Hence

$$KC^2 - r\Big[(V_0 - C)^2\phi_y - (V_0 - C)V_y\Big] - G(1-r) - TK^2 = 0, \tag{2.35}$$

where $T \equiv \sigma/(\delta\rho_2 \mathrm{U}_1^2))$ and σ is the surface tension ($\sigma = B^2/(2\pi\mu K)$) for the case of the magnetic field [29]). We show the resulting solutions, namely the dispersion relations, in figures 2.8a-b. As expected tension decreases the growth rate and becomes important only in large wavenumbers.

4. We note that a magnetic field in the lower fluid aligned with the flow, would lead to an equivalent treatment.

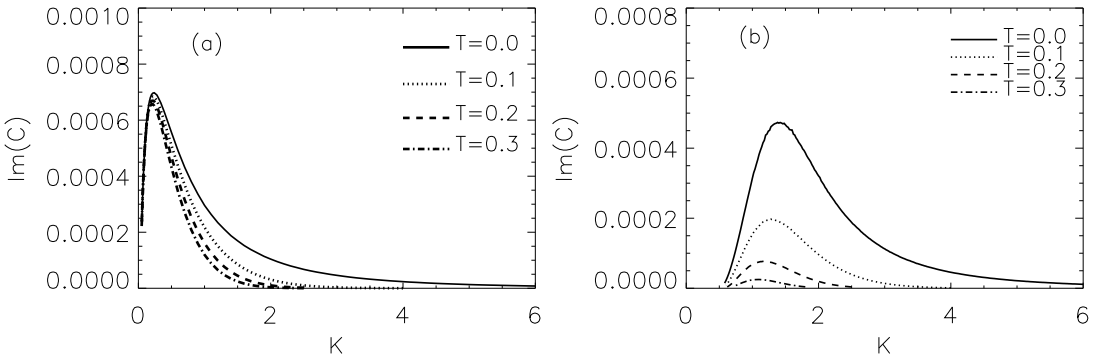

Figure 2.8: The imaginary part of C for $G = 0.5$, $r = 0.01$ and different values of the surface tension. (a) logarithmic wing profile, (b) tanh wind profile.

An important result, is that in the small density ratio limit, the real part of C (to zeroth order in r) is $C_0 = \sqrt{G/K + TK}$ which has its minimum value $C_{\min} = \sqrt{2}(GT)^{1/4}$ at $K = \sqrt{G/T}$. Thus, for the case of a bounded wind profile (such as the tanh profile) there is a minimum value of $U_{\max}$, given by $C_{\min}$, so that a critical layer can exist. We remind the reader that a similar minimum velocity bound also exists for the Kelvin-Helmholtz instability, and is given by

$$U \geq \sqrt{\frac{2}{r}\sqrt{\frac{g\sigma}{\rho_2}}} \approx 650 \ \text{ cm/sec} \ ,$$

where we have retained only terms of first order in r. For the CL case we have instead

$$U \geq \sqrt{2\sqrt{\frac{g\sigma}{\rho_2}}} \approx 20 \ \text{ cm/sec} \ ,$$

which differs from the previous bound by a factor of $\sqrt{r}$. (The numerical values shown here are derived for the case of air blowing over water.) This illustrates the fact that for low wind conditions, the CL instability dominates the KH instability for driving water surface waves.

2.5 Compressible case

Finally we consider the compressible case. We will consider a compressible fluid in the upper layer with sound speed $c_s(y)$ and an incompressible fluid below. The dimensionless equations we have to solve now are:

$$\phi_{,yy} - \left[\kappa^2 + G\frac{\tilde{\rho}}{\rho|_{y=0^+}}\frac{K_s + K_g}{\tilde{V}_G^2} + \frac{\tilde{V}_{G,yy}}{\tilde{V}_G}\right]\phi = 0 \tag{2.36}$$

$$KC^2 - r\left[\tilde{V}_G^2\phi_{,y} - \partial_y\tilde{V}_{G,y}\right] - G(1-r) = 0 \tag{2.37}$$

where

$$\kappa^2 = K^2\left(1 - \frac{V_G^2}{C_s^2}\right), \quad K_s = \frac{\rho_{,y\delta}}{\rho}, \quad K_g = G/C_s^2, \quad C_s = c_s/U_1$$

and

$$\tilde{V}_G = \frac{KV_G\sqrt{\tilde{\rho}/\rho|_{y=0^+}}}{\kappa} \quad \text{with} \quad r = \rho|_{y=0^+}/\rho|_{y=0^-}.$$

We will assume for simplicity an adiabatic atmosphere,

$$\rho = \rho|_{y=0^+}\left(1 - (\gamma-1)\frac{\rho_o}{\gamma P_o}gy\right)^{\frac{1}{1-\gamma}} \tag{2.38}$$

$$P = P|_{y=0}\left(\frac{\rho}{\rho_o}\right)^{\gamma}. \tag{2.39}$$

This assumption, which is commonly used in the atmospheric sciences to simplify the physics involved, has the advantage that $K_g + K_s = 0$, so our equation becomes by one order less singular, and therefore easier to solve.

We will not deal here with supersonic flows since in most astrophysical realms in which interfacial wave generation plays an important role (viz., on white dwarf

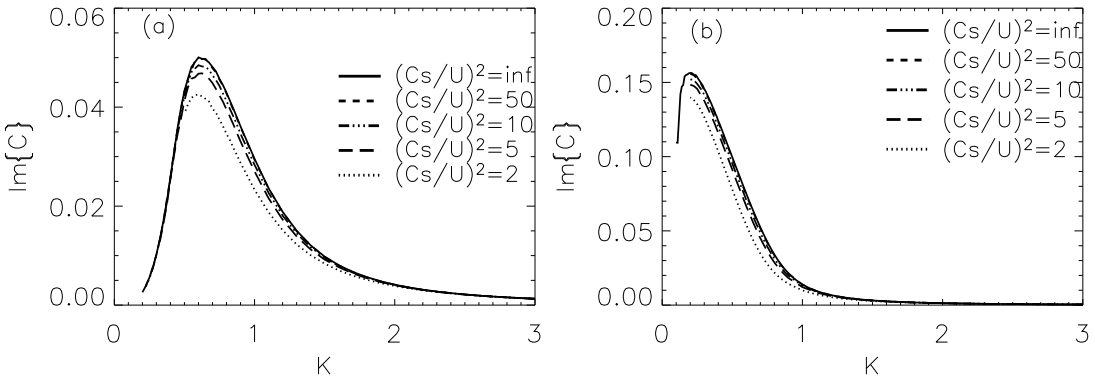

Figure 2.9: The imaginary part of C for the tanh wind profile, $r = 0.1$ and (a) $G = 0.1$, (b) $G = 0.01$ and different values of sound speed.

surfaces) the relevant flows are thought to be subsonic; for this reason we will consider only the tanh wind profile. We shall also deal with small values of G, so that the pressure scale height is large and the breakdown of the adiabatic assumption at values of $y \sim K_s^{-1}$ will not affect us either.

The dispersion relation for different values of C_s and for a tanh wind profile is given in figures 2.9a,b. Compressibility, as it can be seen from the figures, decreases the growth rate. This is an expected result, since our system has now more degrees of freedom (e.g., now the perturbation stores thermal energy as well). We conclude, however, that the deviation from the incompressible case is not very large, even for relatively strong (but still subsonic) winds.

2.6 Summary of linear theory

In this chapter we have explored the linear instability properties of wind shear layers in the presence of gravitational stratification. Our principal aim was to explore the full parameter space of the solutions, defined by the three parameters K (the perturbation wavenumber), G, and r (the density ratio). For generality purposes we examined

three different wind profiles. The only notable difference, is between the unbounded (logarithmic) wind profile and the bounded wind profiles (1-exp(y/δ) and tanh(y/δ)) at small wave numbers. However the difference originates from the nonphysical increase of the wind velocity at high altitudes where the boundary layer theory (that the logarithmic wind profile is derived from) does not longer apply.

We have constructed stability boundaries for the instability, and determined the dependence of these boundaries on the given parameters. As we discuss later, the non-linear development of the instability (and therefore mixing) will crucially depend on the kind of modes that become unstable; therefore an investigation of the stability boundaries is necessary before the study of the nonlinear regime. An important result also derived from our analysis, allowing us to make predictions on the importance of the instability and on the nonlinear development, is the scaling of the growth rate with the parameters G and r in §2.3.4. Clearly for $A_t G \gg 1$ strong mixing is not expected. Finally we investigated the effects of surface tension and compressibility. With the inclusion of surface tension, we obtained a bound on the velocity for the instability to exist. We also found that for subsonic winds the instability weakly depends on the Mach number.

As we have shown, there are significant differences between the CL and the KH modes, both in the parameter ranges in which the instability can occur (e.g., the stability boundaries) and in the magnitude of the growth rate; these differences can be expected to result in different nonlinear evolution of the underlying physical system. For example, it is well-known that CL instability in the air over water case is responsible for generating waves for winds of magnitude below the threshold for which Kelvin-Helmholtz instability exists [27].

Table 2.1: Approximate range for parameter G in three different situations.

	U_1(cm s^{-1})	g cm s^{-2}	δcm^{-1}	G
ocean	$10^2 \sim 10^3$	10^3	$10 \sim 10^2$	$10^{-1} \sim 1$
Sun's surface	$10^2 \sim 10^5$	$10^{4.3}$	$10^6 \sim 10^7$	$10^{1.3} \sim 10^{6.3}$
WD	$10^4 \sim 10^7$	10^8	$10^3 \sim 10^6$	$1 \sim 10$

CHAPTER 3

WEAKLY NON-LINEAR THEORY

3.1 Introduction

In this chapter, we uncover the non-linear evolution of wind-driven surface waves by examining their finite-amplitude evolution using an asymptotic expansion. There are a number of alternatives for studying the nonlinear behavior of wind-driven surface waves, such as for example turbulent modeling of the wind-wave coupling [39, 40, 41]; our focus is instead on weakly non-linear theory because we seek a first-principles understanding of the effects of nonlinearities as the wave amplitude emerges from the linear regime. We further note here that the weakly non-linear theory for the KH instability has already been derived by [42]; and that a Ginzburg-Landau equation was also derived for viscous flow by [43] and [44] for cases where viscous dissipation dominates in saturating the gravity wave amplitude. However, classical finite amplitude analysis in the weakly nonlinear limit cannot be applied straightforwardly to our problem because of the presence of critical layers: Due to the singularity that appear in the linear theory at the point where the phase speed of a surface wave matches the wind speed, higher order terms in the expansion become more singular and the expansion must ultimately fail. The fundamental reason for this behavior is that the flow becomes non-linear first inside the critical layer, even though the rest of the flow can still be considered as operating in the linear regime. For this reason, a more refined treatment of the critical layer is required. The necessary analytical 'machinery' fortunately already exists: Thus, [45], and later [46], showed that for small but finite amplitudes the phase change at the critical layer does not necessarily have to be $-i\pi$; instead, they found that the phase change is zero if the non-linear terms are

taken into account. Later [47] showed numerically that there is a smooth increase of the phase change, from $-i\pi$ to 0, and introduced the function Φ_H that gives the phase change as a function of the amplitude; [48, 49, 50] then derived an ordinary differential equation to describe the evolution of the amplitude of the perturbation based on Φ_H and other similar functions defined for the appropriate critical layer problem. A fundamental assumption in all this work is that the viscosity is dominant in the critical layer; this leads to the derivation of an ordinary differential equation for the wave amplitude. The full equations of the weakly nonlinear problem without the previous assumption have then been derived and solved numerically for various cases [51, 52, 53].

In our case the treatment – although closely related to the earlier work – is nevertheless different in some respects. The previously discussed cases were dealing with a smooth neutral mode where the critical layer was formed at the inflection point $d^2U/dy^2 = 0$. The problem at hand though, deals with neutral modes (gravity waves) that are weakly coupled to a non-modal disturbance in the critical layer in the upper layer. Unlike the previous cases the marginally unstable modes do not form a critical layer at the inflection point since such an inflection point does not exist. Instead gravity waves become weakly unstable if the coupling between the upper fluid (wind) and the gravity modes of the lower fluid is weak. This can be the result of a small coupling coefficient (small density ratio) or if the wind velocity is close to but higher than the smallest phase velocity of the gravity waves. This allows us to examine two special cases: the case of small density ratio, and the case of weak wind or strong stratification; in both cases, the linear growth rate is small. The first case has been examined by [54] and applied to ocean waves. We will focus on the second case which is of particular interest to our astrophysical problem, since the instability takes place on the surface of a white dwarf star, i.e., a star of solar mass, but compa-

rable in size to the Earth; this corresponds to the strongly stratified limit. Another technical difference from the previous cases appears in the derivation of the amplitude equations and lies in the fact that we have a sharp interface. Because of this, our solvability condition will not be expressed in terms of integrals but rather in terms of appropriate vector products of the values of the perturbation stream function at the interface.

An interesting aspect we further examine, with direct applications to the relevant astrophysical and geophysical systems, is the mixing properties of the finite amplitude equations. Although the weakly non-linear results do not lead to wave breaking, which is the main mechanism for mixing the 'surface material' with the 'atmosphere', we study the mixing of tracers inside the critical layer as a first step for revealing the mixing properties of the fully non-linear problem. We measure the finite time Lyapunov exponents and the particle dispersion of the flow.

3.2 Formulation

As before, we consider a two-layer system with constant fluid density ρ_1 and ρ_2 ($\rho_1 \leq \rho_2$) in the upper and lower layers, respectively. The interface between the two layers is given by $y = h(x,t)$, where x is the horizontal and y is the vertical coordinate. In the upper layer we assume a wind parallel to the originally flat interface $y = h(x, t = 0) = 0$. The wind has a shear velocity profile $\vec{U} \equiv [U(y), 0]$, where $U(y)$ varies only with y. The exact form of the wind profile we chose is:

$$U(y) = U_{\max}(1 - \exp(-y/\delta)) \,.$$

The lower layer is initially at rest; thus, we will not consider the more complex, albeit more realistic, case of additional shear in the lower layer [55]. Our aim is to study the dynamics and the weakly nonlinear development of a small sinusoidal perturbations of the horizontal interface.[1]

The fluid is assumed incompressible in both layers; we therefore work with the stream function Ψ, which is connected to the velocity by the relation $(u, v) = (\partial_y \Psi, -\partial_x \Psi)$. The stream function can be separated into its mean and its perturbation components,

$$\Psi_{\text{total}} = \int_0^y U dy' + \Psi \,. \tag{3.1}$$

The fluid within each layer is described by the Navier-Stokes equations (in terms of the stream function Ψ):

$$\nabla^2 \Psi_{,t} + U \nabla^2 \Psi_{,x} - U_{,yy} \Psi_{,x} = \Psi_{,x} \nabla^2 \Psi_{,y} - \Psi_{,y} \nabla^2 \Psi_{,x} + \nu \nabla^2 \nabla^2 \Psi, \tag{3.2}$$

where ∇^2 is the two-dimensional Laplacian and ν is the viscosity (which we will consider to be small, and therefore negligible except for a narrow region within the critical layer).

The boundary conditions at the interface are the continuity of the perpendicular

1. As an aside, we note that the presence of a sharp interface boundary between the two fluids in our system is really only a device to simplify the analysis, but in no way restricts our results. That is, in a more general case there will be no sharp interface, but the density will change smoothly from ρ_2 to ρ_1 in a layer of width δ_1. We would then also expect $U(y)$ to be a smooth function in y, so that any flow discontinuity at the interface would be replaced by a smooth variation in U within a thin viscous boundary layer of width δ_2. One would then expect to see differences in behavior only for those modes with horizontal wavenumber k large enough so that the critical layer lies inside these layers δ_1, δ_2. Such modes, however, are KH-modes which are not under study here; they will obey a Richardson-type stability criterion, $1/4 < g(\Delta\rho/\rho)\delta_2^2/\delta_1$ [29]. We therefore expect our assumption of a sharp interface to be reasonable for horizontal wave-numbers $k^{-1} \geq \max\{\delta_1, \delta_2\}$. Since we are primarily interested in long wavelength perturbations, we conclude that, for our purposes, we have not disregarded any important physics.

component of the velocity to the interface

$$h_{,t} + (U^{\pm} + \Psi^{\pm}_{,y})h_{,x} + \Psi^{\pm}_{,x} = 0\,, \tag{3.3}$$

and the continuity of pressure

$$\Delta\Big[\rho_i\{\Psi_{,ty} + (U+\Psi_{,y})\Psi_{,xy} - \Psi_{,x}(U_{,y}+\Psi_{,yy}) - h_{,x}(\Psi_{,tx} + (U+\Psi_{,y})\Psi_{,xx} + \Psi_{,x}\Psi_{,xy})\}\Big]$$

$$= gh_{,x}(\rho_2 - \rho_1)\,, \tag{3.4}$$

where $h(x,t)$ is the elevation of the interface and all quantities above are evaluated at $y = h(x,t)$. The $\pm$ indices indicate values above and below the interface, and $\Delta[\quad]$ denotes the difference across $y = h$ (e.g., $\Delta[f(y)] = f(h^+) - f(h^-)$).

We non-dimensionalize lengths by the characteristic length l of the wind (a typical length over which the wind strength changes), and the velocities by the asymptotic value of the wind at $y \to +\infty$, U_{max}. An important parameter that emerges from the scaling is $G \equiv gl/U^2_{max}$, which is a measure of the ratio of potential energy to kinetic energy, or alternatively, a measure of the strength of the stratification. Other dimensionless parameters are the Reynolds number, $Re \equiv U_{max}l/\nu \gg 1$, and the ratio of densities, $r \equiv \rho_1/\rho_2 \leq 1$. In terms of the non-dimensional parameters, we focus on the case where $Re \gg 1$ in each layer, and especially the limit $G \gg 1$ (accretion on white dwarfs in astrophysics).

3.3 Derivation of Amplitude Equations

We are now ready to embark upon the weakly non-linear theory. Formally this is done by assuming that, for some parameter ranges of interests, our physical system

lies close to a marginally stable state so that an asymptotic expansion is allowed near the center manifold. For the problem at hand, however, and in the absence of surface tension ($\mathcal{T} = 0$), marginally stable states are possible only when $r = 0$ or $1/G = 0$; the first one expresses the nonphysical situation that there is no upper fluid, and the latter corresponds to a situation where there is no wind in the upper fluid ($U_{max} \sim 1/\sqrt{G}$). Complication arises as we deviate from these neutrally stable states. In ordinary dissipative systems, only a small number of modes near the center manifold become unstable and need to be considered. In our case though, once the density ratio r or the parameter G is finite, an infinite number of modes become unstable if surface tension $\mathcal{T} = 0$. Ideally the interaction of all these modes needs to be taken into account. Practically this difficulty is removed by the combined effect of surface tension $\mathcal{T}$ (or, equivalently, the presence of a magnetic field) and weak viscous damping. In the presence of surface tension the stability boundary in the $(r, G, \mathcal{T})$ space is given by the condition for positive solutions of eq.(2.29) and by $r = 0$. Surface tension reduces the number of unstable modes by neutralizing modes of wave numbers above some cut-off value. Furthermore, weak viscosity will damp out the neutrally stable modes of high wave numbers, rendering them asymptotically stable. By using a periodic domain, we can fix the period so that only one mode becomes unstable; by doing this we omit wave-packet effects [56, 57] that would complicate the analysis, and we will therefore ignore them in this first look of the problem. We can then derive the amplitude equation for this single mode as usual.

We focus on situations where $G \gg 1$, corresponding to weak winds or strong gravitation for arbitrary density ratio. As will be shown, the amplitude equations are very similar to those obtained by Reutov for small density ratio ($r \ll 1$) case.

In chapter 2 we showed that unstable modes for the large G case grow at a rate proportional to $\exp\{-2q_m\mathcal{A}_t G t\}$. Inspired by this result, in the limit $G \gg 1$, we set

the time derivative $\partial_t = \epsilon\partial_T - C\partial_x$, where ϵ (defined later) is small such that the linear growth rate (imaginary part of C) is of order $\mathcal{O}(\epsilon)$. We expand the stream function above the interface as

$$\Psi^+ = \epsilon^2\Psi_0^+ + \epsilon^3\Psi_1^+ + \ldots \tag{3.5}$$

The governing equation (3.2) for the upper fluid is then

$$\epsilon\nabla^2\Psi^+_{,T} + U\nabla^2\Psi^+_{,x} - U_{,yy}\Psi^+_{,x} = \Psi^+_{,x}\nabla^2\Psi^+_{,y} - \Psi^+_{,y}\nabla^2\Psi^+_{,x} + \nu\nabla^2\nabla^2\Psi^+ \tag{3.6}$$

and for the lower fluid

$$\epsilon\nabla^2\Psi^-_{,T} = \Psi^-_{,x}\nabla^2\Psi^-_{,y} - \Psi^-_{,y}\nabla^2\Psi^-_{,x} + \nu\nabla^2\nabla^2\Psi^- \tag{3.7}$$

The boundary conditions at the interface are given by

$$\epsilon h_{,T} - Ch_{,x} + \Psi^+_{,x} = \text{N.L.T.}, \qquad \epsilon h_{,T} - Ch_{,x} + \Psi^-_{,x} = \text{N.LT.} \qquad \text{and} \tag{3.8}$$

$$r\left[\epsilon\Psi^+_{,Ty} - C\Psi^+_{,xy} - U^+_{,y}\Psi^+_{,x}\right] - \left[\epsilon\Psi^-_{,Ty} - C\Psi^-_{,xy}\right] - \left[G(1-r)h - \mathcal{T}h_{,xx}\right] = \text{N.L.T.}\,. \tag{3.9}$$

where N.L.T. are the non-linear terms that are of higher order in ϵ. At the zeroth order we have

$$(U-C)\nabla^2\Psi^+_{0,x} - U_{,yy}\Psi^+_{0,x} = 0\,;$$

expanding in normal modes, $\Psi_0 = \phi_0(y)e^{iKx} + \text{c.c.}$, we have

$$\phi_{0,yy} - \left[K^2 - \frac{U_{,yy}}{U-C}\right]\phi_0 = 0\,, \tag{3.10}$$

where we have focused on the most unstable mode. Equation (3.10) is the Rayleigh equation with a singular behavior at the point y_c where $U(y_c) = C$. The solutions of (3.10) around the critical layer can be expanded in series (2.26,2.27) $\phi_0 \simeq A[1 - (U_c''/U_c')(y-y_c)\ln(|y-y_c|)+\ldots]+B[(U_c''/U_c')(y-y_c)+\ldots]$. Of course, the singularity is removed from the real axis if the phase velocity is complex. Nonetheless if the imaginary part of C is of order ϵ (as in the case we now examine), the vorticity perturbation becomes of order $\epsilon^{-1}\epsilon^2 = \epsilon$ near the critical layer, reducing the non-linear terms to the same order in ϵ as the linear terms, and they have to be taken into account in the asymptotic expansion in the critical layer.

Outside the critical layer the non-linearity is at higher order ($\mathcal{O}(\epsilon^4)$) and can therefore be neglected. It is thus sufficient to use the results from the linear theory for the outer scales. The outer solution (away from the critical layer) can be evaluated numerically. In the case of large G case we also have $K \geq \mathcal{A}_t G \gg 1$ according to (2.28); thus we can express ϕ_0 using W.K.B.J. approximation as an asymptotic expansion in terms of $1/K$. An analytic expression for the growth rate can also be obtained in this expansion. We write ϕ_0 as

$$\phi_0 = \begin{cases} A_3\phi_{above} & \text{if } y > y_c \\ A_1\phi^+_{below} + B_1\phi^-_{below} & \text{if } 0 < y < y_c \end{cases} \tag{3.11}$$

where ϕ_{above} is the exponentially decreasing solution for $y \to +\infty$ and $\phi^{\pm}_{below}$ are the two linearly independent (exponentially increasing and exponentially decreasing) solutions of (3.10). The amplitude coefficients A_1 and B_1 are determined from the inner scaling. In terms of the W.K.B.J. expansion carried out in appendix A, these

solutions can be written at first order in $1/K$ (note $K \gg 1$), as

$$\phi_0 = \begin{cases} \frac{\sqrt{\pi}}{2} A_3 \frac{1}{\sqrt{w}} e^{-\int_{y_a}^{y} w dy'}, & \text{for } y > y_a \\ -\sqrt{\pi} A_3 \cos[I_1] \frac{1}{\sqrt{w}} \sin\left(\int_{y_c}^{y} w dy' - \pi/4\right) & \\ \quad + \sqrt{\pi} A_3 \sin[I_1] \frac{1}{\sqrt{w}} \cos\left(\int_{y_c}^{y} w dy' - \pi/4\right), & \text{for } y_a > y > y_c \\ \sqrt{\pi} A_1 \sin[I_1] e^{-I_2} \frac{1}{\sqrt{w}} e^{+\int_0^y w dy'} & \\ \quad + \frac{\sqrt{\pi}}{2} B_1 \cos[I_1] e^{+I_2} \frac{1}{\sqrt{w}} e^{-\int_0^y w dy'}, & \text{for } y_c > y \end{cases} \tag{3.12}$$

where I_1 and I_2 are integrals determined from the linear solution and are defined in the appendix (A). w is defined in equation (A.21) and y_a is the solution of $w(y) = 0$.

At second order $\Psi_1 = \phi_1 e^{iKx}$ satisfies the inhomogeneous equation

$$\phi_{1,yy} - \left[K^2 - \frac{U_{,yy}}{U - C}\right] \phi_1 = \frac{U_{,yy}}{iK(U-C)^2} \phi_{0,T} \tag{3.13}$$

which again can be solved numerically. Noting that inhomogeneous term is of order $1/K^3$ (in the rescaled units $y \to Ky$) everywhere except inside the critical layer, it can be expressed in a W.K.B.J. expansion. For further analysis, it is sufficient to know that below and away from the critical layer, ϕ_1 can be expressed as

$$\phi_1 = A_1^{(1)} e^{+I_2} \frac{1}{\sqrt{w}} e^{-\int_0^y w dy'} + B_1^{(1)} e^{-I_2} \frac{1}{\sqrt{w}} e^{+\int_0^y w dy'}$$

In order to match the outer solution with the solution inside the critical layer we need to know the asymptotic expansion of the outer solution as $y \to y_c$. Following similar calculations as in the linear theory, **above** the critical layer we have

$$\phi_0 \simeq A_3 \Big[\pi \cos[I_1][-z + \ldots] + \sin[I_1][1 - z\ln(z) + \ldots + (1 - 2\gamma)z + \ldots]\Big] \tag{3.14}$$

and

$$\phi_1 \simeq \frac{U_c'' \sin[I_1]\, A_{3,T}}{i2KU_c'^2} \ln|z| + \ldots \tag{3.15}$$

where $z = (y - y_c)(-U_c'')/U_c'$, γ is the Euler Masceroni constant and the subscript c means evaluated at the critical point. **Below** the critical layer the asymptotic expansion gives

$$\phi_0 \simeq A_1 \sin[I_1][1 - z\ln|z| + \ldots + (1-2\gamma)z + \ldots] + \pi B_1 \cos[I_1] e^{-I_2}(-z + \ldots) \tag{3.16}$$

and

$$\phi_1 \simeq \frac{U_c'' \sin[I_1]\, A_{1,T}}{i2KU_c'^2} \ln|z| + \ldots \tag{3.17}$$

Next we examine the dynamics of the inner scaling in the critical layer.

3.3.1 Inner Solution

To capture the dynamics of the critical layer, we use the scaling $\Psi \to \epsilon^2\tilde{\Psi}$, $y - y_c \to \epsilon Y$ and $1/R \to \epsilon^3\nu$. From equation (3.6) we obtain

$$\tilde{\Psi}_{,TYY} + U_c' Y \tilde{\Psi}_{,xYY} + \tilde{\Psi}_{,Y}\tilde{\Psi}_{,YYx} - \tilde{\Psi}_{,x}\tilde{\Psi}_{,YYY} - \nu\tilde{\Psi}_{,YYYY}$$

$$= -\epsilon\left[\frac{1}{2}U_c'' Y^2 \tilde{\Psi}_{,YYx} - U_c''\tilde{\Psi}_{,x}\right] + \mathcal{O}(\epsilon^2)\,. \tag{3.18}$$

In order to match with the outer solution (3.14,3.16) we expand $\tilde{\Psi}$ as

$$\tilde{\Psi} = \tilde{\Psi}_0 + \epsilon\ln(\epsilon)\tilde{\Psi}_1 + \epsilon\tilde{\Psi}_2 + \epsilon^2\ln(\epsilon)\tilde{\Psi}_3 + \epsilon^2\tilde{\Psi}_4 + \ldots\,. \tag{3.19}$$

To first order, we then have

$$\tilde{\Psi}_{0,TYY} + U_c' Y \tilde{\Psi}_{0,xYY} + \tilde{\Psi}_{0,Y}\tilde{\Psi}_{0,YYx} - \tilde{\Psi}_{0,x}\tilde{\Psi}_{0,YYY} - \nu\tilde{\Psi}_{0,YYYY} = 0\,.$$

Matching with the outer solution we obtain

$$\tilde{\Psi}_0 = \sin[I_1](A_1 e^{iKx} + A_1^* e^{-iKx})\,, \tag{3.20}$$

and therefore $A_1 = A_3 \equiv A$. To the next order ($\epsilon \ln(\epsilon)$), we have

$$\tilde{\Psi}_{1,TYY} + U_c' Y \tilde{\Psi}_{1,xYY} - \tilde{\Psi}_{0,x}\tilde{\Psi}_{1,YYY} - \nu\tilde{\Psi}_{1,YYYY} = 0\,.$$

Matching with the outer solution we obtain

$$\tilde{\Psi}_1 = \left[A\frac{U_c''}{U_c'}Y + \partial_T A \frac{U_c''}{i2KU_c'^2}\right]\sin[I_1]e^{iKx} + \text{c.c.} \tag{3.21}$$

To third order (ϵ^3), we have

$$\tilde{\Psi}_{2,YYT} + U_c' Y \tilde{\Psi}_{2,YYx} - \tilde{\Psi}_{0,x}\tilde{\Psi}_{2,YYY} - \nu\tilde{\Psi}_{2,YYYY} = U_c''\tilde{\Psi}_{0,x}\,. \tag{3.22}$$

Denoting $Z = \tilde{\Psi}_{2,YY}$, which is the vorticity inside the critical layer, we obtain

$$Z_{,T} + U_c' Y Z_{,x} - \tilde{\Psi}_{0,x} Z_{,Y} - \nu Z_{,YY} = U_c''\tilde{\Psi}_{0,x}\,. \tag{3.23}$$

To match with the outer solution, we require the boundary conditions of Z

$$\lim_{Y\to+\infty} Z = \left[A\frac{U_c''}{U_c'}\frac{1}{Y} - \frac{U_c''}{2iKU_c'^2}\frac{1}{Y^2}A_{,T}\right]\sin[I_1]e^{iKx} + \text{c.c.}$$

and similarly for $Y \to -\infty$ with A replaced by B_1. Integrating Z along Y and using the asymptotic behavior of Ψ_2 above and below the critical layer, we obtain

$$\int_{-\infty}^{+\infty} Z dY = \Big[\Psi_{2,Y}\Big]_{-\infty}^{+\infty} = \pi \frac{U_c''}{U_c'} \cos[I_1]\Big[A - B_1\Big] e^{iKx} + \text{c.c.}\,,$$

where we have taken the limiting procedure $\lim_{\epsilon\to 0} \int_{-1/\epsilon}^{1/\epsilon} Z\ dY$. Defining

$$J \equiv \frac{K}{2\pi \sin[I_1]} \frac{U_c'}{U_c''} \int_{-\pi/K}^{+\pi/K} e^{-iKx} \int_{-\infty}^{+\infty} Z dY dx\,. \tag{3.24}$$

we obtain the following important result:

$$\cos[I_1]B_1 = \cos[I_1]A - \frac{1}{\pi}\sin[I_1]J\,. \tag{3.25}$$

The last equation (3.25) implies that the phase change across the critical layer depends on the detailed treatment of the vorticity dynamics inside the critical layer. In the linear case $J = +i\pi A$, but as the amplitude grows and the non-linear term $\tilde{\Psi}_{0,x}Z_{,Y}$ in equation (3.23) becomes important, the phase change will decrease.

3.3.2 Boundary conditions and the amplitude equation

Combining the above results we find that the streamfunction at the interface is

$$\Psi_0|_0 = \frac{\sqrt{\pi}}{2}\left[A\Big(2\sin(I_1)e^{-I_2} + \cos(I_1)e^{+I_2}\Big) - \frac{1}{\pi}J\sin(I_1)e^{+I_2}\right] e^{iK(x-Ct)} + \text{c.c.} \tag{3.26}$$

$$\Psi_{0,y}|_0 = \frac{\sqrt{\pi}}{2}K\left[A\Big(2\sin(I_1)e^{-I_2} - \cos(I_1)e^{+I_2}\Big) + \frac{1}{\pi}J\sin(I_1)e^{+I_2}\right] e^{iK(x-Ct)} + \text{c.c.}\,, \tag{3.27}$$

Unlike the linear case, the phase change is now defined by J in equation (3.24). The slow time scale mentioned before is defined by by the value of C_i, which is exponentially small and is given by equation (2.34). We therefore define $\epsilon \equiv e^{-2I_2} \sim e^{-2G}$, and equations (3.26) and (3.27) can be re-written as

$$\Psi_0|_0 = \frac{\sqrt{\pi}}{2}\left[\frac{1}{\sqrt{\epsilon}}A\cos(I_1) - \frac{1}{\sqrt{\epsilon}\pi}J\sin(I_1) + 2\sqrt{\epsilon}A\sin(I_1)\right]e^{iKx} + \text{c.c.}\,. \qquad (3.28)$$

To match with the upper fluid we expand Ψ^- and h as:

$$\Psi^- = \epsilon^{3/2}\Psi_0^- + \epsilon^{5/2}\Psi_1^- + \ldots \quad \text{and} \quad h = \epsilon^{3/2}h_0 + \epsilon^{5/2}h_1 + \ldots$$

We write the zeroth order stream function Ψ_0^- below the interface, and the surface elevation h_0 as $\Psi_0^- = CHe^{iKx+Ky} + \text{c.c.}$ and $h_0 = He^{iKx} + \text{c.c.}$, H being the amplitude of the wave.

The first order ($\epsilon^{3/2}$) boundary conditions give us $M \cdot V_0 = 0$, where

$$M = \begin{bmatrix} -C & 1 & 0 \\ -C & 0 & 1 \\ -\tilde{G}(1-r) & rCK & CK \end{bmatrix} \quad \text{and} \quad V_0 = \begin{bmatrix} H \\ \Phi \\ CH \end{bmatrix}. \qquad (3.29)$$

$\Phi = (A\cos(I_1) - \frac{1}{\pi}J\sin(I_1))$ is the amplitude of the stream function at the interface and $\tilde{G} = G + K^2\mathcal{T}/(1-r)$ is the gravity term including the effect of surface tension. Here we have discarded the $U_{,y}$ term since it is of order $1/K$. For a non-trivial solution, we must have $\det(M) = 0$. This leads us to the relation $C = \sqrt{\tilde{G}\mathcal{A}_t/K}$ and $HC = \Phi$.

At the next order, we have ϕ_1 at the interface

$$\phi_1|_0 = A_1^{(1)}\frac{1}{\sqrt{\epsilon}} + B_1^{(1)}\sqrt{\epsilon} \text{ and } \phi_{1,y}|_0 = -KA_1^{(1)}\frac{1}{\sqrt{\epsilon}} + KB_1^{(1)}\sqrt{\epsilon} \tag{3.30}$$

where the values of $A_1^{(1)}, B_1^{(1)}$ depend on $A_{,T}$, and can be obtained by matching with the inner solution at the critical layer. The second term in equation (3.30) is exponentially small (of order $\sqrt{\epsilon}$) and can thus be neglected. The stream function of the lower fluid Ψ_1^- and the elevation h_1 at this order are $\Psi_1^- = CH^{(1)}e^{iKx+Ky} + \text{c.c.}$ and $h_1 = H^{(1)}e^{iKx} + \text{c.c.}$. The boundary conditions at the interface are

$$M \cdot V_1 = -\frac{1}{iK}\partial_T W_1 + W_2\,, \tag{3.31}$$

(where M was defined in equation 3.29),

$$V_1 = \begin{bmatrix} H^{(1)} \\ \Phi_1 A_1^{(1)} \\ CH^{(1)} \end{bmatrix}, \quad W_1 = \begin{bmatrix} H \\ H \\ -K(r\Phi + CH) \end{bmatrix} = H\begin{bmatrix} 1 \\ 1 \\ -(r+1)KC \end{bmatrix}, \tag{3.32}$$

and

$$W_2 = \begin{bmatrix} -2\sin(I_1)A \\ 0 \\ 2rKC\sin(I_1)A \end{bmatrix}. \tag{3.33}$$

We define $V^T \equiv [-rCK, -CK, 1]$ where V^T is such that $V^T M = 0$. Multiplying equation (3.31) with V^T, we obtain $V^T W_1 = -2(1+r)CKH$ and $V^T W_2 = 4rCKH\sin(I_1)$. Hence, we arrive at the amplitude equation for large G.

$$\frac{1}{iK}V^T W_{1,T} = V^T W_2\,, \text{ or } H_{,T} = -iK\frac{2r}{1+r}\sin(I_1)A\,, \tag{3.34}$$

with

$$CH = 2A\cos(I_1) - J\frac{1}{\pi}\sin(I_1)\,. \tag{3.35}$$

The amplitude evolution can now be determined from equations (3.34)-(3.35).

Equations (3.34)-(3.35) can be re-written in a more familiar form

$$H_{,T} = -i\mathcal{C}_1 H + \mathcal{C}_2 J \tag{3.36}$$

$$H = \mathcal{D}_1 A + \mathcal{D}_2 J \tag{3.37}$$

where $\mathcal{C}_1, \mathcal{C}_2, \mathcal{D}_1, \mathcal{D}_2$ are coefficients determined from the solutions of the linear problem. Equations (3.36-3.37) along with the definition of J in equation (3.24), were first found (in an equivalent form) by [54] to describe the weakly non-linear evolution of a single-wave coupled to the vorticity in an inviscid critical layer, for small density ratio $r \equiv \epsilon \ll 1$, with G of order one. If the viscosity is included in his treatment by scaling viscosity $\nu \to \epsilon^3\nu$, the same equation for vorticity Z can be obtained, and his amplitude equations for $r \ll 1$ and unity G take exactly the same form as our amplitude equations for the $G \gg 1$ case. We thus focus on the general form of the amplitude equations in the next section, and present results from solving equations (3.23), (3.24) and (3.36)-(3.37). We note here that Reutov pointed out the fact that with the extra assumption $\mathcal{D}_2 = 0$ equations (3.36)-(3.37) are identical with those describing electrostatic waves in a plasma, which have already been solved numerically by [58]. We investigate the properties of the full set of the equations without this assumption in the next section.

3.4 Results

3.4.1 Preliminaries

For both cases (weak wind and small density ratio), the amplitude equations can be cast into the following more general form:

$$H_{,T} + i\mathcal{C}_1 H = i\mathcal{C}_2 J \tag{3.38}$$

$$H = \mathcal{D}_1 A + \mathcal{D}_2 J \tag{3.39}$$

$$J = \frac{K}{2\pi}\frac{U_c'}{U_c''}\int_{-\pi/K}^{+\pi/K} e^{-iKx}\int_{-\infty}^{+\infty} Z \quad dY\,dx \equiv \langle e^{-iKx} Z\rangle \tag{3.40}$$

$$Z_{,T} + U_c' Y Z_{,x} - \tilde{\Psi}_{0,x} Z_{,Y} - \nu Z_{,YY} = U_c''\tilde{\Psi}_{0,x} \tag{3.41}$$

with

$$\lim_{Y\to\infty} Z = \left[A\frac{U_c''}{2U_c'}\frac{1}{Y} + \frac{U_c''}{2U_c'^2}\frac{1}{Y^2}A_{,T}\right] e^{iKx} + c.c. \tag{3.42}$$

and

$$\tilde{\Psi}_0 = \left(Ae^{iKx} + A^* e^{-iKx}\right) \tag{3.43}$$

where the coefficient $\sin[I_1]$ from (3.20) has been absorbed in the amplitude A in (3.43).

The above equations can be interpreted as follows. Equation (3.39) expresses the continuity of the normal velocity at the interface: It imposes the constraint that the phase and amplitude of the perturbation of the surface wave (given by H) is the same as the perturbation of the wind (given by $\mathcal{D}_1 A + \mathcal{D}_2 J$) including the component that comes from the phase change at the interface. Equation (3.38) is Newton's law, or alternatively can be viewed as a statement about the continuity of pressure at the interface; it gives the growth of the amplitude H due to the out of phase component

of the pressure. Equation (3.41) gives the evolution of the vorticity inside the critical layer that determines the phase change, and involves the non-linear term $\tilde{\Psi}_{0,x}Z_{,Y}$. The coefficients $\mathcal{C}_1, \mathcal{C}_2, \mathcal{D}_1, \mathcal{D}_2, \in \Re$ are obtained from the linear theory, and are given in equations (3.20),(3.34) and (3.35). $\mathcal{C}_1$ and $\mathcal{D}_2$ are coefficients that involve correction to the real part of C due to both the gradient of the velocity at the interface $U_{,y}$ and the pressure component in phase with the traveling wave. $\mathcal{C}_2$ and $\mathcal{D}_1$ involve the part of the pressure perturbation that is out of phase with the traveling wave.

Before we start investigating the properties of the set of equations (3.38-3.41) we re-scale the amplitudes, the time scale and length scales to reduce the number of free parameters. The rescaling is carried out in appendix B, where it is shown that we can set $\mathcal{C}_1 = 0$ and $\mathcal{D}_1 = -\mathcal{C}_2 = U' = U'' = K = 1$ with no loss of generality. The two remaining independent parameters are $\mathcal{D}_2$ and ν.

Dropping the non-linear term in eq. (3.41) we obtain $J = i\pi A$ in the linear case [38]. Assuming an exponential growth rate $A = e^{\gamma T}a_1$ and $H = e^{\gamma T}a_2$, the above equation can be written as:

$$\begin{aligned} \gamma a_2 &- \pi a_1 &&= 0\,, \\ a_2 &- (1 + i\pi\mathcal{D}_2)a_1 &&= 0\,; \end{aligned} \tag{3.44}$$

the growth rate then is given by

$$\gamma = \frac{\pi}{1 + \pi^2\mathcal{D}_2^2} - i\frac{\pi^2\mathcal{D}_2}{1 + \pi^2\mathcal{D}_2^2}\,. \tag{3.45}$$

We note as an aside that there are several conservation laws at work here. First, the vorticity is conserved inside the critical layer $\langle Z\rangle_{,T} = 0$, which implies $\langle Z\rangle = 0$ since the initial Z had infinitesimal amplitude. Second, by noting that $\langle \Psi_{0,x}Z\rangle =$

$iK(J^*A - JA^*)$, one can show that the following laws hold:

$$\frac{d}{dT}\left\{|H|^2 + \langle YZ\rangle\right\} = 0\,; \tag{3.46}$$

$$\frac{d}{dT}\left\{|H|^2 - \frac{1}{2}\langle Z^2\rangle\right\} = \nu\langle Z^2_{,Y}\rangle\,; \tag{3.47}$$

$$\frac{d}{dT}\left\{\langle(\tilde{\Psi}_0 + \frac{1}{2}Y^2)Z\rangle + \mathcal{D}_2|J|^2\right\} = \nu\langle Z\rangle\,. \tag{3.48}$$

Equations (3.47), and (3.48) are conservation laws only if $\nu = 0$. In equations (3.46), (3.47), and (3.48), the integration over x was assumed to be taken first, so that we ensure the convergence of the integrals. Recalling that the velocity (in the units we are using) inside the critical layer is given by $[u - C, w] = [\epsilon Y + \epsilon^2(1/2Y^2 + \Psi_{2,Y}) + \ldots, \epsilon^2\Psi_{0,x} + \ldots]$ we can identify the first relation (eq. 3.46) as corresponding to the conservation of momentum. Combining equations (3.46) and (3.47), we obtain the conservation of enstrophy inside the critical layer,

$$\frac{d}{dT}\langle(Z)^2\rangle = -\nu\langle Z^2_{,Y}\rangle\,. \tag{3.49}$$

The third equation (3.48) can be regarded as a statement of the conservation of energy.

3.4.2 Quasi-steady state

An interesting limit in the set of our equations is when the rescaled viscosity is large enough to play a dominant role inside the critical layer. With this assumption we can drop the time derivative term in equation (3.41) [2]; Z then depends only on the

2. By using the rescaling $A \to \nu^{2/3}A$, $Z \to \nu^{1/3}Z$, $Y \to \nu^{1/3}Y$ one can show that the time derivative term is of order $\nu^{-1/3}$ smaller than the other terms.

value of A, which then makes J a function of A only. More specifically we have

$$\nu Z_{,YY} + \tilde{\Psi}_{0,x} Z_{,Y} - Y Z_{,x} = -\tilde{\Psi}_{0,x}\,; \tag{3.50}$$

by letting $A = R(T)e^{i\Theta(T)}$, $\xi = x + \Theta$ and also using the rescaling $Y = \sqrt{2}\eta R^{1/2}$, $Z = \sqrt{R/2}\hat{Z}(\xi,\eta)$ and $\chi \equiv \nu/(2R)^{3/2}$; we obtain

$$\chi \hat{Z}_{,\eta\eta} - \sin(\xi)\hat{Z}_{,\eta} - \eta \hat{Z}_{,\xi} = 2\sin(\xi)\,; \tag{3.51}$$

Equation (3.40) then becomes

$$J = \frac{1}{2\pi} R \cdot e^{i\Theta} \int_{-\infty}^{+\infty} \int_{-\pi+\Theta}^{+\pi+\Theta} e^{-i\xi} \hat{Z} d\xi d\eta = -i\frac{1}{2\pi} A \int_{-\infty}^{+\infty} \int_{-\pi}^{+\pi} \sin\xi \hat{Z} d\xi d\eta\,, \tag{3.52}$$

where the $\cos(\xi)$ term **is zero** due to reasons of symmetry. Equation 3.52 can be written as

$$J = -iA\Phi_H(\chi)\,, \text{ with } \Phi_H(\chi) = \frac{1}{2\pi} \int_{-\pi}^{+\pi} \int_{-\infty}^{+\infty} \sin\xi \hat{Z} d\eta d\xi. \tag{3.53}$$

$\Phi_H(\chi)$ was first studied numerically by [47]. Its values range from $-\pi$ for $\chi \to \infty$ to 0 for $\chi \to 0$. Its asymptotics for $\chi \to 0$ and $\chi \to \infty$ are given by

$$\Phi_H(\chi) = \begin{cases} -c_1\chi + c_2\chi^{3/2} + O(\chi^2) & \chi \ll 1 \\ -\pi + c_3\chi^{-4/3} + O(\chi^{-8/3}) & \chi \gg 1 \end{cases} \tag{3.54}$$

where $c_1 = 5.5151\ldots$, $c_2 = 4.2876\ldots$ and $c_3 = 1.6057\ldots$. The derivation for the above asymptotics can be found in [49]. The amplitude equation then can be written as

$$H_{,T} = -A\Phi_H\left(\frac{\nu}{(2|A|)^{3/2}}\right)\,, \text{ with } H = A + i\mathcal{D}_2 A\Phi_H\left(\frac{\nu}{(2|A|)^{3/2}}\right)\,.$$

We have thus ended up with an ordinary differential equation for the amplitude of the wave. Writing A in terms of R and Θ, and after some algebra, one can show that

$$\left(1+\mathcal{D}_2^2\Phi_H\tilde{\Phi}_H\right)R_{,T}=-R^2\Phi_H\,,\ \text{and}\ \left(1+\mathcal{D}_2^2\Phi_H\tilde{\Phi}_H\right)\Theta_{,T}=-\mathcal{D}_2\Phi_H\tilde{\Phi}_H\,, \quad (3.55)$$

where $\tilde{\Phi}_H=(R\Phi_H)_{,R}$. For large R at late times we can conclude that

$$|H|\sim|A|\equiv R\sim\nu T^{2/3}\ \text{and}\ \Theta\sim\nu^2T^{-1}\,. \quad (3.56)$$

This is one of the basic results of our calculations. The above limit becomes valid at later times when small scales appear inside the critical layer, even when the rescaled viscosity is smaller than one. An important implication of this result is that the amplitude grows with an algebraic power instead of the initial exponential variation. Another important feature is that the growth rate depends linearly on the viscosity, unlike the case in linear theory. In linear theory, a weak viscosity gave the same phase change "$-i\pi$", and the resulting growth rate was independent (to first order) of ν. Finally we note that the phase of the waves, Θ, goes asymptotically to zero at late times.

3.4.3 Numerical Results

Next we investigate the weakly non-linear evolution of the wave by solving equations (3.38-3.41) numerically. To solve the advection equation (3.41), we used a code which is spectral in x and finite difference in Y. The domain range we used was $(-50,50)$ in Y and $(0,2\pi)$ in x. Up to 1024 grid points were used in the Y direction and 63 modes were kept in x. Viscosity $\nu=0.1$ is used in all the simulations. The

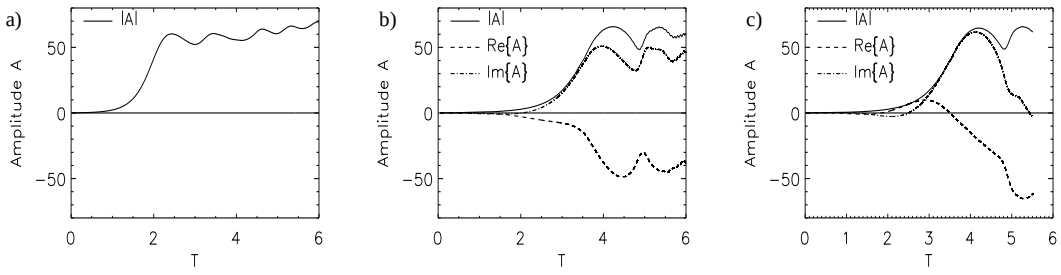

Figure 3.1: The evolution of the wave amplitude A for the cases $\mathcal{D}_2 = 0$ (panel [a]), $\mathcal{D}_2 = +0.3$ (panel [b]) $\mathcal{D}_2 = -0.3$ (panel [c]).

far-field boundary conditions ($Y \to \pm\infty$) were satisfied to order $1/Y$, although the asymptotic behavior of Z was taken into account when we evaluated the integral in equation (3.40). The code was tested by comparing with a fully pseudo-spectral code as well as with already published results.

Equations involving a critical layer have been solved numerically for various cases [59, 53, 51, 52, 58]. The nonlinear evolution of the critical layer leads to the well studied 'cats-eye' pattern. As the amplitude of the wave increases, the 'phase-change' across the critical layer is decreased to zero and the amplitude saturates up to diffusive time scales. We will focus only on the differences being introduced by the coupling of the amplitude A of the upper 'wind' perturbation with the amplitude of the wave H. Such coupling is controlled by the parameter $\mathcal{D}_2$. When $\mathcal{D}_2 = 0$ we have no feedback of the gravity wave to the critical layer 'free critical layer'; the amplitude A then is proportional to H. In figure (3.1) we plot the amplitude of the 'wind perturbation' A as a function of time for three different cases: $\mathcal{D}_2 = 0, \pm 0.3$. The saturation amplitude does not seem to strongly depend on the coupling coefficient $\mathcal{D}_2$. The phase of the amplitude ($\arg\{A\}$) does change; this corresponds to traveling vortices.

The first panel in figure (3.2) shows the temporal behavior of phase change

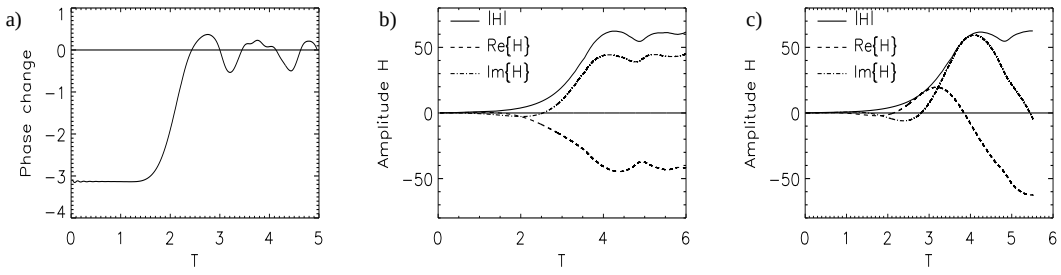

Figure 3.2: The evolution of the phase change across the critical layer as a function of time for the $\mathcal{D}_2 = 0$ case (panel [a]), and the evolution of the wave amplitude H for the cases $\mathcal{D}_2 = +0.3$ (panel [b]) and $\mathcal{D}_2 = -0.3$ (panel [c]).

$\mathrm{Im}\{-J/A\}$, which is similar for all three cases. The last two panels show the evolution of the amplitude of the wave H as a function of time for the $\mathcal{D}_2 = \pm 0.3$ cases. H has the same properties as A although the time dependence is smoother, which is expected since H can be written as a time integral of A.

Finally in figure (3.3) we display the total vorticity $Z + Y$ inside the critical layer at the non-linear stage, for the cases $\mathcal{D}_2 = 0, \pm 0.3$. The displacement of the vortices in the non-zero coupling coefficient cases indicates that the vortices are drifting with respect to the co-moving frame with the wave. Furthermore, we note the small differences in the vorticity near the separatrix between figure (3.3)(a) and figures (3.3)(b) and (c). This hints at different mixing properties induced by the coupling with the wind, which turn out to be important in the mixing properties of the flow that we examine in the next section.

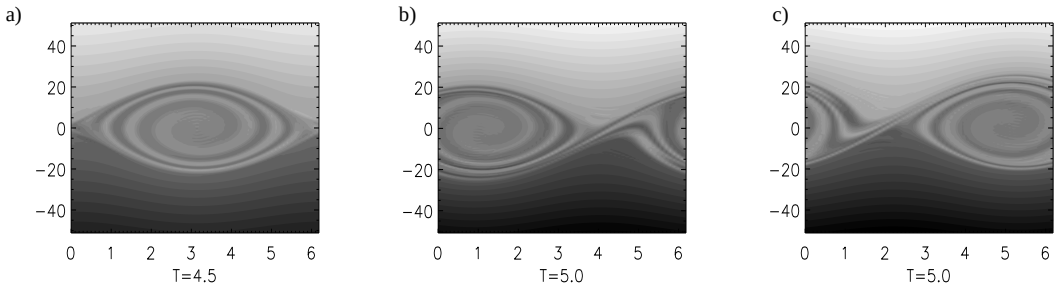

Figure 3.3: Plots of the vorticity inside the critical layer using a gray-scale representation for the vorticity for the cases $\mathcal{D}_2 = 0, +0.3, -0.3$ (panel [a,b,c] respectively).

3.5 Effect of gravity wave on chaotic mixing inside critical layers

The above analysis is originally motivated by the possibility of enhanced mixing of different fluids due to the instability of wind-driven gravity waves at the interface. Specifically in the context of nuclear runaway in novae, we are ultimately most interested in the mixing of two differentially rotating layers of distinct chemical abundances in a strong gravitational field [18]. In the strongly non-linear regime, where the surface waves break due to the wind, dimensional analysis based on preliminary numerical simulations ([18] and references therein) indicates that turbulent mixing due to breaking of wind-driven gravity waves is the key to explaining the mixing of white dwarf stellar matter into the "burning" accreted envelope on time scales consistent with the observations. Motivated by these results, we investigate in this section the effect of gravity waves on the chaotic mixing in the critical layers, before wave breaking occurs. In this case, the weakly non-linear flow is laminar everywhere, as shown in previous section; and the cat's eye vortices develop within the critical layer, with the gravity surface waves yet too weak to break. Fortunately, there already

exists a substantial body of work focused on mixing within critical layers. The aim of this section is to analyze weakly nonlinear wave-driven mixing from this perspective; we mainly focus on the qualitative aspects, and illustrate how the coupling between gravity waves and vorticity inside the critical layer alters the mixing.

Similar chaotic mixing in critical layers associated with Rossby-waves has been investigated in great detail, using a variety of approaches, and in various geophysical and plasma physics contexts [60, 61, 62]. Proper treatment of the mixing in the critical layer requires consistency in updating the velocity field, vorticity and the tracer particles [62]. The sensitivity of transport of tracer particles to their initial conditions reflects the complicated structures of manifolds commonly found in these non-integrable Hamiltonian systems [60, 61].

In previous section, we have found that, with or without coupling with surface waves, the general flow structure of the vortices is similar inside the critical layer. Such vortical structures are typical of the weakly nonlinear evolutions of parallel flows [62, 53]. However, their mixing properties may be very different (depending on the details of the underlying flow) in spite of great similarity in the general features. As pointed out in [60], the single-wave approach adopted above to derive the amplitude equations is equivalent to the pendulum approximation of a single-mode Hamiltonian system. In our amplitude equation (3.41), the vorticity Z is advected by a time-dependent pendulum flow: $(u, v) = (Y, -\Psi_{0,x})$, with $\Psi_0 \equiv Ae^{iKx} + \text{c.c.}$. Putting $A \equiv R(T)e^{i\Theta(T)}$, the particle trajectories $(x(\mathbf{x_0}; T), Y(\mathbf{x_0}; T))$ satisfy equations

$$x_{,T} = u = Y, \tag{3.57}$$

$$Y_{,T} = v = KR(T)\sin(Kx + \Theta(T)), \tag{3.58}$$

where $\mathbf{x_0} \equiv (x_0, Y_0)$ is the initial particle position.

Given the time dependence from the numerical solutions in the previous section, we can calculate the strain rate of such a flow by first linearizing equations (3.57)-(3.58) for an infinitesimal separation between two particles $\delta\mathbf{x}$,

$$\frac{d\delta\mathbf{x}}{dT} = (\delta\mathbf{x}\cdot\nabla)\mathbf{v} = \begin{pmatrix} 0 & 1 \\ K^2R\cos(Kx(\mathbf{x_0};T)+\Theta) & 0 \end{pmatrix}\delta\mathbf{x} \equiv \mathbf{A}\delta\mathbf{x} \quad . \quad (3.59)$$

λ_0, defined as the product of eigenvalues of matrix $\mathbf{A}$ in equation (3.59), is interpreted as the combination of strain and rotation: $\lambda_0(\mathbf{x_0}) = -\det(\mathbf{A}) = R\cos(Kx(\mathbf{x_0};T)+\Theta)$. During the numerical integration of equations (3.38-3.41) from $t=0$ to $t\sim 8$, we update λ_0 for each $\mathbf{x_0}$ in the computation domain as the amplitudes are updated, and we obtain λ_0 as a function of both space ($\mathbf{x_0}$) and time. We then time-average λ_0 for each $\mathbf{x_0}$ in the entire domain. The time-averaged λ_0, denoted as $\langle\lambda_0\rangle$, is a function of only the initial position $\mathbf{x_0}$ of the particle. Positive $\langle\lambda_0\rangle$ implies the likelihood for a positive Lyapunov exponent for that initial position; negative $\langle\lambda_0\rangle$ implies that rotation is dominant over strain. We have calculated the time-averaged $\langle\lambda_0\rangle$ for each initial position $\mathbf{x_0}$ in the computation domain for $\mathcal{D}_2 = 0.2$ case as shown in figure 3.4(b). Figure 3.4(b) is to be compared with figure 3.4(a), where the vorticity is decoupled from the surface wave: $\mathcal{D}_2 = 0$. More striated layers are found in figure 3.4(b), indicating more complicated tangles of manifolds due to coupling with the surface gravity wave.

The relation between $\langle\lambda_0\rangle$ and the finite time Lyapunov exponent may not be straightforward, and can depend sensitively on the prescribed flow. In general cases where the flow is time dependent, some correction to $\langle\lambda_0\rangle$ can be made so that it is closer to the Lagrangian description [63]: where Ψ is the stream function of the flow. Interestingly $\lambda_1 = 0$ in our case despite the time-dependence of the amplitudes. Thus

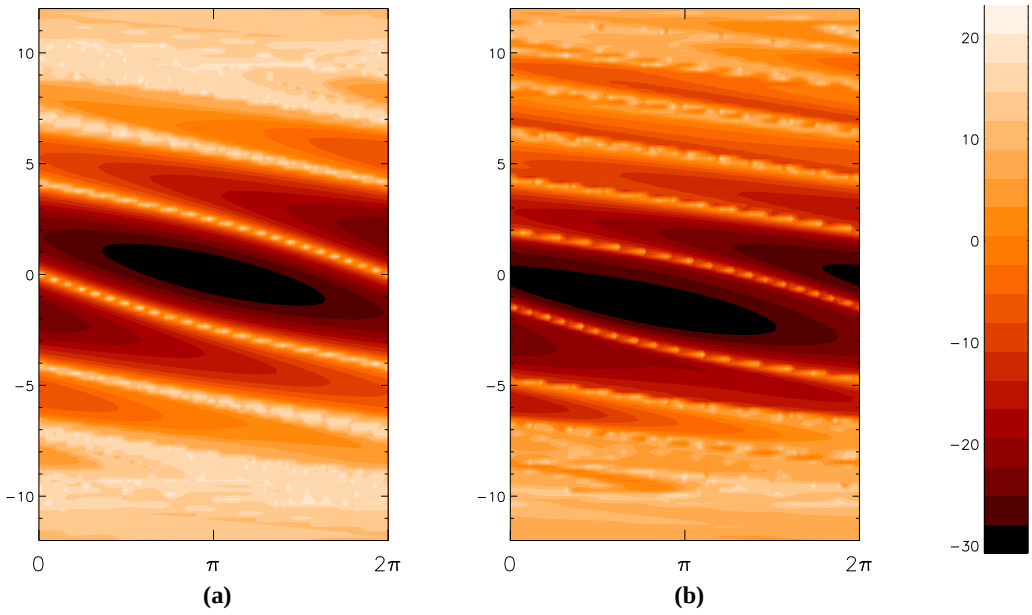

Figure 3.4: (a): $\langle\lambda_0\rangle$ for the critical layer without coupling to the gravity wave ($\mathcal{D}_2 = 0$). (b): $\langle\lambda_0\rangle$ for the critical layer coupled to the gravity wave ($\mathcal{D}_2 = 0.2$). Bright regions indicate possible positive Lyapunov exponent.

we expect $\langle\lambda_0\rangle$ to be a good indicator of the finite time Lyapunov exponent, which we have also calculated independently (figure (3.5)) for the two corresponding cases in figures (3.4)(a) and (b). Similar to dynamical systems, positive finite time Lyapunov exponents strongly suggest the presence of unstable mixing manifolds. The larger the number of positive finite time Lyapunov exponents in the system, the more chaotic the mixing is.

The spatial distribution of the finite time Lyapunov exponents (FTLE) is certainly different between figures (3.5)(a) and (b) due to the coupling of shear flow to the surface wave. However, up to time $T \sim 8$, our calculation shows that the range of positive FTLE is similar: both cases have almost identical maximum (~ 0.72) and minimum (~ -0.4) values (please note that the figure 3.6 shows the positive values of the FTLE). The relative frequency of positive FTLE is also similar (see figure 3.6),

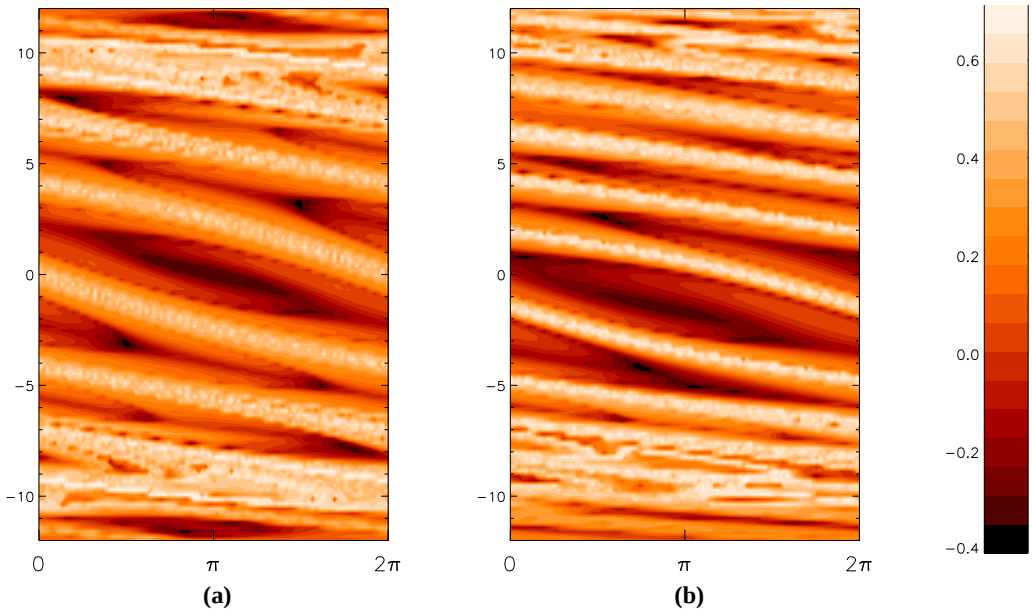

Figure 3.5: (a): Finite time Lyapunov exponent the un-coupled case $\mathcal{D}_2 = 0$. (b): Finite time Lyapunov exponent for the case $\mathcal{D}_2 = 0.2$. Bright regions indicate positive Lyapunov exponent.

with a slight difference in the variance: variance ~ 0.04 in (b), while in (a) variance ~ 0.03.

In realistic situations where the passive tracers may be weakly diffusive, the asymptotic mixing property is determined by the combination of slow diffusion and fast advection. If we define ζ as the tracer concentration, we can write down the equation for the weakly diffusive tracer in the above flow field (eqs. 3.57 and 3.58) as

$$\zeta_{,T} + Y\zeta_{,x} + R(T)\sin\left(Kx + \Theta(T)\right)\zeta_{,Y} \quad = \quad \frac{1}{\mathrm{Pe}}\nabla^2\zeta\,, \tag{3.60}$$

where $\mathrm{Pe} \equiv U_{max}l/\kappa$ is the Peclet number, with U_{max} and l the characteristic velocity and length defined in previous section, and κ the molecular diffusivity of the tracer. Among all the measures used to describe mixing of diffusive tracers in shear flows,

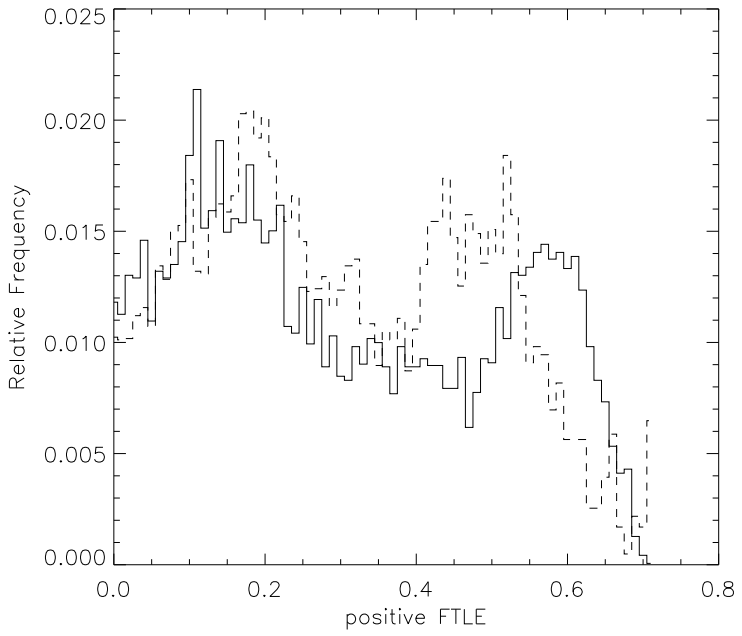

Figure 3.6: Probability distribution of the positive finite-time Lyapunov exponent. Dashed line corresponds to figure 3.5(a), and solid line corresponds to figure 3.5(b).

we focus on the stream-wise particle dispersion (variance), defined as

$$\sigma^2 \equiv \langle x^2 \rangle - \langle x \rangle^2, \tag{3.61}$$

where $\langle x \rangle$ and $\left\langle x^2 \right\rangle$ are, respectively, the first and second longitudinal moments of the concentration field ζ

$$\langle x \rangle \equiv \int x \zeta d^2x, \qquad \langle x^2 \rangle \equiv \int x^2 \zeta d^2x,$$

and we similarly define the y-variance $\sigma_y^2 \equiv \langle y^2 \rangle - \langle y \rangle^2$.

If the flow is weak and diffusion is strongly dominant over advection, particles undergo random walks and σ increases linearly with the square root of time: $\sigma = (2T/\mathrm{Pe})^{1/2}$. On the other hand, if the shear flow is strong and irregular in time,

the particles will be in a super-diffusive regime ($\sigma \sim T^{\alpha}$, $\alpha > 1$), during which the dispersion grows faster than that for ballistic transport ($\sigma \sim T$). In cases where the flow is bounded and time-independent, the super-diffusive regime eventually gives way to yet another diffusive (Taylor) regime, with a larger effective diffusivity than molecular diffusion [64]. For a time-dependent velocity field, the super-diffusive regime is the long-time limit of particle transport.

To examine how the time dependence of the flow affects diffusive particle mixing in our case, we have integrated equation (3.60) using a particle method ([64] and references therein). Due to the need to integrate equation (3.60) over long durations, we have used three models of $R(T)$ and $\Theta(T)$, resembling two classes of solutions from solving the amplitude equations (figure 3.7(a)); the first two are for the inviscid critical layer, where the amplitude oscillates around the saturated value, while the third is for a viscous critical layer, where the amplitude grows as $T^{2/3}$ asymptotically in time.

We place 10^5 particles at an initial position close to the separatrix, solve for their positions in $\Re^2$, according to equation (3.60) for $\mathrm{Pe} = 10^5$, and record their positions, from which we can calculate the particle dispersion. As pointed out in [64], the method used [65] is particularly robust for small values of the diffusion coefficient, e.g. large Peclet number. In our case (equations 3.57 and 3.58), ballistic transport is expected (and confirmed numerically) if there is no time variation in A.

Figure (3.7) illustrates the temporal characteristics of the model flow amplitudes R we used in this study: two cases corresponding to inviscid critical layers, for which the initially exponentially growing amplitude saturates to $R \sim 1$ at $T \sim 100$ and then oscillates periodically with a fluctuation amplitude of 0.2 and periods of 6 and 65, respectively; and one case corresponding to the viscous situation, in which the amplitude oscillation just discussed is replaced by an algebraic growth proportional

to $T^{2/3}$. The consequent results for our measured transverse and longitudinal particle dispersion are then shown in Figure (3.8), which provides the computed dispersion σ versus time for these three cases. We clearly see that the early time dependence of σ is verified as the diffusive regime, where $\sigma = (2T/\mathrm{Pe})^{1/2}$; and that transverse diffusion saturates, corresponding to complete transverse mixing in the critical layer. We also observe that the long time asymptotics for all cases studied are at least super-diffusive, with $\sigma \sim T^{3/2}$ for cases 1 and 2, while for case 3, where the amplitude grows as $T^{2/3}$, the dispersion is close to $\sigma \sim T^2$. This contrasts with results for Poiseuille flow, for which longitudinal diffusion asymptotes to Taylor dispersion once transverse diffusion saturates ([64]); this difference in behavior is actually expected because in our case (as opposed to the Poiseuille case) the flow amplitude continues to show temporal variations in the long-time limit.

These results are consistent with anomalous diffusion found in other two-dimensional flows by [66] that predict the $\sigma \sim T^{3/2}$ scaling for flows with KAM regions. The temporal periodicity in the flow in our first two cases creates the possibility for KAM regions to coexist with chaotic regions; and particle dispersion is in good agreement with theory. However, for the third case, the amplitude of the flow grows indefinitely with time, with no periodicity, and there do not exist any KAM regions; thus the absence of KAM regions (where particles can get trapped) and the indefinite growth of the vortices leads to particle transport that is more super-diffusive.

From the above particle simulation results, we expect that, despite the fact that the particle diffusion coefficient is the same, more diffusive particle dispersion can be found in viscous critical layers (third case in figure 3.8) than inviscid critical layers (first and second cases in figure 3.8). For the case of viscous critical layers, the single-wave asymptotic expansion eventually fails as the critical layer expands indefinitely. Thus it would be interesting to see how the mixing pattern might be altered when the

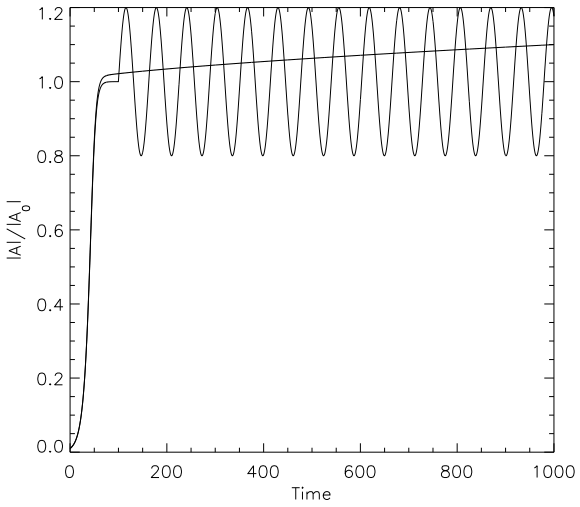

Figure 3.7: The two classes of models for the amplitude R used in calculating the particle dispersion: the first class, corresponding to inviscid critical layers, shows initial exponential growth followed by saturation to $R \sim 1$ and oscillatory behavior; the second class, corresponding to the viscous case, follows the exponential phase with algebraic growth. We show only the oscillatory case with period 65; the shorter-period (6) case looks identical but for the period of the oscillation, but cannot be easily displayed on the same time plot for reasons of graphical clarity.

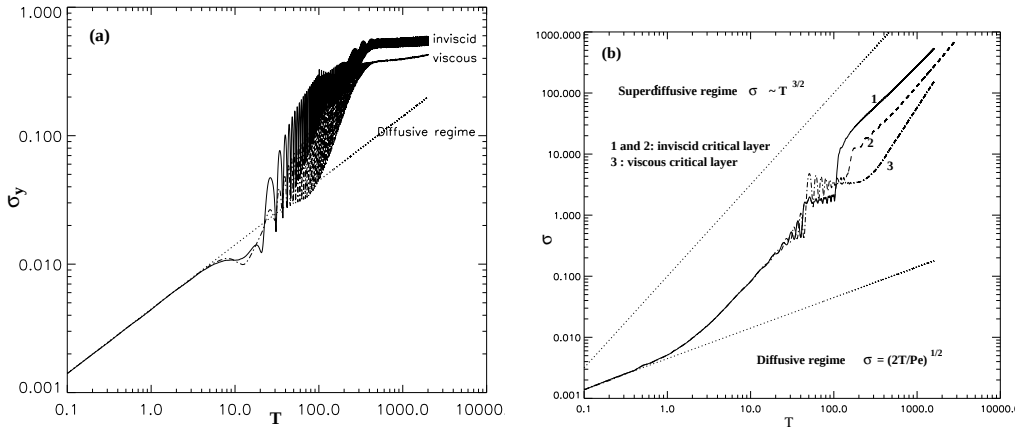

Figure 3.8: Results of our particle dispersion calculations, for the three amplitude models shown in the previous figure; in each panel, the solid line corresponds to the oscillatory case with period 6; the long dashed line for the oscillatory case with period 65; and the dash-dotted line for the viscous case, with ultimately algebraic amplitude growth. We show the particle dispersion σ in (a) the transverse direction and (b) the longitudinal direction.

critical layer comes in contact with the interface. In the case where multiple critical layers interact with each other, the ensuing mixing patterns are found to depend sensitively on various dimensionless parameters [59]. In the present case of wind-driven gravity waves, the expanding viscous critical layer may cause the surface wave to break as the critical layer expands toward the interface, leading to complicated mixing, as observed in figure 3.9 from direct numerical simulations of wind-driven gravity waves [22].

3.6 Summary of weakly non-linear theory

In this chapter, we have conducted a weakly nonlinear analysis of the resonant interaction between a wind and surface gravity waves based on the earlier linear analysis.

Our results indicate that the exponential growth of unstable resonant waves during the linear regime transits to algebraic growth in the weakly nonlinear regime. For parameters we have used to simulate the amplitude equations, the transition occurs as the surface amplitude $H \sim 60$, which translates to $h/l \sim 60e^{-3\mathcal{A}_t G}$ for the large G case, or $h/l \sim 60r^2$ for the small density ratio case. As pointed out by [54], such a transition amplitude is extremely small for the air-water case as $r = 10^{-3}$ and $h/l \sim 6 \cdot 10^{-5}$. In the weakly nonlinear regime, the algebraic growth scales to $t^{2/3}$ with a prefactor linearly proportional to the weak viscosity in the critical layer, similar to cases without coupling with gravity waves.

We have also obtained an interesting result related to mixing at the 'saddle points' connecting neighboring cat's eyes inside the critical layer; this mixing (which we studied by means of inserting Lagrangian tracers, and observing their evolution) is a consequence of the dynamics near the 'saddle', where mixing between two adjacent vortices appears to take place (see earlier related work by [60]) Such mixing regions

are commonly found in non-integrable Hamiltonian systems, and here they suggest the presence of chaotic mixing. Results from the particle analysis further confirm that chaotic mixing is a consequence of the temporal behavior of the amplitude associated with the global background flow. Even though we have assumed much simpler temporal behavior for the amplitude in our simulations, the super-diffusion found in the simpler cases affirms that more chaotic mixing should be expected as a result of the instability of the shear flow coupled to the gravity surface waves. This may imply that the entrainment rate of water vapor into air could be enhanced by the coupling of weak wind with surface waves.

At the outset of our weakly nonlinear analysis we assume the spatial domain is periodic in the stream-wise direction, and rely on the periodicity to avoid the problems of interaction between modes in the continuum without resorting to quasi-linear theory [41] or eddy viscosity models [40, 39]. Assuming that some dissipative and surface restoring force to reduce the number of unstable modes to one, we focus on such a resonant mode inside the critical layer. The periodicity assumption, albeit unrealistic in most physical situations, is advantageous for comparison between our weakly nonlinear results and direct numerical simulations. The details of this process are elucidated in the following for various relevant physical setups where our results may be applicable.

The $G \equiv gl/U^2 \gg 1$ assumption can be relevant in astrophysics, where gravity is very large compared to convection 'winds' in the convection zone, or to the accretion flow on the white dwarf surface. However, there exists no capillary force in astrophysics. Magnetic fields aligned with the interface act similarly as the surface tension, yet the resultant dispersion relation is different; unlike surface tension the phase velocity of the waves does not increase with the wave number but instead saturates at the Alfven speed. Therefore, contrary to the case with surface tension, modes with

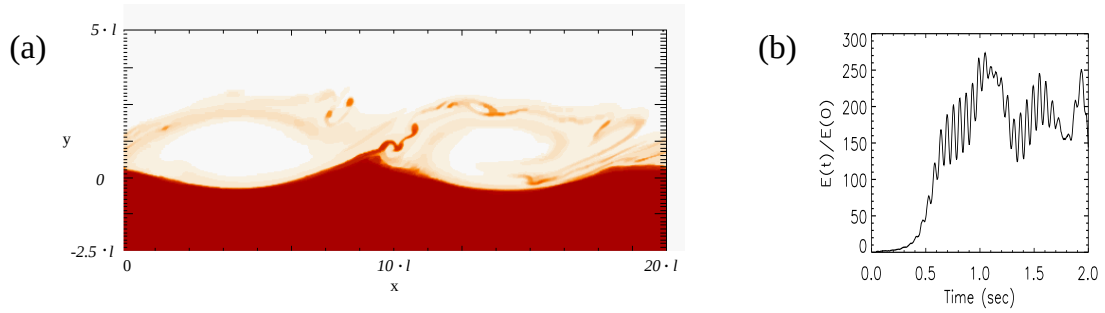

Figure 3.9: Results from direct numerical simulations with $G = 0.1$ and $r = 0.1$, obtained at a (dimensional) time of $\sim$1 sec. Density contour plot of a wind driven gravity wave are shown in panel a); panel b) shows the energy of the wave as a function of time.

large wave numbers are not neutralized or damped completely by magnetic fields, but their growth rate decreases exponentially with wave number. Thus, in the case of a magnetized plasma, we would also need to further assume that the most unstable mode is much more "dominant" than any other mode in the continuum in order to apply our results to astrophysics. In terrestrial situations, the condition $G \gg 1$ can be met in liquid interfaces for large length scale of the wind ($l \gg U^2/g$) provided that the constraint $4\mathcal{T}G < (r+1)^2/(1-r)$ for instability is satisfied. For the small density ratio case ($r \ll 1$), the periodicity assumption and the criterion for surface tension to damp all the modes except the most unstable mode result in a range of the maximum wind velocity within which our weakly nonlinear results apply to small density ratio cases: $0.2\ \mathrm{m\,s^{-1}} < U_{\max} < 1\ \mathrm{m\,s^{-1}}$ for the air-water case.

We further remark that, as found in the case of an internal boundary layer [59], a similar non-linear development of the vorticity in the critical layer and its ensuing expansion are also observed in direct numerical simulations for parameters well beyond the range suitable for weakly nonlinear analysis. Figure 3.9 illustrates such an example obtained from direct numerical simulation of wind-driven gravity waves

with $G = 0.1$ and $r = 0.1$, no surface tension, and an initial maximum Mach number of $U_{max}/C_{sound} = 0.2$ [22]. We note that while the characteristic parameters are beyond the range for weakly nonlinear analysis, the fully nonlinear results bear a strong similarity to the weakly nonlinear results discussed earlier. Thus, the cat's eye vorticity shown in figure 3.3 resembles the contour of scalar density field in panel a), even though the vorticity has already expanded right above the interface. The temporal evolution of the wave energy shown in panel b). Despite the fast oscillations due to sound waves emitting from the reflecting bottom boundary, the temporal variation behaves similarly to the amplitude H for the weakly nonlinear case shown in figure 3.2 if the fast sound wave oscillations are filtered. Here it is especially notable that while the temporal evolution in these two rather different cases bear a remarkable resemblance, the physics underlying the saturation in these two cases is quite different: contrary to the weakly nonlinear case, the saturation in the fully nonlinear calculations results from the fact that the critical layer both broadens substantially and descends onto the interface (panel a); this behavior and strongly suggests that in this nonlinear regime, saturation is largely a consequence of the broadening of the resonant layer, and consequent decreased coupling between the wind and the perturbed interface. Thus, we see that the saturation mechanism is likely to depend on details of the specific parameter regime governing the shear layer; this is an issue we intend to pursue in much more detail in subsequent studies.

Finally, we note a number of interesting additional issues that remain to be investigated. For example, while we have focused on mixing above the interface, mixing below the interface can also have important astrophysical consequences; this is principally because (for example) mixing H and He in to C/O of the white dwarf star can lead to nuclear burning in the upper layers of the star itself, which may significantly affect the stratification of the interface layer (because then the dynamics of the lat-

ter layer may resemble much more closely what occurs in atmospheres heated from below (e.g., the solar photospheric case). Similarly, sub-surface currents in (possibly due to sub-surface convection) can also significantly couple to the interface instability [67, 68, 69].

CHAPTER 4

NUMERICAL SIMULATIONS

4.1 Introduction

So far we have examined the linear and weakly non-linear theory for the generation of waves. However, these theories are based on the assumption of small amplitude waves and give little direct information about mixing, which is largely governed by nonlinear processes. To our knowledge the fully nonlinear evolution of the resonant instability has not been previously studied with numerical simulations for either the case of the ocean or the astrophysical problem. The oceanographic problem is difficult to address numerically both because the density ratio is very small ($\rho_{\rm air}/\rho_{\rm water} = 10^{-3}$) making the growth time scale one thousand times smaller than the wave period, and because surface tension plays a key role in the spray formation. Nonetheless, there have been studies [70] on the growth of waves for a given pressure distribution at the interface given by Miles theory; similarly [71, 72] have investigated boundary layer simulations in the presence of a wavy boundary and studied the effect of "waves" on the wind profile. Present computational resources make more detailed modeling of the oceanographic problem with numerical simulations difficult. However, it is possible to address the astrophysical problem for a range of relatively strong winds.

In this chapter we present results of the fully nonlinear problem of wind driven gravity waves for fixed density ratio of $\rho_1/\rho_2 = 0.1$. The simulations in this study were performed using the FLASH code [73, 74, 75], a parallel, adaptive-mesh hydrodynamics code for the compressible flows found in astrophysical environments.

In the next section 4.2 we present the physical setup used in our simulation studies and the equations of motion. In section 4.3 we present known results from the theory

of free traveling waves. In 4.4 we discuss the numerical code used for the simulations, and in 4.5 we present the table of our runs and justify the choice of the parameter space we examine. Section 4.6 presents results about the wave dynamics we observe. In section 4.7 we present and discuss our results about mixing and in section 4.8 we present our convergence studies. We summarize and draw our conclusions in section 4.9.

4.2 Initial setup and evolution equations

We consider a two-dimensional square box of size $l_y = l_x$, with two layers of compressible fluid in hydrostatic equilibrium separated by a sharp interface located at $l_y/2$. The densities of the fluids are ρ_1 immediately above the interface and ρ_2 immediately below, with $\rho_1 < \rho_2$. There is a uniform gravitational field $\mathbf{g}$ in the negative y-direction. The upper fluid moves in the x-direction with a velocity given by $U(y)$, where $y = 0$ corresponds to the location of the unperturbed interface. The exact form of $U(y)$ used is:

$$U(y) = U_{\max}\left(1 - e^{-y/\delta}\right) \tag{4.1}$$

A sketch of the wind profile is shown in figure 2.1 c).

The equations we evolve are the compressible Euler equations for inviscid flow,

$$\frac{\partial \rho}{\partial t} + \nabla \cdot \rho \mathbf{v} = 0 \ , \tag{4.2}$$

$$\frac{\partial \rho \mathbf{v}}{\partial t} + \nabla \cdot \rho \mathbf{v}\mathbf{v} + \nabla P = \rho \mathbf{g} \ , \tag{4.3}$$

$$\frac{\partial \rho E}{\partial t} + \nabla \cdot (\rho E + P)\,\mathbf{v} = \rho \mathbf{v} \cdot \mathbf{g} \ . \tag{4.4}$$

where ρ is the density, $\mathbf{v}$ is the fluid velocity, P is the pressure, and $\mathbf{g}$ is the acceleration

due to gravity. E is the total specific energy, composed of the specific internal energy ϵ and the kinetic energy per unit mass,

$$E = \epsilon + \frac{1}{2}v^2 \ . \tag{4.5}$$

The system of equations must be closed by an equation of state of the form $P = P(\rho, \epsilon)$, for which we use a simple gamma law,

$$P = (\gamma - 1)\,\rho\epsilon \ . \tag{4.6}$$

The initial density and pressure profiles were obtained by integrating the equation of hydrostatic equilibrium in an isotropic atmosphere,

$$\frac{dP}{dy} = -\rho g \hat{y} \ , \tag{4.7}$$

which for the case of a compressible, gamma-law gas gives

$$\rho|_{t=0} = \rho_i \left[1 - (\gamma - 1)\,\frac{g\rho_i y}{P_0 \gamma}\right]^{\frac{1}{\gamma - 1}} \quad \text{and} \quad P = P_0 \left(\frac{\rho}{\rho_i}\right)^{\gamma} . \tag{4.8}$$

Here P_0 is the pressure at the interface and $\rho_{i=1,2}$ is the density immediately above or below the interface.

A passive scalar X representing the mass fraction of a species[1], is advected by:

$$\frac{\partial \rho X}{\partial t} + \nabla \cdot \rho X \mathbf{v} = 0 \, . \tag{4.9}$$

1. The mass fraction $X_i(t, \mathbf{x})$ of a species i, represents the ratio of the mass m_i of the species i included in an infinitesimal volume element located at $\mathbf{x}$ at time t, to the total mass m included in the same volume element.

In this setup we introduce the passive scalar X representing the mass fraction of the lower fluid so that X takes initially the value 1 below the interface and 0 above.

We use periodic boundary conditions in the x-direction and hydrostatic, stress-free boundary conditions in the y-direction [76]. We note that we perform "run down" simulations in the sense that after the initial conditions are set, no additional forcing is used to maintain the wind flow.

The non-dimensional numbers involved are $G = g\delta/U_{\max}^2$ which gives a measure of the strength of the wind (G is related to the Froude number F as $G = F^{-2}$), the density ratio $r = \rho_1/\rho_2$ right above and below the interface (or equivalently the Atwood number $\mathcal{A}_t = (1-r)/(1+r)$) and the Mach number given by $\mathsf{Ma} = U_{\max}/C_{\rm s}$, where $C_{\rm s}$ is the sound speed in the upper fluid given by $C_{\rm s} = \sqrt{\gamma\frac{P}{\rho_1}}$. Two additional numbers appear due to the finiteness of our calculation. The first one is $L = l_x g/U^2$ which is a measure of the size of the box we are using. The second one is N, which gives the size of our grid for each spatial direction. The effective Reynolds number of the flow is is an increasing function of N, although an exact relation between the two is hard to obtain.

We used simple sinusoidal perturbations of small amplitude to initialize the gravity waves. For single-mode calculations the perturbed interface was written as

$$h(x) = A\cos(k_0 x) \tag{4.10}$$

where $k_0 = 2\pi/l_x$ is the smallest wave number that fits the computational domain and A is the amplitude of the wave. In the lower fluid the perturbation of the velocity was decreasing exponentially according the results of the linear theory. In the upper fluid the velocity perturbations were modeled so as to mimic the eigenfunctions of the linear problem. Ak_0 was set to 0.05. For multi-mode perturbations, a superposition

of different modes was used with random phases. The exact form of the interface is

$$h(x) = \sum A_k \cos(kx + \phi_r) \tag{4.11}$$

where ϕ_r is a random function and and the amplitude A_k of each excited mode is given by $A_k = C_{k_{\max}} k e^{-k/k_{\max}}$. $C_{k_{\max}}$ is a normalizing coefficient keeping the total amplitude of the perturbation equal to 0.05. $k_{\max}$ was set to $2k_0$ for all runs except those in which the effect of the initial spectrum was studied. For all simulations, we kept r fixed at 0.1 and tried to minimize the effects of compressibility by keeping $\mathsf{Ma} = 0.2$. Our principal aim, therefore, is to investigate how gravity wave generation and mixing is affected as we change the parameter G in the limits $L \to \infty$ and $N \to \infty$.

4.3 Finite amplitude free waves

There are many known results about finite amplitude free waves (no driving) that are found to be relevant in our research. Before presenting our results from the numerical simulations we review some of the properties of free (no wind) irrotational finite amplitude waves. It has been known for some time [77] that the Stokes equations for irrotational flows have solutions of traveling gravity waves. These have been evaluated and tabulated in [78]. There is a highest amplitude, given by $A \cdot k$=0.4432, for which gravity wave solutions exist. At this amplitude the waves form a singular crest such that the radius of the curvature of the interface at the crest goes to zero, forming a corner with opening angle of 120 degrees. The stability properties of these waves have been studied extensively by [79] and references therein. It has been shown that the crest of the waves is subject to various instabilities. Subharmonic instabilities

appear in front of the crest of the wave when the amplitude of the wave is larger than $A \cdot k$=0.4292. However, when superharmonic instabilities are allowed (more than one wavelength in the computational domain is considered) the crests of the waves become unstable at much smaller amplitudes [80]. The nonlinear development of the instabilities has been shown to lead to breaking of the crest [81]. In our simulations the gravity waves are close to irrotational since the initial perturbation has no vorticity and vorticity is conserved up to viscous time scales (in the absence of boundary layers). There are similarities therefore in our simulations with the free wave theory. In particular most of the instabilities described by [79] are present in our simulations as secondary instabilities in the fully developed waves, with direct impact on the mixing properties of the flow. However the presence of wind results in differences of the nonlinear development of this secondary instabilities even for slowly growing waves (weak winds), especially at structures in the breaking crest.

4.4 Numerical Method

All the numerical simulations described in this paper were performed using the FLASH code. The FLASH code is a parallel, adaptive-mesh simulation code for studying multi-dimensional compressible reactive flows in astrophysical environments. It uses a customized version of the PARAMESH library [82, 83] to manage a block-structured adaptive grid, adding resolution elements in areas of complex flow. The current models used for simulations assume that the flow is described by the Euler equations for compressible, inviscid flow. FLASH regularizes and solves these equations by an explicit, directionally split method, carrying a separate advection equation for the partial density of each chemical or nuclear species (scalars) as required for reactive flows. The code does not explicitly track interfaces between fluids. As a result,

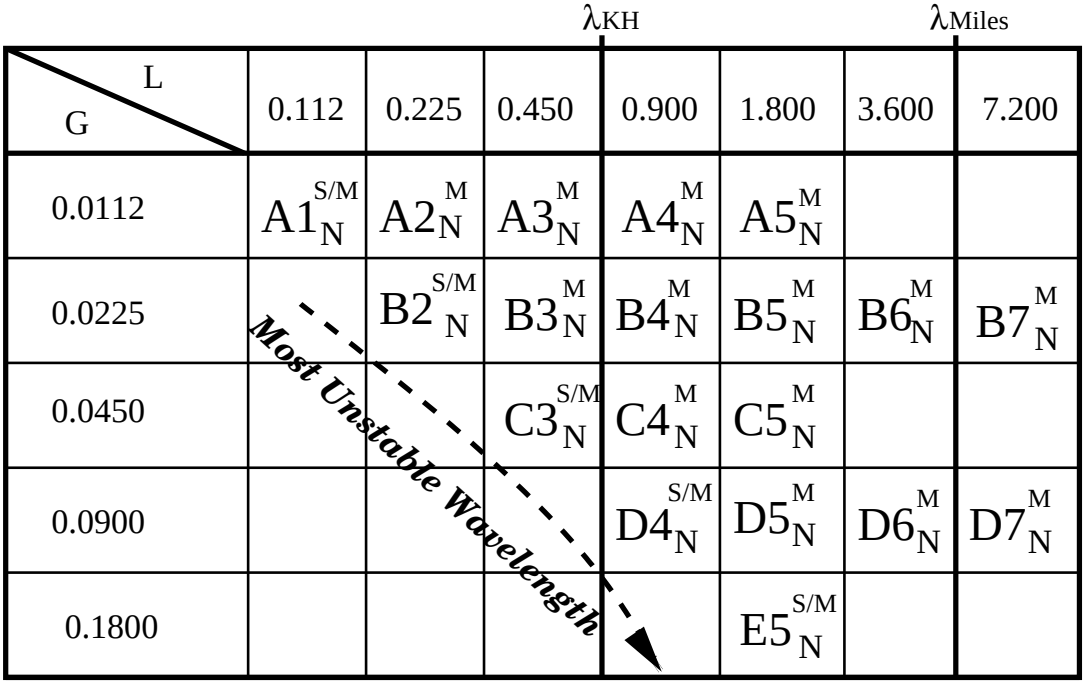

Figure 4.1: The parameter space spanned by our runs. Each block in this diagram corresponds to a set of different runs with different resolution N. The $x-$axis gives the size of the computational domain measured in units of $(U_{\max}^2/g)$; the y-axis gives the value of $G \equiv g\delta/U_{\max}^2$. The dashed line indicates the wavelength of the most unstable mode for a given value of G. The index S/M indicates whether a single mode or multimode perturbation was imposed.

mixing occurs on grid-spacing scales exclusively due to numerical diffusion; the rate of this diffusion is a decreasing function of resolution, but is also a function of flow speeds and structure. Complete details concerning the algorithms used in the code, the structure of the code, selected verification tests, and performance may be found in [73], [74] and [75].

4.5 Numerical simulations

Figure 4.1 illustrates the parameter space spanned by our simulations. Each block in this diagram corresponds to a set of different runs. The horizontal axis indicates

the size of the computational domain in terms of the non-dimensional number L. The value of L in each column differs from the previous one by a factor of 2. The vertical axis corresponds to the parameter G. Again as we move down in the diagram G is increasing by powers of 2. G ranged from $G = 0.01125$ to $G = 0.18$. The dashed line shows the location of the most unstable wave number, as predicted by the linear theory. The two vertical thick lines show the location of the two maximum wavelengths given by the KH theory (λ_{KH} from equation 2.24) and via Miles theory (λ_R from equation 2.28). Modes with wavelength to the right of each line are stable to the corresponding instability. The growth rate from linear theory as a function of the wave number is shown in figure 4.2 for the five values of G we are investigating. For each location in the diagram more than one simulation has been performed with different grid size. The index N corresponds to the number of grid points in each direction; N ranged from 64 to 2048. Furthermore, we tested for sensitivity of our results to the initial conditions by carrying out runs with varying spectrum of the initial wave perturbation. The superscripts M/S indicates whether a single mode (S) or a random multimode (M) perturbation was used at $t = 0$. The strategy followed in our numerical simulations was to start from a computational domain the size of the most unstable wavelength for a given value of G and move to the right in the diagram (increasing L). The details of each run will be presented along with our results.

At this point we should comment on the computational limitations of the system we are investigating. First of all we cannot make runs for very large L (too far to the right in our diagram) because in order to resolve the most unstable wave length we must increase the size of our grid. For similar reasons, we cannot investigate very large values of the parameter G (too far down in the diagram) because the growth rate of the unstable modes becomes very small compared to the wave period and the diffusive time scale, the wavelength of the most unstable mode becomes larger

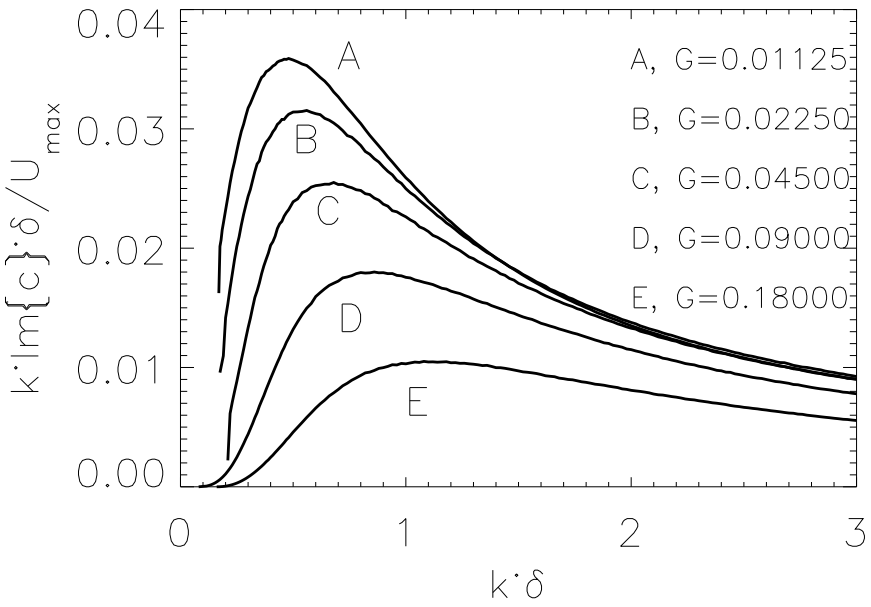

Figure 4.2: The linear growth rate as a function of the wave number. Each curve corresponds to a different value of $G \equiv g\delta/U_{\max}^2$ used in our simulations.

and as is shown later, more resolution is required to capture the physics of the wave breaking.

4.6 Wave dynamics

4.6.1 Comparison with theory

In the first part of our investigation we focus on the formation and nonlinear development of the gravity waves. In order to verify the code we compare the growth rates of the gravity waves from the simulations with the ones predicted by the linear theory. In figure 4.3 we show the potential energy of the gravity waves at the early stages as a function of time for different values of the parameter G. The results are from the runs $A1_{512}^S$, $B2_{512}^S$, $C3_{512}^S$, $D4_{512}^S$ and $E5_{512}^S$ for a single mode perturbation. Density plots of these runs can be seen in figure 4.5 which we discuss later. The potential

energy of the gravity wave was evaluated based on the integral

$$E_p = \frac{1}{2}(\rho_2 - \rho_1) g \int h(x)^2 dx \tag{4.12}$$

where $h(x)$ is the location of the interface, defined as the contour line where $\rho(y) = 0.98\rho_2$. Equation 4.12 was derived by integrating ρy over space and assuming that the wave amplitude is much smaller than the pressure scale height. We note that this method was the least noisy method to calculate the gravity wave potential energy in the linear regime. A direct integration over the whole computational domain for the evaluation of the potential energy was far too noisy. The results from the simulations for the evolution of the potential energy of the gravity waves as a function of the rescaled time tU/δ (from now on we drop the index 'max' from $U_{\max}$ for clarity) are shown in figure 4.3 where they are compared with linear theory predictions. They are found to be in satisfactory agreement with the theory.

It would be useful to further verify our code using the results of weakly nonlinear theory. However, computational limitations did not allow us to reach close to the asymptotic regime $G \gg 1$ required so that the comparison is justified. Nonetheless a qualitative comparison can be made. In the two panels in figure 4.4 show a comparison of two advected fields: the vorticity as predicted by weakly nonlinear theory in panel (a) and density from our numerical simulations in panel (b). There is similarity in the structure of the two fields although more small scale structure appears in panel (b).

4.6.2 Nonlinear evolution

Next we discuss the results from the simulations when the system is far away from linearity. We present first the single-mode runs $A1^S_{512}$, $B2^S_{512}$, $C3^S_{512}$, $D4^S_{512}$ and

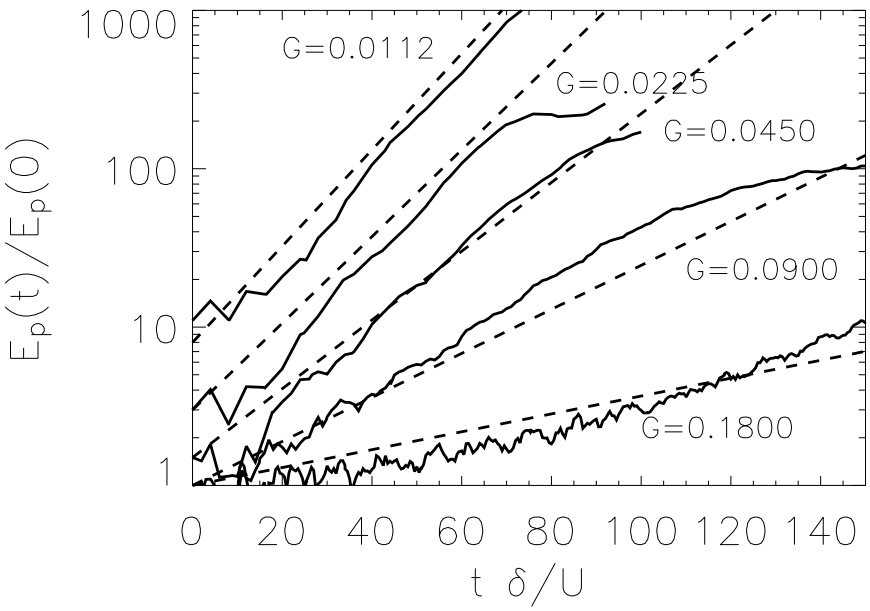

Figure 4.3: Comparison of the observed growth rate with the linear theory. The solid black lines show the evolution with time of the potential energy $E_p(t)$ of gravity waves calculated from the numerical simulations $A1^S_{512}$, $B2^S_{512}$, $C3^S_{512}$, $D4^S_{512}$, $E5^S_{512}$. The dashed lines give the linear theory predictions. The first three lines have been shifted up for clarity.

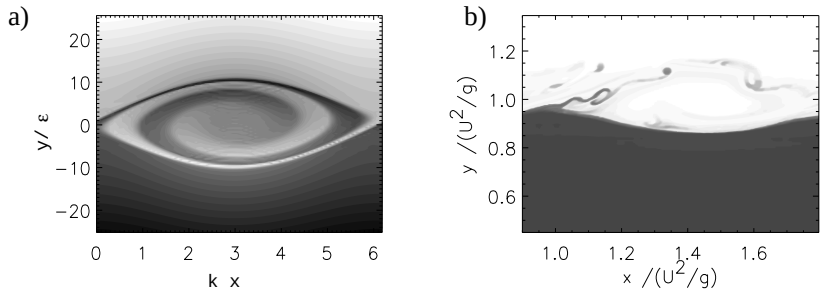

Figure 4.4: A qualitative comparison of structure between weakly non-linear theory and the numerical simulations. Panel (a) shows a contour plot of the vorticity as predicted by weakly non-linear theory. Panel (a) shows a contour plot of density from our numerical simulations.

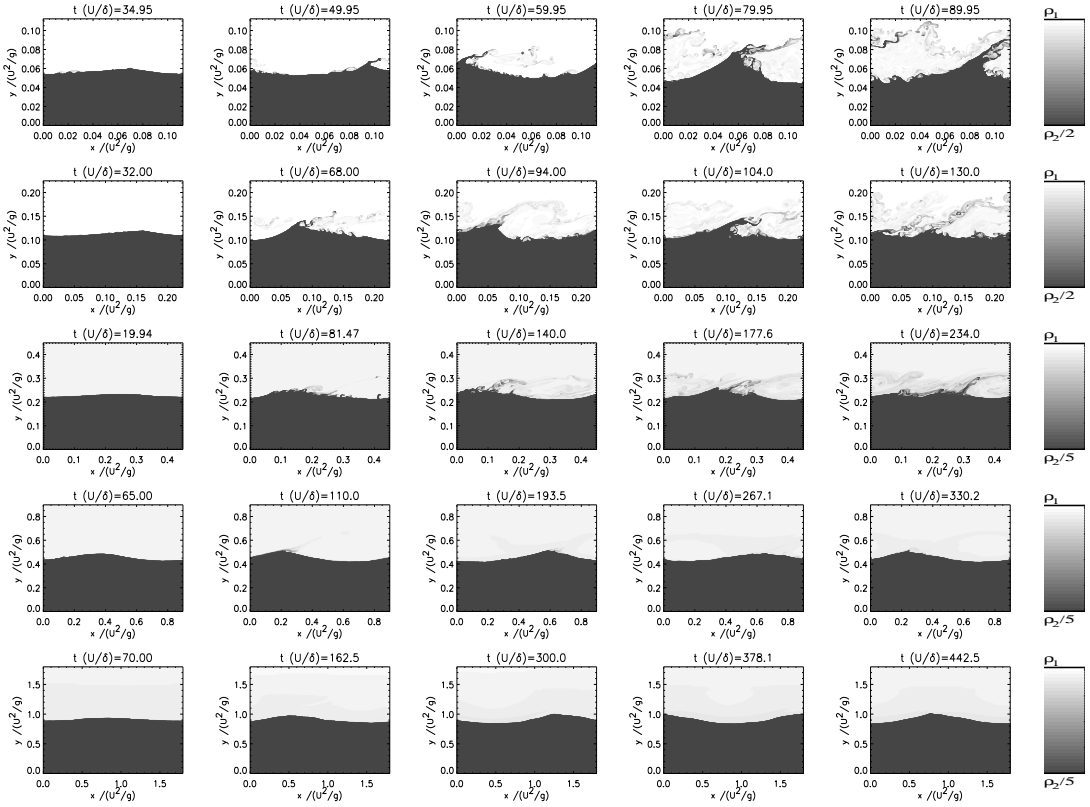

Figure 4.5: Waves forming for single mode initial perturbations for different values of G. The grey scale represents density. Each row corresponds to a different value of G (starting from the smallest value in the top row) $G = 0.0112, 0.0225, 0.0450, 0.0900, 0.1800$; time increases from left to right. The computational domain is arranged so that the largest wavelength is close to the most unstable mode.

$E5^S_{512}$. In each simulation a single mode was excited with wavelength equal to the box length. With this choice we are examining the evolution of the mode close to the most unstable one for each value of G. The panels in figure 4.5 are density plots that show the time evolution of the forming wave. Each row corresponds to a different value of G and each column represents a different time.

There is a difference in the structures that appear as we increase the parameter G. For the smaller values of G we observe that as the wave grows at some point

in time it forms a breaking cusp and material start mixing. As time progresses, the wave becomes very oblique with amplitude larger that what the theory of the highest wave predicts [79]. The wave is then forced to overturn, leading to the generation of small scale structure and strong mixing.

As we increase the value of G, waves grow more slowly as predicted by linear theory. In run $D4^{S}_{512}$ the wave reaches a maximum amplitude and a cusp is formed. We note that this amplitude is smaller than that predicted by [77] who assumed in his analysis that there was no upper fluid. The profile of the interface strongly resembles those calculated for irrotational waves by [78] for amplitudes close to the maximal one. The opening angle is roughly estimated to be 136^{o}, which is close to, but a little wider than the one predicted by [77]. Figure 4.6 shows a density plot of a wave about to break, where we show the opening angle. We note that due to the presence of the wind there is an asymmetry with respect to front and the back of the wave (i.e. the wave is tilted forward). The development of the cusp instabilities and the further input of energy from the wind leads to the ejection of material from the cusp at aperiodic time intervals. The ejected material diffuses in an eddy turnover time in the upper fluid. At each ejection, the amplitude of the wave drops. The wave resumes growing, forming a new cusp that again leads to the ejection of new material, and so on. Finally, in the last row of figure 4.5, $G = 0.18$, it appears that almost no cusp formation or mixing is present. As we will show later in the resolution studies, this is an effect of low resolution that suppresses the cusp instabilities we mentioned before[2].

There is an interesting interpretation of the above described results related to

2. In finite-difference-based or finite-volume-based simulations, the appearance of instabilities - such as cusp formation- can critically depend on the (effective) grid resolution. This fact is a strong motivation underlying the resolution studies presented later on.

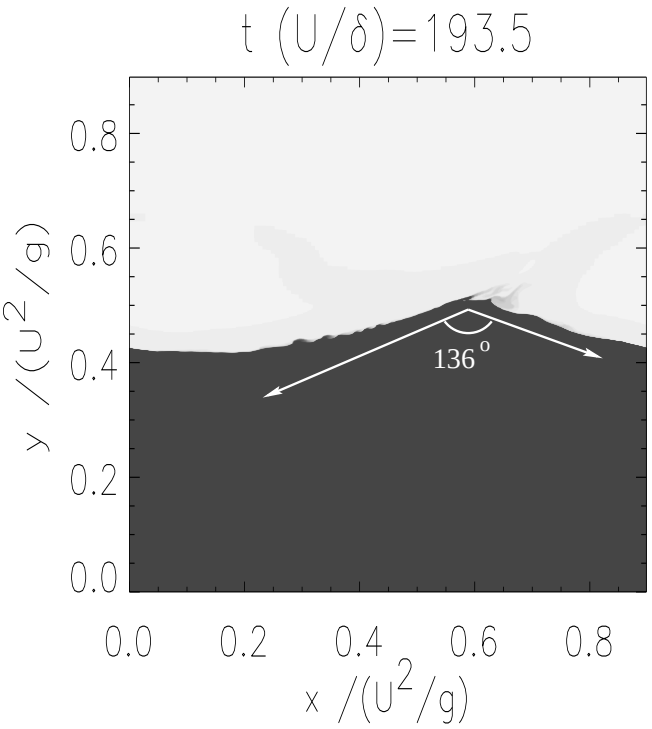

Figure 4.6: The structure of the wave near cusp-breaking. The wave just before breaking forms a cusp of angle $\sim 136^o$. The amplitude of the wave at this point is $Ak = 0.35$. The presence of the wind makes the breaking possible at smaller values of the amplitude than what the theory of free waves predicts.

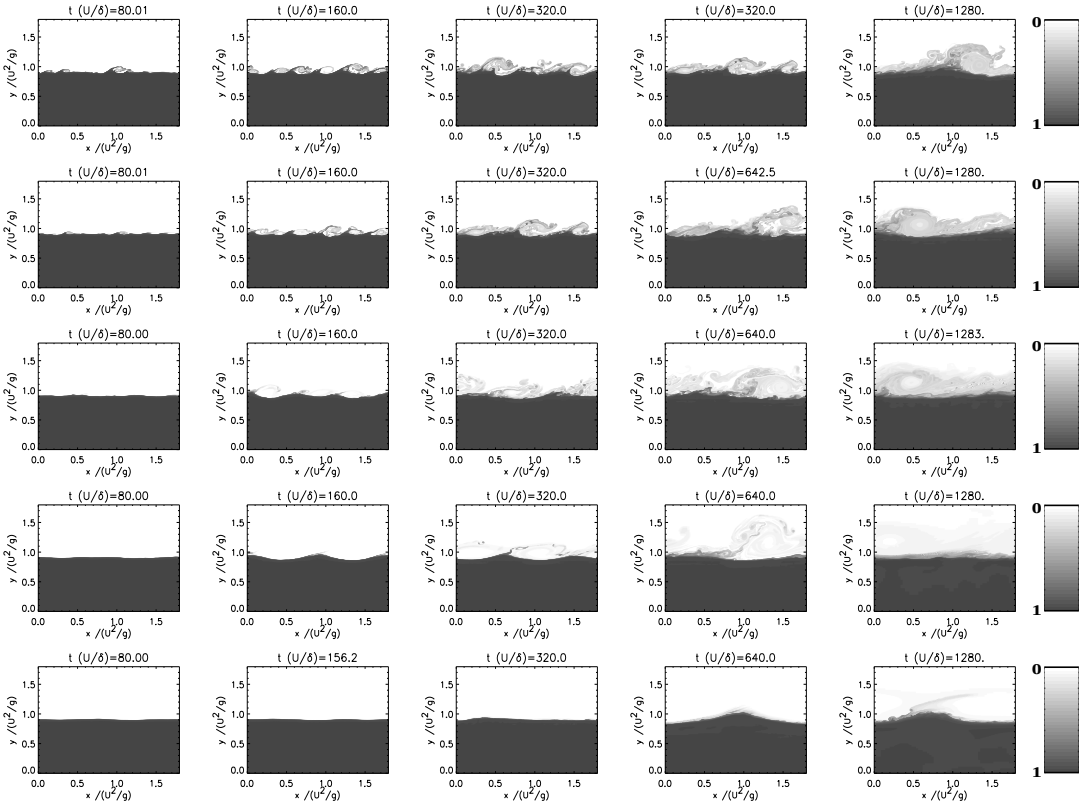

Figure 4.7: Waves forming for different G and the same L with random multimode perturbations. The grey scale represents the mass fraction X Each row corresponds to a different value of G (starting from the smallest value in the top row) $G = 0.0112, 0.0225, 0.0450, 0.0900, 0.1800$; time increases from left to right. The computational domain for all figures shown here is $L = 1.8$.

the two instabilities (KH and resonant) described in the linear theory. For the runs $A1^S_{512}$, $B2^S_{512}$, $C3^S_{512}$ (where the first mechanism appears to be more dominant) the wavelength of the most unstable wave is smaller than the maximum wavelength λ_{KH} predicted by KH theory. On the other hand for the runs $D4^S_{512}$, $E5^S_{512}$ where only cusp breaking or no mixing at all is observed, the most unstable wavelength is larger than λ_{KH}. The minimum wave number predicted from KH can therefore be interpreted as a criterion for overturning to occur.

Important differences appear when we move to multimode perturbations and com-

putational boxes larger than the most unstable wavelength. There are two main reasons for this: the first is that larger boxes allow for vortex merging, which affects the dynamics of the waves; and second reason is that super-harmonic instabilities lead to cusp-breaking at smaller amplitudes than for cases in which only a single wave period is considered [80]. Figure 4.7 shows contour plots of the mass fraction of the lower fluid X from the evolution of the runs $A5^M_{512}$, $B5^M_{512}$, $C5^M_{512}$, $D5^M_{512}$ and $E5^M_{512}$. All runs have the same multimode perturbation as described in §2 and the same box size L and resolution N. In the first three rows mixing is initiated by the over turning of small waves (most unstable ones), and A thin mixed layer is formed. Vortices merge exciting larger wavelengths, that themselves overturn leading to a wider mixed layer. This procedure continues until wavelengths larger than λ_{KH} are excited. Mixing then continues at a smaller rate in a mechanism that resembles cusp-breaking, although an interface cannot be defined in this case. It is worth noting that at the end, the largest wavelength mode is dominant, implying that the two-dimensional cascade has influenced our results.

For larger G, modes with large wavelength appear to be dominant from the beginning. In particular, the mode with $l_x/\lambda = k\delta L/2\pi = 2$ (two waves in the box) is dominant at the beginning of the $D5^M_{512}$ run and the mode with $l_x/\lambda = 1$ for the run $E5^M_{512}$. We note that linear theory predicts that the most unstable wavelength has $l_x/\lambda \simeq 2.5$ for the $D5^M_{512}$ run and $l_x/\lambda \simeq 1.7$ for the $E5^M_{512}$ run for incompressible flows, which is close considering that the ratio l_x/λ in our setup can take only integer values. Further more mixing seems to be suppressed for the $E5^M_{512}$ run until late times, while the run $D5^M_{512}$ forms breaking cusps that eject material in the upper fluid that can be clearly seen in the third panel of the fourth row in figure 4.7. We note that there is more mixing than the single mode run with the same value of G because, as we discussed in section 4.3, the presence of superharmonic instabilities

force the cusps to break at smaller wave amplitudes. At the end of this run the two waves have merged into one.

We focus further on the run $D5^{M}_{512}$, which has interesting properties regarding the evolution of superharmonic perturbations. The configuration of two traveling waves shown in the first three panels of the fourth row of figure 4.7 appears to be stable to small perturbations (noise) since it remains at this configuration for some time. Superharmonic instabilities, although leading to more cusp-breaking do not destroy the two vortex configuration initially. However at some point in time the two vortices do merge, exciting the mode with wavelength equal to the box size. Significant amount of mixing happens at that point. We further investigate the run $D5^{M}_{512}$ by introducing a different perturbation at $t = 0$. The spectrum of the perturbation was of the same functional form as in equation 4.11 except the peak of the spectrum took the values $k_{\max} = 2k_0, 3k_0, 4k_0, 5k_0$. The first case corresponds to the previously described run. Although the same mode ($k = 2k_0$) appears to be dominant at the beginning, the time at which the two vortices merged into one was different for each run and varied from $200\delta/U$ to $500\delta/U$. We note that there was no systematic correlation of the merging time with $k_{\max}$. Figure 4.8 shows the evolution of the potential energy for these runs. The diamonds indicate where the two vortices merged.

We note finally that although one can trust the 2-dimensional assumption when mixing starts, three-dimensional effects may well become important when vortex merging happens. Thus vortex merging can be the result of the two-dimensional inverse cascade, and might not take place in a three dimensional setup resulting in a different structure of the mixing zone for the 3-D case. The behavior therefore of the 2-D runs must be compared with 3-D runs in order to resolve this issue.

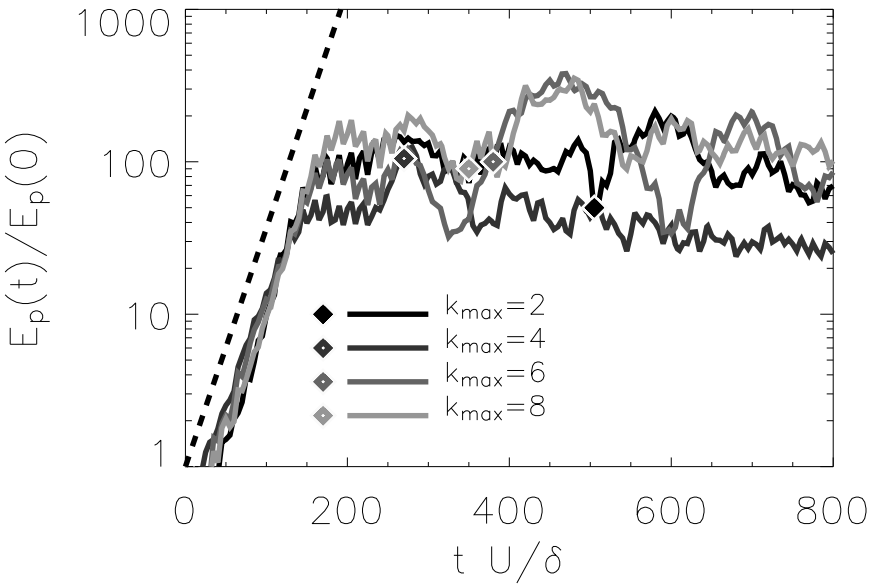

Figure 4.8: The evolution of the gravity wave potential energy for different initial perturbations for the runs $D5^M_{512}$. The diamond indicates when the two waves merged into one. The dashed line gives the linear theory prediction.

4.7 Mixing

Next we focus on mixing. The primary quantities we are interested in are the amount of mass of the lower fluid that is mixed upwards and the distribution of this mixed mass. As discussed in section 4.4, in these simulations mixing on small scales is due to uncontrolled numerical diffusion; however, our investigation is based on the assumption that absent this effect, mass will still be mixed at a finite rate independent of the diffusivity because of the generation of eddies at smaller and smaller scales (turbulent diffusion). How close we are to this limit will be demonstrated in the next section, where we present our convergence studies. Furthermore since our results are from run-down numerical experiments, at late times, where turbulence has decayed, only numerical diffusion will give effective mixing. Therefore there are two expected stages of mixing: dynamic mixing at early times that is dominated by small scale

generation (cusp-breaking and overturning) and a diffusive stage at late times when turbulence is no longer present.

Keeping the above in mind, we quantify the mixing by measuring the lower fluid mass inside a mixed layer and averaging over the horizontal direction. The mixed layer is defined as the region in our computational domain where the concentration of the passive scalar X defined in equation 4.9 is between two extreme values $X_{\max}, X_{\min}$. We define therefore the quantity $M(t, X_{\min}, X_{\max})$ as the mixed mass per unit area located in the layer with $X_{\min} < X(t, x, y) < X_{\max}$:

$$M(t, X_{\min}, X_{\max}) = \frac{1}{l_x} \int_{\mathcal{D}} \rho X \, dx \, dy \tag{4.13}$$

where $\mathcal{D} = \{(x, y) | \, X_{\min} < X(t, x, y) < X_{\max}\}$. We further define the density distribution of the mass as

$$\mu(t, X) \equiv dM(t, X_{\min}, X)/dX \tag{4.14}$$

The distribution expresses the amount of mass from the lower fluid that lies between the values X and $X + dX$, per unit area, and is of particular interest when the effect of chemical or nuclear reactions is studied.

In figure 4.9 we plot $\mu(t, X)$ for the runs $A5^M_{1024}$, $B5^M_{1024}$, $C5^M_{1024}$, $D5^M_{1024}$, $E5^M_{1024}$. The distribution was calculated by averaging over space and time for the time range $1200 < tU/\delta < 1500$. The first three runs $A5^M_{1024}$, $B5^M_{1024}$, $C5^M_{1024}$ (overturning runs) have a large part of the mixed material lying in the range $0.02 < X < 0.4$ with a small shift of the peak of the distribution toward smaller values of X as G is increased. There is a striking difference between these runs and the results from $D5^M_{1024}$, $E5^M_{1024}$ (cusp-breaking runs). The peak of the distribution of the cusp-breaking runs are at smaller values ($X < 0.2$) with much smaller deviation (much narrower distribution

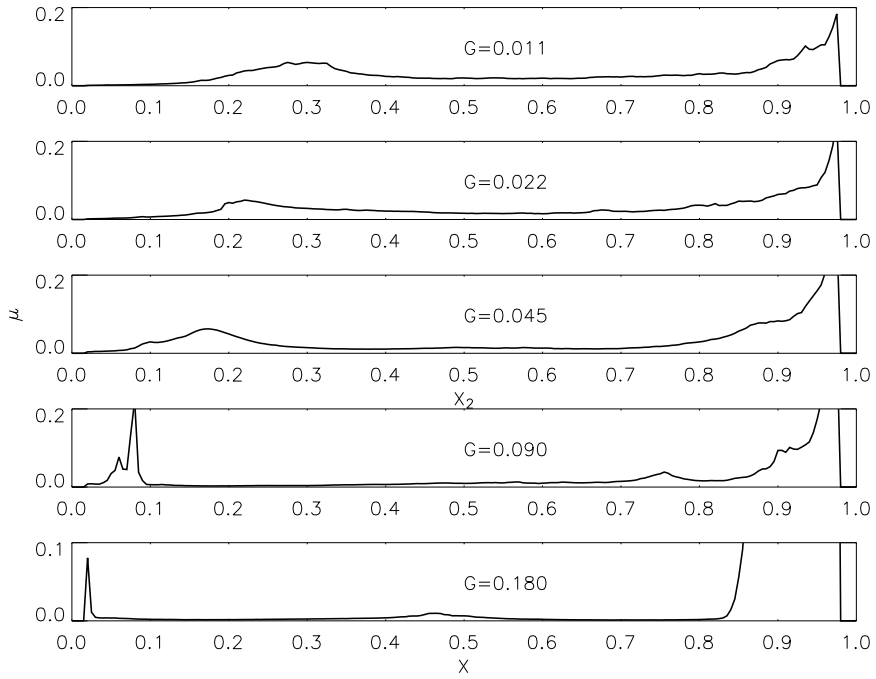

Figure 4.9: Distribution of mass μ in the mixed layer for the 1024^2 runs with $L = 1.80$ and different values of G; the value of G is increasing as we move from top to bottom.

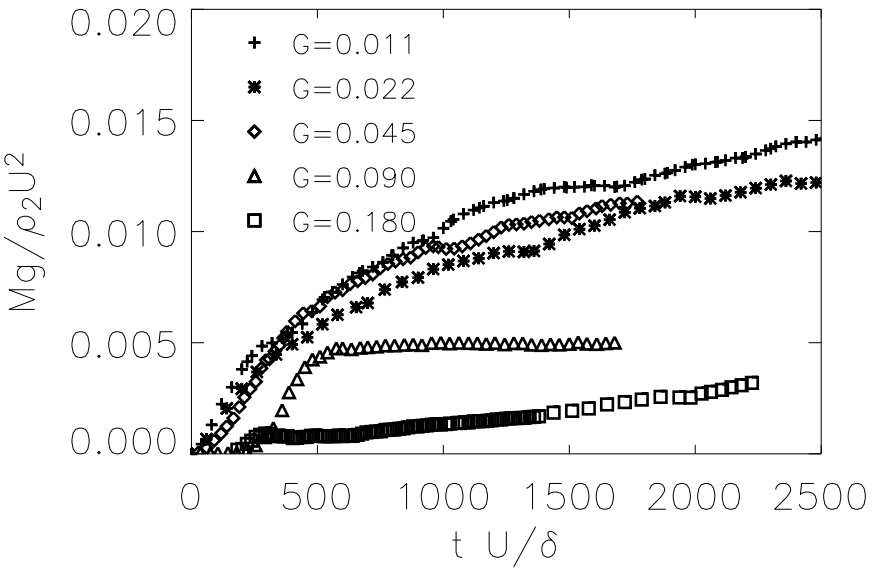

Figure 4.10: The evolution of the mass in the mixed layer per unit area M(t,0.02,0.4) with $L = 1.80$ and different values of G as indicated.

peaks). This implies that for the cusp-breaking mechanism the mixed mass is has spread over a larger area when compared to the overturning mechanism. Mixing by overturning is confined in the region of the wave, while the ejected material from the cusp-breaking can spread over a wider vertical range.

In all runs a significant amount of mass appears to be in the high X end of the distribution, this is more pronounced for the large G cases (e.g. E5). However, this mass is not related to the cusp formation or overturning but rather to numerical diffusion in the bulk of the wave. This phenomenon is more obvious in the large G runs only because the dynamical time scale (δ/U) is large and closer to the numerical diffusion time scale. This mixed mass strongly depends on the resolution, an effect that is not desirable. We are therefore only interested in the mixed mass for low X and we will therefore restrict our attention in estimating the mixed mass in the range ($0.02 \leq X \leq 0.4$).

Figure 4.10 shows $M(t, 0.02, 0.4)$ as a function of the rescaled time (tU/δ) from the

runs $A5^M_{1024}$, $B5^M_{1024}$, $C5^M_{1024}$, $D5^M_{1024}$ and $E5^M_{1024}$. The first three curves ($G \leq 0.045$) in which mixing is due to overturning, give similar results with small differences. The mixing time scale for those runs is determined by (δ/U). This implies that the mixed mass as a function of time for the given box size and small values of the parameter G, $(G \leq 0.045)$, is given by

$$M(t, 0.02, 0.4) = \rho_2 \frac{U^2}{g} f(tU/\delta) \tag{4.15}$$

where f is a function that can be estimated from figure 4.10. The total amount of mass mixed in the dynamic mixing range for sufficiently small δ is therefore to first order independent of the wind length scale δ; and only the time scale depends on δ. The amount of mixed mass increases linearly at early times (dynamical range), with a rate given by:

$$\frac{dM}{dt} = \alpha_1 \frac{\rho_2 U^3}{g\delta} \tag{4.16}$$

where α_1 is measured to be $\alpha_1 \simeq 1.5 \cdot 10^{-5}$.

The dynamical mixing appears to transition to a slower rate, that is possibly related to numerical mixing, after $t \simeq 2 \cdot 10^3 \delta/U$. The total amount of mass mixed at this point is

$$M = \alpha_2 \rho_2 U^2/g, \tag{4.17}$$

where α_2 is measured to be $\alpha_2 \simeq 1 \cdot 10^{-2}$.

As we move to higher values of the parameter G (runs $D5^M_{1024}$ and $E5^M_{1024}$) the above results no longer hold. The amount of mass mixed for the runs $D5^M_{1024}$ and $E5^M_{1024}$ deviates from the previously discussed curve: $M(t, 0.02, 0.4)$ appears to decrease fast with G when G is larger than 0.045. This is expected since we know from the linear theory that the growth rate decreases exponentially with G, and from

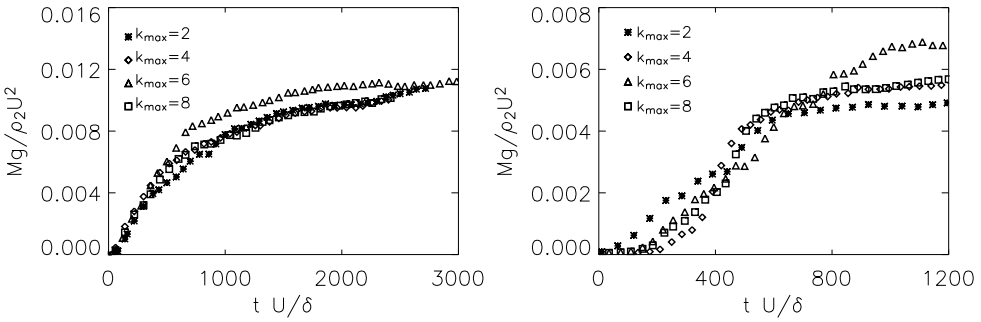

Figure 4.11: The amount of mass in the mixed layer $M(t, 0.02, 0.4)$ for different initial perturbations for the run $B5^M_{512}$ panel a) and for the ran $D5^M_{512}$ panel b).

weakly nonlinear theory we know that the wave to first order remains linear (e.g. no cusp) in the limit of large G.

In order to draw conclusions for the behavior of chaotic nonlinear systems from numerical simulations an ensemble average of different initial conditions is ideally required. However, the computational cost of high resolution runs does not allow for a large number of runs. For this reason, we have had to contend ourselves with four different simulations for the setups in $B5^M_{512}$ and $D5^M_{512}$ with different imposed perturbations, and we have obtained only qualitative results about the sensitivity of the runs to small differences in the initial conditions. The results are shown in figure 4.11(a-b). For the $B5^M_{512}$ runs fluctuations of M are small throughout the integrated time. For the runs $D5^M_{512}$ there are significant variations of the amount mixed. The chaotic behavior of the two vortex configuration, as discussed in the previous section, explains the existence of the large fluctuations. The sensitivity therefore of M to the initial imposed perturbation increases as we increase the parameter G, and one therefore should be careful when interpreting the results of a single run.

4.8 Convergence Studies

One of the key issues of the problem we examine is the mixing of the two species and it is therefore important to control diffusion. Unfortunately we have to rely on numerical diffusion, which is not a well-controlled quantity. It is believed that in the limit of high resolution (high effective Reynolds number), the effective diffusion of the two species is going to reach an asymptotic value independent of the resolution. This expectation is based on the belief that once fully developed turbulence appears effective diffusion would be determined by eddy diffusion. This assumption and how close to this limit our simulations are, needs to be explicitly tested.

To investigate the dependence of $M(t, X_{\min}, X_{\max})$ with resolution we repeated the same runs with different N and looked at the dependence of M and the μ on the grid size. A similar effect is observed for all the overturning runs. As we increase the resolution of each run the amount of mass mixed M decreases initially up to some point of lowest mixing and then starts increasing again. This is consistent with the idea that at low resolution, numerical diffusion dominates the mixing, and increasing the resolution decreases total mixing. Eventually, however, the mixing becomes dominated by mixing due to small scale motions, and increasing the resolution still further increases the total mixing as smaller and smaller eddies are resolved. Similar mixing behavior has been observed in simulations of Rayleigh Taylor instability [84, 85]. A more non-monotonic behavior was observed for the cusp-breaking waves as we increased resolution. In figure 4.12 we show the mixed mass $M(t, 0.02, 0.4)$ as a function of time for the runs $B5_N^M, D5_N^M$ for different values of N ranging from 64 to 1028. To further demonstrate the sensitivity of mixing with resolution for the large G runs we show, in figure 4.13 the results of the simulations $E5_N^M$ for different resolutions: the structure of the cusp changes drastically as we increase the resolution.

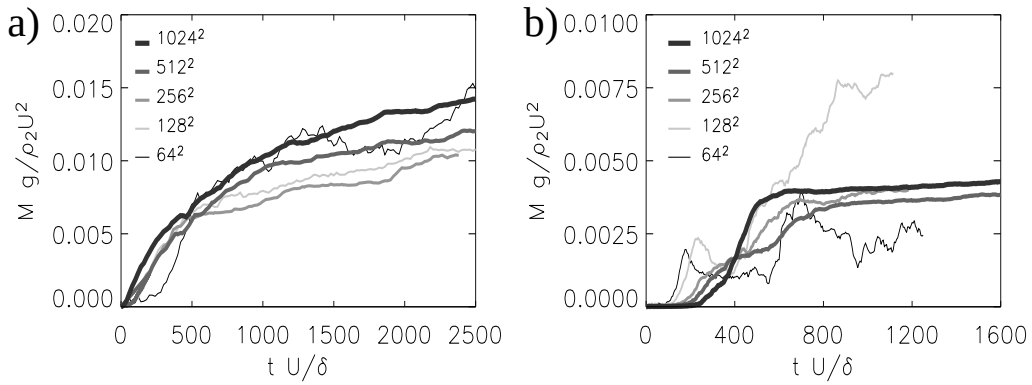

Figure 4.12: The evolution of the mixed mass $M(t, 0.02, 0.4)$ for the runs $B5_N^M$ (panel a) and $D5_N^M$ (panel b), for five different resolutions.

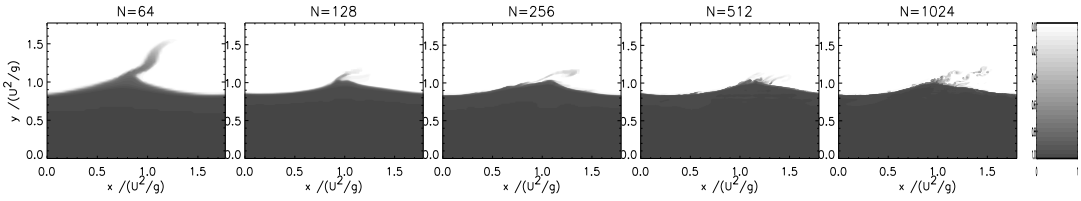

Figure 4.13: The formation of the cusp with different resolutions. N gives the number of grid points across the computational domain.

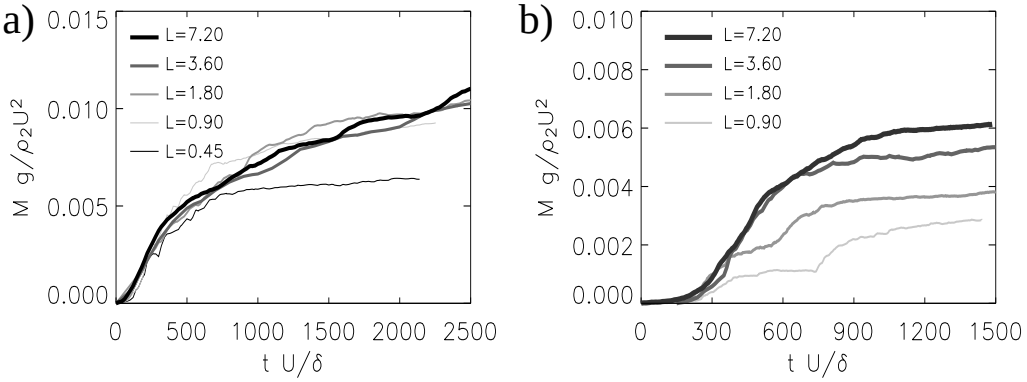

Figure 4.14: he evolution of the mixed mass $M(t, 0.02, 0.4)$ for the runs $B5_N^M$ (panel a) and $D5_N^M$ (panel b) and for five different box sizes L. The resolution per unit length (N/L) was kept fixed in all runs to 256/0.9.

Another limit we are interested in is $L \to \infty$. It is expected that if we chose sufficiently large L, then all horizontally averaged quantities should not depend on L. To test how close we are to this limit we performed a number of simulations changing the value of L while keeping the resolution per unit of physical length N/l fixed. It was found that larger values of L were required for convergence as we increased G. In figure 4.14 we present the dependence of $M(t, 0.02, 0.4)$ on the size of the computational domain L for two values of G, ($G = 0.0112$ and $G = 0.09$). Although the runs with small G converged for L as small as 0.9, for the large G modes convergence seems to be achieved only when L is larger than 7.2.

4.9 Summary of Numerical simulations

In this chapter, we have presented the results from an extensive investigation of wind-driven gravity waves, using numerical simulations. Motivated by an astrophysical problem we investigated how interfacial waves are amplified by the wind, following

[27] resonant mechanism, to the nonlinear (breaking wave) stage. Keeping the density ratio fixed at $r = 0.1$ we performed a parameter study by changing the nondimensional parameter $G = g\delta/U^2$.

Our results are in quantitative agreement with the linear theory and qualitative agreement with weakly nonlinear theory. In the nonlinear stage our results indicate that the initial exponential growth of the gravity waves predicted by Miles's theory is reaching saturation. For small values of G saturation occurs via overturning of the gravity waves. For larger values of G the waves saturate with out overturning. At the saturation amplitude secondary instabilities appear near the cusp of the wave, that result in cusp-breaking. These instabilities greatly resemble the instabilities of irrotational finite amplitude gravity waves [79]. Our results therefore demonstrate a connection between [27] theory for the generation of waves by wind and the theory for finite amplitude irrotational waves.

The transition between the formation of overturning waves (smaller values of G) and the formation of cusp-breaking waves (larger values of G) occurs close to the value of G at which the most unstable wavelength is also marginally KH unstable. We denote this critical value of G as G_T, and estimating from the linear theory we find $G_T \simeq 0.07$. The waves for the runs with $G < G_T$ (i.e. A, B, C) were found to overturn while the waves for the runs with $G > G_T$ (i.e. D, E) showed cusp-breaking. Although the transition from overturning to cusp-breaking waves in not necessarily sharp estimate from linear theory is expected to be a good indicator for the value of G that this transition takes place. Of course the validity of such result for different density ratios still needs to be examined.

The mixing properties of the two regimes (small G and large G) are significantly different. The overturning regime mixes very fast on a time scale δ/U, an amount of mass per unit area that scales as $\rho_2 U^2/g$. On the other hand, for large G mixing occurs

via secondary instabilities, smaller amount of mass is mixed and the distribution of the mass mixed is different.

Mixing was found to depend on the resolution for all cases, but more strongly in the cusp-breaking runs. It was found that at high enough resolutions, the amount of mass mixed increases with resolution. Our results on mixing can therefore be only interpreted only as a lower bound on the amount of mass mixed. We found better convergence in the limit $L \to \infty$ but higher L (computational domain) to achieve this was required as we increased the parameter G.

We believe that the results of this paper, can have a guiding role to future investigations on wind wave interactions and mixing in stratified media by wave breaking. In particular it would be interesting to know if cusp-breaking occurs for arbitrary large values of G or if there is a cut off; and how different density ratios, dimensionality and surface tension can affect these results. Finally, we emphasize that there is always a need to verify such results by comparing solutions obtained by different numerical methods as well as validate the calculations with experimental data.

CHAPTER 5

ASTROPHYSICAL IMPLICATIONS

5.1 Introduction

In this chapter we investigate the implications of the results obtained from the previous sections in the astrophysical problem, and try to construct a "sub-grid" mixing model to use in a one dimensional stellar evolution code.

So far we have only considered an idealized fluid dynamical problems for a limited range of parameters in order to get a basic physical understanding of shear mixing. The actual physical situation in the atmosphere of a white dwarf can be far more complex. For example, we have only considered small Mach number flows while the the relevant astrophysical flows can be from highly subsonic (convection winds) to highly supersonic at the beginning of the accretion phase. The density ratio (which we kept fixed in the previous chapter to the molecular ratio value $r = 0.1 \sim m_H/m_C$) can vary by a lot due to temperature differences and partial ionization. Further more we assumed an ideal equation of state and did not include any nuclear reactions that play a major part in this astrophysical problem. Extrapolating therefore our results to the white dwarfs atmosphere is not as straight forward.

An other difficulty that prevents us to make a direct connection of the previous results with the astrophysical problem is that our work only concentrated only in the shear layer over the boundary between the white dwarf and the atmosphere, and not in the large scale atmospheric flows that are responsible for the formation of this layer. Ideally, we would have to solve for the accretion phase and the resulting atmospheric instabilities like convection and "match" with the results from the boundary layer. However, a self-consistent calculation of the accretion boundary layer and the wind

profile in the atmosphere is far beyond the scope of the current research. The resolution needed to simulate the interaction is so fine as to prohibit the direct simulation of this effect within a macroscopically large (i.e., the entire atmosphere of the white dwarf) computational domain.

In order to deal with the above mentioned difficulties and get an estimate on the amount mixed we follow two steps. First we assume that most of the mixing takes place at the late stages of the accretion phase and second we use an one dimensional stellar evolution code (KEPLER) to model the large scale atmospheric flows that uses the results from the numerical simulations as a parameter input. In § 5.2 we present two-dimensional numerical simulations of the boundary layer with more (astrophysical) realistic initial conditions and demonstrate how the mixed mass depends on the velocity of the flow. We then, in § 5.3, incorporate this relation into a one-dimensional simulation and discuss two scenarios: that mixing only occurs if the convective zone reaches the C/O interface; and that the mixing occurs prior to the onset of convection. Because the shear in the envelope prior to the onset of convection is unknown, we compute the accretion and runaway for several different masses of the mixed layers. We discuss the implications, in § 5.4.

Because the shear in the envelope prior to the onset of convection is unknown, we compute the accretion and runaway for several different masses of the mixed layers.

5.2 Breaking Gravity Waves

To calculate the amount of mass mixed by wave breaking as a function of time, in more realistic situations, we repeated a suite of numerical simulations of wind-driven gravity waves. The initial configuration is similar to the one described in the previous chapter with two main differences. First the density ratio was fixed to $\rho_1/\rho_2 = 0.6$

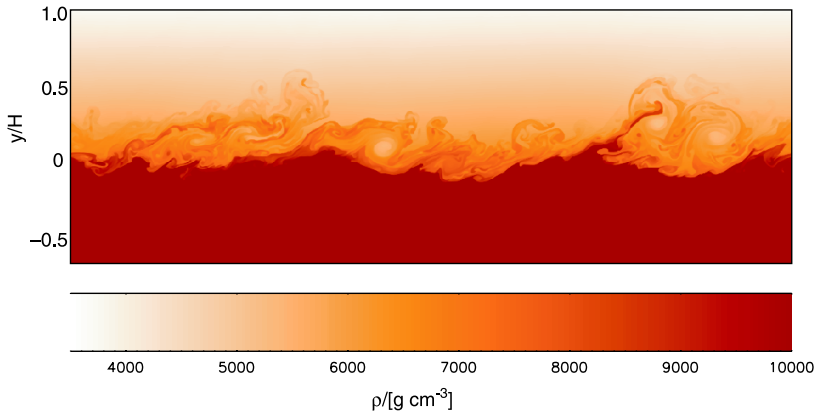

Figure 5.1: Breaking CO waves, as determined by simulations in two dimensions. Gravity points towards the bottom of the figure, with the vertical distance y in units of the pressure scale height H, as evaluated just above the interface. The color scale indicates the mass density in units of g cm $^{-3}$.

appropriate for the degenerate plasma prior to ignition. Furthermore we set the Mach number $\mathsf{Ma} = U_{\rm max}/c_{\rm s} = 0.5$ and consider four values of δ/H: 0.005, 0.01, 0.02, and 0.04. These values vary the value of $G = \delta g/U_{\rm max}^2)^{1/2} = (\delta/H)/(\gamma \mathsf{Ma}^2)$, that was investigated in the previous section. The unstable modes have wavenumbers [20] $k \geq g/U_{\rm max}^2(1-\rho_1/\rho_2)$. We chose the size of our computational domain to be roughly equal to this maximum wavelength, so that we have 1024 grid points along the largest possible wave. In practice, smaller waves become dominant, with the wavelength of the dominant mode depending on the wind profile. In all cases this dominant mode is well-resolved.

Figure 5.1 shows fully developed waves breaking, generation of the "spray", and mixing of the white dwarf substrate up into the atmosphere. Figure 5.2 shows contours (*black lines*) of the carbon mass fraction at 0.49, 0.20, and 0.02, respectively, for the simulation depicted in Figure 5.1, but at a later time, where 50% was the initial concentration of C in the lower fluid. The contour at 0.49 corresponds to the carbon

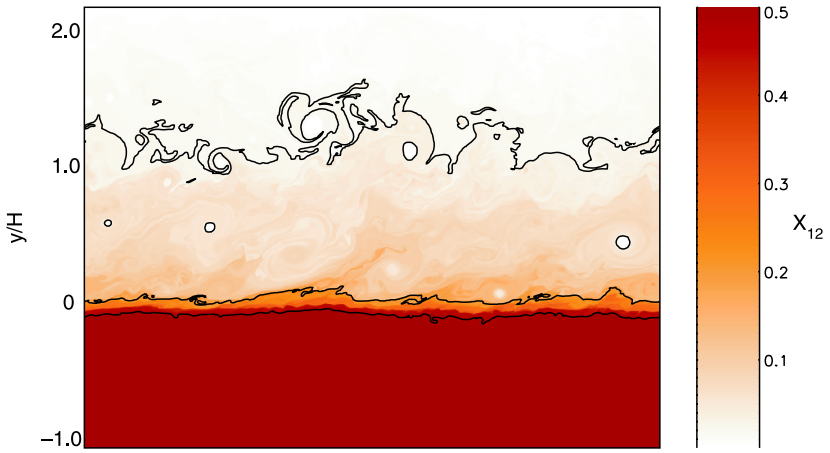

Figure 5.2: Mass fraction of ^{12}C for $\delta/H = 0.04$ after $t = 3500\delta/U$. The vertical dimension is scaled to the pressure scale height H as evaluated just above the interface. The contours for ^{12}C mass fractions of, from the top, 0.02, 0.20, and 0.49.

mass fraction of the underlying white dwarf, while the smaller contour values indicate how far outward into the accreted material the white dwarf substrate is mixed. The contour at 0.2 delimits the region that contains most of the initial enrichment.

Figure 5.3 shows the surface mass density (the mass of C/O in the mixed layer per unit area), $dM_{\rm CO}/dS$, averaged over the horizontal direction. The mixed layer is defined here as the region in which the carbon mass fraction is between 0.49 and 0.01. The amount of mixed mass depends on these delimiters; reducing the upper limit to 0.4 decreases the mixed mass by less than a factor of 2. The C/O is mixed rapidly until it saturates; further mixing occurs on diffusive timescales. Although the four curves in figure 5.3 do not the same behavior as the ones in figure 4.10 for small values of G (ie. there is a dependence of the initial slope on the value of G probably due to compresibility), the total mass of white dwarf material that becomes mixed at late times is independent of the lengthscale δ. The rate of mixing, i.e., the initial slopes of the curves in Figure 5.3, does show, however, some dependence on δ unlike

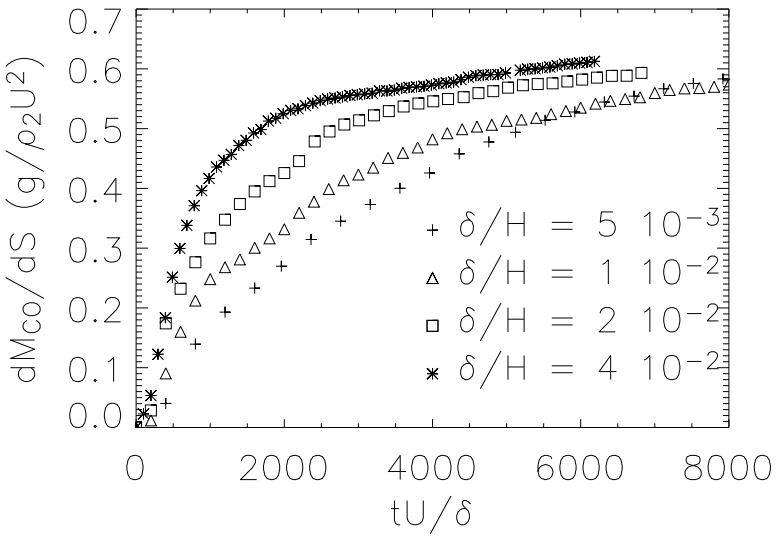

Figure 5.3: The mixed mass of C/O, per unit area, as a function of time. This was computed by averaging over the horizontal direction in the simulations. Time is scaled to $\delta/U_{\max}$ and $M_{\rm CO}$ is scaled to $\rho_2 U_{\max}^2/g$ (see eq. 5.1). Four different values of $g\delta/U_{\max}^2$ were used, 0.01, 0.02, 0.04, and 0.09.

what we found in the previous chapter. This is probably due to compressibility. Using dimensional analysis and the numerical results, we find that for a fixed density ratio $\rho_1/\rho_2 = 0.6$ the total mass per unit area, $dM_{\rm CO}/dS$, mixed into the accreted H/He saturates at

$$\frac{dM_{\rm CO}}{dS} = \alpha \frac{U_{\max}^2}{g} \rho_{\rm WD}, \tag{5.1}$$

where α is a non-dimensional constant[1] that we determine from the simulations to be $\alpha \simeq 0.6$ (see Figure 5.3). The timescale to reach saturation is far shorter than the timescale of either the accretion phase ($> 10^4$ yr) or the pre-peak convective phase (~ 100 yr) of a typical classical nova. For example, if $\delta/H = 0.01$ and $\mathsf{Ma} = 0.5$, then the saturation timescale is of order seconds for our nova setup.

1. In general, α depends on ρ_2/ρ_1 and possibly Ma. A parameter study, outside the scope of this paper, is necessary to determine this dependence.

5.3 One-Dimensional Nova Models

We now incorporate our simulations of the wave breaking and mixing into simulations of the thermonuclear burning of a nova. In order to explore the global properties of this local mixing mechanism, we compute several one-dimensional models of novae with a modified version of the KEPLER stellar evolution code [86] that includes a large network of $\sim$ 100 light isotopes [87] implicitly coupled into the stellar structure solver. This allows us to follow throughout the entire convective envelope the radioactive decays of nuclei that are formed at the base of the burning zone. The underlying white dwarf has a mass of $1.0\,M_{\odot}$, a radius of 5000km, a luminosity of $10^{31}\,\mathrm{ergs\,s^{-1}}$, and is composed of a 50%/50% ^{12}C/^{16}O mixture. We retain the outer $0.005\,M_{\odot}$ on the computational grid to follow the thermal inertia of the outer WD layers and allow the model to relax until it has a constant luminosity before we start the accretion. The accretion rate is $10^{-9}\,M_{\odot}\,\mathrm{yr^{-1}}$, and in all but one model (see item 3 below), the accreted material consists of 70 % ^{1}H, 28.7 % ^{4}He, 0.3 % ^{12}C, 0.1 % ^{14}N, and 0.9 % ^{16}O, by mass. Convection is modeled using the Ledoux criterion for stability and mixing length theory. We assume no convective overshooting and that semiconvection is too slow to cause mixing.

We investigate three scenarios, as summarized in Table 5.1, for generating the gravity wave induced mixed layer.

1. In the first scenario, the only shearing considered is that from the convective cells driving a wind at the interface between the H-rich atmosphere and the C/O substrate. This is the scenario envisaged by [18], in which the C/O, after being entrained, is then distributed throughout the convective zone. Figure 5.4 summarizes the evolution of the accreted layer. After accretion for about $6.9\times10^{4}\,\mathrm{yr}$ a convective zone forms about $2.5\times10^{-5}\,M_{\odot}$ above the WD interface. The to-

tal envelope mass accreted at ignition is $\approx 7 \times 10^{-5}\, M_\odot$, in good agreement with the estimates of [88, 89]. Within $\sim 100\,\mathrm{yr}$ from the onset of convection, the convective zone extends upward to the surface and downward to about $5 \times 10^{-6}\, M_\odot$ above the interface, at which time the runaway reaches its peak rate of energy generation. This peak phase evolves on a timescale of $\sim 1\,\mathrm{h}$, but the convection does not reach the WD interface. Only days later, when the nova envelope is already significantly expanding, does the burning layer reach the WD. This downward movement, in mass, of the burning layer is mediated by heat conduction into these deeper H-rich layers. The convective zone also moves deeper, but never quite reaches the WD interface[2]. As a result, there is no injection of C/O into the H-rich envelope, by construction.

The envelope expands to large radii ($> 10^{12}$ cm, large enough to engulf the secondary) by the end of the simulation, but the result will only be a slow nova, in rough agreement with the semi-analytical calculations of [88, 89]. We do not find any contact of the convective region with the WD substrate; as a result, we do not expect that any convection-driven wave mixing would occur, unless there is a large redistribution of angular momentum in the accreted envelope [12, 13].

2. In the second scenario, the shearing originates from a wind at the base of the accreted envelope blowing across the underlying C/O substrate. We assume that the wind persists throughout the H/He layer with velocity sufficient to drive mixing on a timescale much less than that to accreted a critical mass of

2. At the very bottom of the H shell the nuclear luminosity from H burning can never become large enough to drive convection, as it goes to zero at the interface; the only possibility for mixing to occur is if a steep temperature gradient arises from the thermal inertia of the heated WD core below an expanding H envelope.

fuel. In this case the mixed layer is generated prior to ignition. We also assume a linear (in Lagrangian mass coordinate) gradient in the mass fraction of C/O between the WD and the accreted envelope. Because the shear profile, and hence the amount of mass mixed, is unknown, we consider a range of mixed masses (see Table 5.1). Our ignorance of the fluid motions in the envelope and substrate prevents us from saying where and how the accreted material spreads over the surface, and so we cannot determine the actual shear at the base of the envelope. In all cases that we consider, the shear velocity is subsonic, which is the range of validity of the 2-d simulations. For such velocities, the mixed layer is always thinner than a pressure scale height (eq. [5.1]).

Figure 5.5 shows the case with the largest pre-enrichment: the mixed material comprises 4.6×10^{28} g (i.e., a total of 2.3×10^{28} g of WD material is being mixed with H-rich material). This is about 25% of the envelope mass, which is less than that generated by the calculation described in section 5.2. From equation (5.1), a 25% enrichment corresponds to $\mathsf{Ma} = 0.4$ if the velocity were uniform over the surface. We note that this velocity is much less than Keplerian, $U_{\rm max} \approx 0.05(GM/R)^{1/2}$, as expected in the envelope well below the accretion disk boundary layer [90]. If the velocity were not uniform over the surface, then a higher maximum velocity would be required to inject the same percentage of the total envelope mass.

The mixed layers are added to the surface using the same accretion rate as the rest of the envelope ($10^{-9}\, M_\odot\, {\rm yr}^{-1}$); to prevent a runaway while these layers are being added, we suspend nuclear energy generation during the accretion of the first 5×10^{28} g. About 50 yr prior to peak energy generation a semiconvective region forms in the outer 60 % (by mass) of the enriched layer; about 8 months

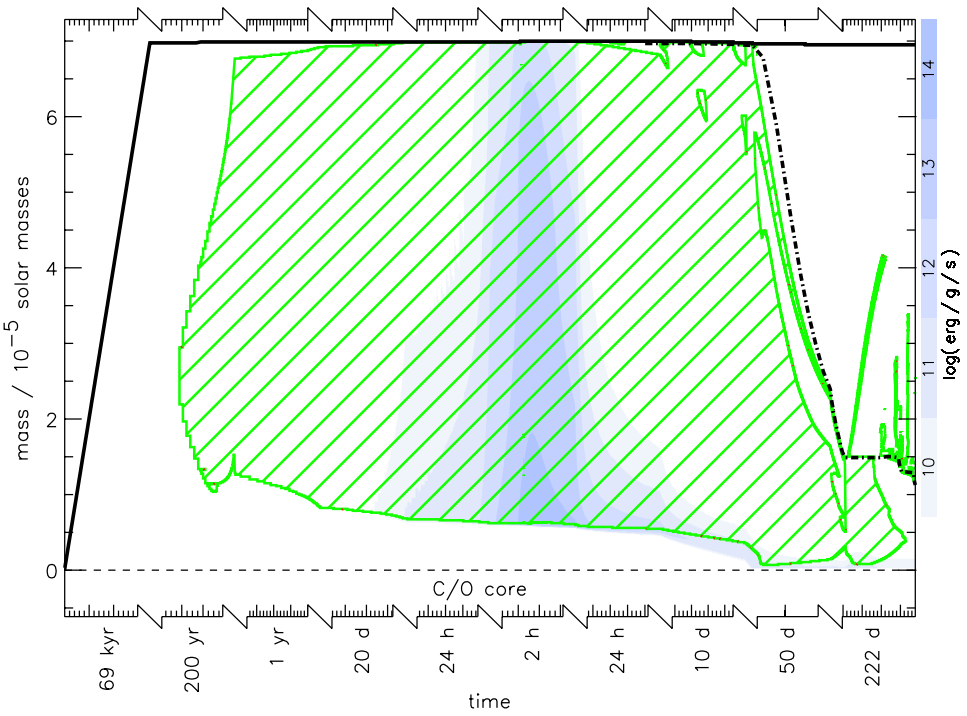

Figure 5.4: Kippenhahn diagram of a nova without enrichment. The x-axis indicates time intervals for the different evolution stages, and the y-axis gives the mass above the C/O WD substrate. *Green hatching* (framed by a *green line*) indicates convection, *blue shading* indicates nuclear energy generation for which each level of darker blue denotes an increase by one order of magnitude, starting at $10^{10}\,\mathrm{ergs\,g^{-1}\,s^{-1}}$. The *thick black line* shows the total mass of star (including ejecta), increasing because of accretion; the *dash-dotted line* indicates the mass outside of 10^{12} cm; and the *dashed line* marks the interface between the white dwarf C/O substrate and the accreted layers.

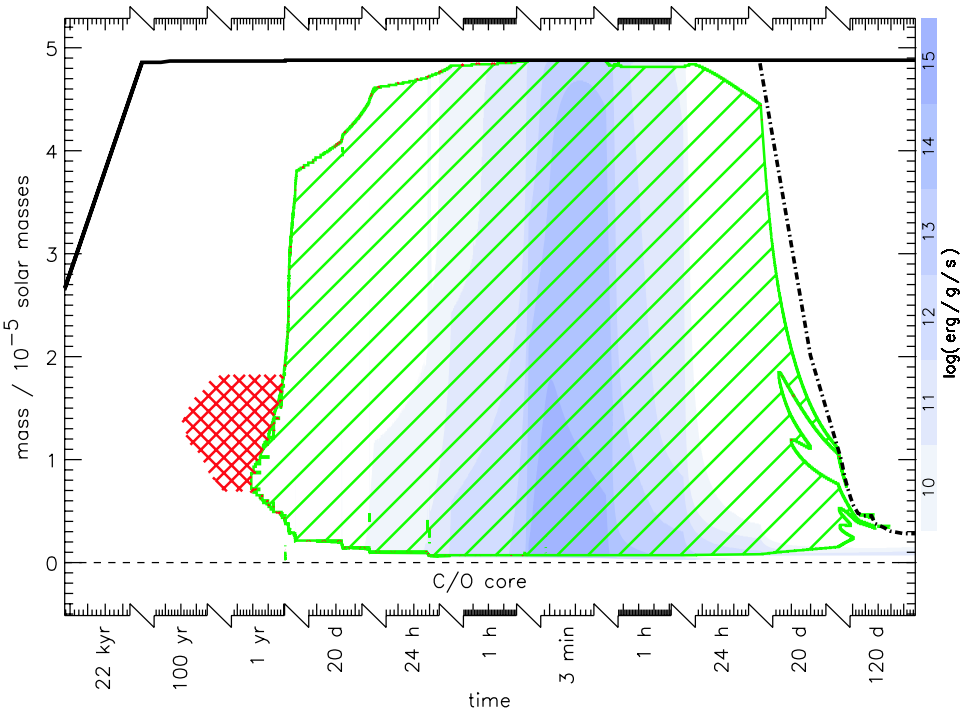

Figure 5.5: Same as Fig. 5.4 but for a model in which the inner $M_{\rm mix} = 4.6 \times 10^{28}$ g are enriched in C/O with a linear composition gradient (with respect to the Lagrangian mass coordinate) between the WD composition (C/O) at the base and the accretion composition (solar) at the upper edge. Note that the convective zone does not reach the interface with the WD substrate, and that a significant semi-convective region, indicated by *red hatching*, develops prior to the onset of convection.

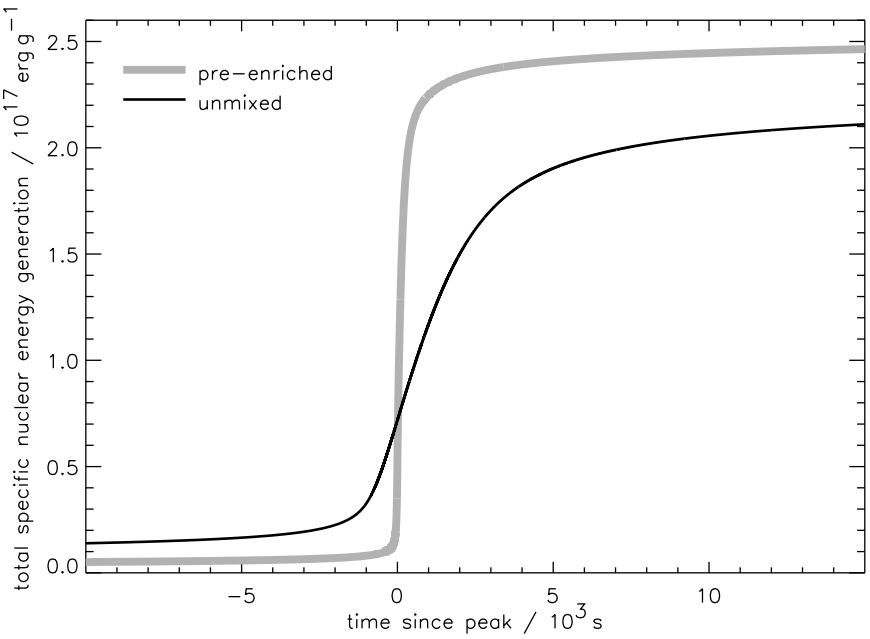

Figure 5.6: Time-integrated average specific nuclear energy generation of the accreted envelope. The curves are shifted so that the zero in time corresponds to the peak energy generation rate. The gray curve indicates the model with the highest wave-induced pre-enrichment (see Tab. 5.1 and Fig. 5.5); the black curve indicates the model without prior enrichment (Fig. 5.4). The slope of a curve is proportional to the average specific energy generation rate in the envelope.

before the peak a convection zone starts at the base of this semiconvective layer (at $7 \times 10^{-6}\,M_\odot$ above the WD interface) that extends upward to the surface and downward to about $5 \times 10^{-7}\,M_\odot$ above the interface. In contrast to the first case, the pre-mixed envelope with the largest enriched mass ignites at a smaller accumulated mass, $\approx 5 \times 10^{-5}\,M_\odot$.

The energy generation in the enriched layer is dominated by $^{12}\mathrm{C}(\mathrm{p},\gamma)^{13}\mathrm{N}(\beta^+)^{13}\mathrm{C}$. The peak energy generation timescale is about 3 min—20 times faster than in the first case—with a specific energy generation rate about 20 times higher. Figure 5.6 shows the specific nuclear energy generation in the accreted envelope, with the time centered about the peak energy generation rate. The larger

rate of energy generation roughly corresponds to the ~ 20 times greater metal enrichment. In this scenario the entire 25 % of pre-enriched C/O material is spread throughout the hydrogen envelope during the runaway. This leads to a a corresponding enrichment in the ejecta. The ejecta are unbound, i.e., they have a positive velocity at very large radii.

As in the first case, the convection never reaches the WD interface (although the base of the convective zone is much deeper), so there is no additional convection-induced wave mixing of the C/O substrate with the hydrogen-rich envelope. We did experiment with pre-runaway, pre-enriched layers as small as 1/10,000 the mass used in the case described above (Table 5.1). As before, we disregarded nuclear burning for the first 10^{28} g of accreted material, with the exception of the case with $3.77 \times 10^{-6}\, M_{\odot}$ of enrichment, where we took twice that mass to accommodate the entire enriched layer. The difference in masses for which nuclear burning is suspended is the reason for the case with the largest pre-enriched mass, $1.15 \times 10^{-5}\, M_{\odot}$ having a slightly larger envelope mass at runaway than that of the case with $3.77 \times 10^{-6}\, M_{\odot}$ of enriched mass.

In none of these cases did the convection reach the WD interface. Eventually, for the case of an enriched mass of $\leq 10^{-9}\, M_{\odot}$, the runaway behaves as in the non-enriched case: the energy release rate in the mixed layers is too small to drive convection above and heat conduction cools it efficiently so that the runaway does not occur in its vicinity. The slightly higher envelope masses obtained in the limit of small enrichment is likely to be an artifact of our suspension of nuclear energy generation for the first fraction of the accretion phase.

3. In a third scenario we assume accretion of material enriched to a mass fraction of 50 % in C/O. Allowing for nuclear energy generation instantaneously in this

material leads to a rapid runaway after only a thin layer has been accumulated at the surface of the star. If this magnitude of enrichment was due to instantaneous mixing with a colder WD substrate, then a lower temperature in the enriched material and thus a significantly later runaway could result. We include this run to demonstrate how qualitatively different the accretion of pre-enriched material behaves as compared to first accreting unenriched material and then, only later after it has settled, mixing the accreted layers with the C/O substrate.

5.4 Implications and Summary

Using a constant wind profile that blows across the surface of a white dwarf, we have performed a two-dimensional parameter study of the mechanism proposed by [18]. Our primary results of the mixing rate and the maximum mixed mass, equation (5.1), suggest that this process can mix about 10^{-6}–$10^{-5}\,M_{\odot}$ of the underlying C/O into the hydrogen-rich envelope. From this, we investigated two scenarios: that the wind is the result of convection, and that the wind originates during the accretion phase.

We find that if no enrichment occurs prior to the onset of convection, then the convective zone does not reach the C/O interface, and no additional mixing occurs (in the one-dimensional model) in the absence of convective overshoot. The result in this case will be a slow nova, with little enrichment of the ejecta. In contrast, an envelope with a mixed layer at the C/O interface, consistent with the scalings from high-resolution numerical studies, provides a more violent runaway and the ejecta are enriched by $\sim 25\%$ in C/O, consistent the enrichment observed in some nova ejecta. Such an event does require a strong shear velocity, but the saturation amount of mass mixed is roughly independent of the shape of the shear profile, so long as its thickness is much less than a pressure scale height. Our runs, outlined in Table 5.1, show that

when the metals are concentrated at the base of the accreted envelope, the amount of mass accreted prior to runaway is *larger* than if the C/O were uniformly distributed over the envelope, i.e., if the white dwarf were to accrete material with a supersolar metallicity. The reason is that the opacity of the envelope is larger than when the C/O are concentrated at the base.

There are a number of issues that we have not yet addressed or investigated. First, our results might depend on the dimensionality of the system. We would therefore expect that although the generation of the gravity waves is captured by two-dimensional dynamics, the energy cascade of the waves and the advection of spray and vorticity will be different in a three dimensions. Second, this work investigates only the density ratio for an accreted envelope in thermal equilibrium. During the early phase of accretion and during the runaway the density ratio will likely be different. Third, although our parameter study covers more than one order of magnitude in δ, it is important to know if our results still hold at even larger values. As δ becomes a respectable fraction of H, we expect that the stratification of the envelope, and in particular the effect of a non-zero Brunt-Väisälä frequency, will become important. All of these differences can affect the mass and thickness of the mixed layer, and the investigation of these issues is the subject of ongoing work.

In our one-dimensional nova simulations, we assumed that a convective roll will only entrain the mixed layer if the base of the convective zone (as computed from a mixing-length formalism) reaches the interface. Future multidimensional studies can inform us as to how convection interacts with the interfacial gravity waves, and to whether this assumption is in fact correct. Moreover, our sub-grid model, when incorporated into a one-dimensional calculation, does not account for spatial variations of the wind. Such a variation would occur, for example, if the fuel accretes non-uniformly over the surface of the star and then spreads. In reality the amount of

Table 5.1: Properties of the 1D nova models

Case	$M_{\rm enrich}$ ($M_\odot$)	$M_{\rm envel}$ ($M_\odot$)	$\dot{E}_{\rm nuc,max}$ (ergs s^{-1})
no pre-enrichment	0	6.93×10^{-5}	6.68×10^{42}
wave pre-enrichment	1.26×10^{-9}	7.08×10^{-5}	7.24×10^{42}
wave pre-enrichment	1.26×10^{-8}	7.05×10^{-5}	7.65×10^{42}
wave pre-enrichment	1.26×10^{-7}	6.78×10^{-5}	7.71×10^{42}
wave pre-enrichment	1.31×10^{-6}	5.42×10^{-5}	1.27×10^{43}
wave pre-enrichment	3.77×10^{-6}	4.67×10^{-5}	2.68×10^{43}
wave pre-enrichment	1.16×10^{-5}	4.85×10^{-5}	1.26×10^{44}
enriched accretion	(50 %)	2.08×10^{-6}	5.28×10^{40}

mass mixed will vary over the surface of the star. Our one-dimensional calculations must of necessity take the mixed mass as a free parameter. Because the amount of C/O entrained depends quadratically on the velocity in the wind profile, our calculation underscores the need for detailed simulations of the shear profile of an accreting white dwarf. These issues are clearly important and are the next steps to pursue.

APPENDIX A

DETAILED DERIVATIONS OF FORMULAS

A.1 Extension of Howard's semicircle theorem

We begin from

$$\phi_{yy} - \Big(K^2 + \frac{V_{yy}}{V-C}\Big)\phi = 0, \quad \phi|_{y=0} = 1, \quad \phi|_{y=\infty} = 0 \tag{A.1}$$

and

$$KC^2\phi - r\Big[(V_0 - C)^2\phi_y - (V_0 - C)V_y\phi\Big] - \tilde{G}\phi = 0. \tag{A.2}$$

where $\tilde{G}$ is the restoring force ($\tilde{G} = G(1-r)$ for the simplest case), $0 < \tilde{G}$, $0 < K$, and we assume $C_i \neq 0$. Let $V_G = V - C$, and let $\psi = \phi/V_G$ and $D \equiv \partial_y$. Note that

$$V_G^2 D\phi - V_G\phi DV_G = V_G^3 D\psi \ .$$

The boundary condition can then be written as

$$rV_G^3 D\psi = KC^2 - \tilde{G} \ . \tag{A.3}$$

From (A1) we obtain

$$V_G D^2\psi + 2DV_G D\psi - V_G K^2\psi = 0 \ ; \tag{A.4}$$

multiplying the last relation with $V_G\psi^*$ and integrating, we obtain:

$$\psi^* V_G^2 D^2\psi + \psi^* DV_G^2 D\psi - V_G^2 K^2|\psi|^2 = 0 \ ,$$

so that

$$D[\psi V_G^2 D\psi] - V_G^2 |D\psi|^2 - V_G^2 K^2 |\psi|^2 = 0$$

and

$$-[\psi^* V_G^2 D\psi]_0 - \int_0^\infty V_G^2 [|D\psi| + K^2 |\psi|^2] dy = 0 \ ;$$

using the normalization condition, and denoting by $Q(y) = [|D\psi| + K^2|\psi|^2] \geq 0$, we then have

$$\frac{1}{V_G^*} V_G^2 \frac{KC^2 - \tilde{G}}{V_G^3} = -r \int_0^\infty (V_G)^2 Q dy \ ,$$

so that

$$\frac{KC^2 - \tilde{G}}{|V_G|^2} = -r \int_0^\infty (V - C)^2 Q dy \ . \tag{A.5}$$

Taking the imaginary part, we obtain

$$\frac{K(2C_r C_i)}{|V_G|^2} = r \int_0^\infty 2C_i (V - C_r) Q dy$$

$$\frac{KC_r}{|V_G|^2} = r \int_0^\infty (V - C_r) Q dy \ . \tag{A.6}$$

Therefore,

$$0 < C_r < V_{max} \tag{A.7}$$

i.e., a wind cannot generate waves traveling faster than its maximum speed. Now, taking the real part, we obtain

$$\frac{K(C_r^2 - C_i^2) - \tilde{G}}{|V_G|^2} = -r \int_0^\infty [V^2 - 2VC_r + C_r^2 - C_i^2] Q dy \ , \tag{A.8}$$

or

$$\frac{K(C_r^2 - C_i^2) - \tilde{G}}{|V_G|^2} = -r\left[\int_0^\infty V^2 Q dy - 2C_r \int_0^\infty V Q dy + (C_r^2 - C_i^2)\int_0^\infty Q dy\right] ,$$

or

$$\frac{K(C_r^2 - C_i^2) - \tilde{G}}{|V_G|^2} = -r\left[\int_0^\infty V^2 Q dy - 2C_r\left\{\frac{KC_r}{r|V_G|^2} + C_r\int_0^\infty Q dy\right\} + (C_r^2 - C_i^2)\int_0^\infty Q dy\right] ,$$

so that

$$0 < \frac{K|C|^2 + \tilde{G}}{|V_G|^2} = r\int_0^\infty [V^2 - |C|^2] Q dy \tag{A.9}$$

and

$$C_r^2 + C_i^2 < V_{max}^2 , \tag{A.10}$$

which is the sought-for result.

A.2 lower bound on the CL-unstable modes

Consider the wind profile $V = 1 - e^{-y}$; then the equations 2.21 and 2.21 become

$$\phi_{yy} - \left(K^2 - \frac{e^{-x}}{1 - e^{-x} - C}\right)\phi = 0 \tag{A.11}$$

and

$$C^2 - r[C^2\phi_y + C] - G(1 - r) = 0. \tag{A.12}$$

We are interested in the value of K for which our system becomes marginaly unstable. From the extension of Howard's semicircle theorem to our case we know that for C_r greater than V_{max} the system is stable, so the instability is expected to start when $C = V_{max} = 1$. Using this value for C we obtain from A.11

$$\phi_{yy} - \left(K^2 + 1\right)\phi = 0 \; ; \tag{A.13}$$

therefore $\phi = e^{-y\sqrt{K^2+1}}$ and from A.12 we then have

$$K - r[-\sqrt{K^2+1} + 1] - G(1-r) = 0 \; , \tag{A.14}$$

which by solving gives us

$$K_{min} = \frac{G(1-r) + r - r\sqrt{(G(1-r)+r)^2 + (1-r^2)}}{1-r^2} \; . \tag{A.15}$$

Numerical integration confirms this result.

A.3 Large G behavior

We are interested in cases for which the factor G is large. As already discussed, such cases not only correspond to the astrophysical limit of strong surface stratification, but also correspond to cases for which the wind is weak enough so that the growth rate of (linearly) unstable modes is small, i.e., to cases for which our analysis is actually appropriate.

In order to proceed, we need to adopt a specific wind profile; in what follows, we will use a profile of the form $U = (1 - e^{-y})$. However, we note that our basic results hold for more general wind profiles. From equation 2.28 we know that the unstable modes will have K to be of the same order as G, and therefore $K \gg 1$; this allows us to write a WKBJ expansion for the solution of the perturbation stream function of equation (2.36) for the wind. The equation we have to solve for large K is therefore

$$\phi_{,yy} - \left[K^2 + \frac{U_{,yy}}{U-C}\right]\phi = 0\,; \tag{A.16}$$

The boundary condition at the interface is:

$$KC^2 - r[C^2\phi_y|_0 - CU'|_0] - G(1-r) = 0\,. \tag{A.17}$$

The WKBJ approximation will break down at two points: The first one is at $y = y_c$, where the critical layer is located; the second one is at $y = y_a$, where y_a is the solution of $K^2(U-C) + U_{,yy} = 0$ and the second term in (A.16) becomes zero. For this reason, we will have to decompose the $y-$axis into three regions: I. $0 < y < y_c$; II. $y_c < y < y_a$; III. $y_a < y$. The first-order solutions of the WKBJ equations therefore are:

$$\text{(I)} \qquad \phi = A_1\frac{1}{\sqrt{w}}e^{-\int_0^y w dy'} + B_1\frac{1}{\sqrt{w}}e^{+\int_0^y w dy'}\,, \tag{A.18}$$

$$\text{(II)} \qquad \phi = A_2\frac{1}{\sqrt{w}}\sin\left(\int_{y_c}^y w dy' - \pi/4\right) + B_2\frac{1}{\sqrt{w}}\cos\left(\int_{y_c}^y w dy' - \pi/4\right)\,, \tag{A.19}$$

$$\text{(III)} \qquad \phi = A_3\frac{1}{\sqrt{w}}e^{-\int_{y_a}^y w dy'}\,, \tag{A.20}$$

where

$$w(y) = \sqrt{\left|K^2 + \frac{U_{,yy}}{U-C}\right|} = \sqrt{\left|K^2 - \frac{e^{-y}}{1-C-e^{-y}}\right|}\,, \tag{A.21}$$

and the $-\pi/4$ factor appearing in the solution for Region II is inserted for convenience, to be exploited shortly. The coefficients A_1, B_1, A_2, B_2, A_3 are connected through the solutions at the points where the WKBJ approximation breaks down, and can be obtained using matched asymptotics. Thus, close to $y = y_a$ it is well-known that the solution is an Airy function [91]. Matching the two solutions we obtain that for

$y_c < y < y_a$,

$$\phi = \frac{2A_3}{\sqrt{w}} \left\{ \sin[I_1] \cos\left[\int_{y_c}^{y} w dy' - \pi/4 \right] - \cos[I_1] \sin\left[\int_{y_c}^{y} w dy' - \pi/4 \right] \right\} , \quad \text{(A.22)}$$

and therefore

$$B_2 = 2A_3 \sin[I_1] , \qquad A_2 = -2A_3 \cos[I_1] , \quad \text{(A.23)}$$

where $I_1 = \int_{y_c}^{y_a} w dy'$. The solutions near the critical point $y = y_c$ satisfy the equation

$$\phi_{,yy} - \frac{U_c''}{U_c' y} \phi = 0 \quad \text{(A.24)}$$

where $U_c'' = U''|_{y=y_c}$ and $U_c' = U'|_{y=y_c}$. The solutions of the above equations are given in terms of $z = -(y - y_c) U_c''/U_c' > 0$ by

$$f_1(z) = \sqrt{z} J_1\left(2\sqrt{z}\right) , \qquad f_2(z) = \sqrt{z} N_1\left(2\sqrt{z}\right) , \quad \text{(A.25)}$$

where J_1, N_1 are, respectively, the first Bessel and Neumann (Bessel of the second kind) functions. The first terms in the asymptotic expansion for $y \to +\infty$ are

$$f_1(z) \simeq \frac{\sqrt[4]{z}}{\sqrt{\pi}} \sin\left(2z^{1/2} - \pi/4\right) , \qquad f_2(z) \simeq -\frac{\sqrt[4]{z}}{\sqrt{\pi}} \cos\left(2z^{1/2} - \pi/4\right) . \quad \text{(A.26)}$$

Matching with the outer solution, we have

$$\phi = \sqrt{\pi} A_2 f_1(z) - \sqrt{\pi} B_2 f_2(z) .$$

The asymptotic expansion for $z \to 0^+$ is

$$f_1 \simeq z + \ldots \tag{A.27}$$

$$\pi f_2 \simeq -1 + z \ln|z| + \ldots - (1-2\gamma)z + \ldots , \tag{A.28}$$

where γ is the Euler-Masceroni constant. Thus, we can identify f_1 with the regular Frobenius solution ϕ_a, and f_2 with the singular Frobenius solution ϕ_b. Here we assumed that C_i is much smaller that G^{-1} (this is something that will be justified a posteriori).

For $y < y_c$ the solutions of equation (A.24) can be obtained by making the transformation $z \to e^{-i\pi} z$ which is equivalent to taking the contour below the critical layer. By doing this the first Bessel function transforms to the first modified Bessel function that is growing exponentially and is real while the second one transforms to a linear combination of an exponentially growing and an exponentially decreasing modified Bessel function, and due to the presence of the logarithm it is going to have an imaginary part. Their asymptotic expansion for $y \to \infty$ is

$$f_1 \simeq -\frac{\sqrt[4]{z}}{2\sqrt{\pi}} e^{+2\sqrt{z}}, \qquad f_2 \simeq \frac{\sqrt[4]{z}}{2\sqrt{\pi}} \left[i e^{2\sqrt{z}} - 2e^{-2\sqrt{z}} \right], \tag{A.29}$$

with $z = (y - y_c)U_c''/U_c' > 0$. The inner solution for negative large z can be then written as

$$\phi_{in} \simeq \sqrt{\pi}\left(A_2 f_1 - B_2 f_2\right) , \tag{A.30}$$

$$\simeq -\frac{\sqrt[4]{z}}{2}\left[\left(A_2 + iB_2\right) e^{2\sqrt{z}} - 2B_2 e^{-2\sqrt{z}} \right] . \tag{A.31}$$

Matching with the outer solution then gives

$$\phi \simeq \frac{1}{2\sqrt{w}}\left[-(A_2+iB_2)e^{-\int_{y_c}^{y} w dy'} + 2B_2 e^{+\int_{y_c}^{y} w dy'}\right] \tag{A.32}$$

or

$$\phi = -\frac{A_2+iB_2}{2} e^{I_2}\frac{1}{\sqrt{w}} e^{-\int_0^y w dy'} + B_2 e^{-I_2}\frac{1}{\sqrt{w}} e^{\int_0^y w dy'}, \tag{A.33}$$

where $I_2 = \int_0^{y_c} w dy'$. Gathering all the terms then gives

$$A_1 = A_3\Big(\cos[I_1] - i\sin[I_1]\Big)e^{+I_2}, \qquad B_1 = 2A_3 \sin[I_1]\, e^{-I_2}, \tag{A.34}$$

and

$$\phi = A_3\left[2\sin(I_1)e^{-I_2}e^{+\int_0^y w dy'} + \cos(I_1)e^{+I_2}e^{-\int_0^y w dy'} - i\sin(I_1)e^{+I_2}e^{+\int_0^y w dy'}\right]. \tag{A.35}$$

The values of ϕ and $\phi_{,y}$ at zero are therefore

$$\phi|_0 = A_3\left[2\sin(I_1)e^{-I_2} + \cos(I_1)e^{+I_2} - i\sin(I_1)e^{+I_2}\right], \tag{A.36}$$

$$\phi_{,y}|_0 = A_3\left[2\sin(I_1)e^{-I_2} - \cos(I_1)e^{+I_2} + i\sin(I_1)e^{+I_2}\right], \tag{A.37}$$

where we have kept terms only to first order in K. For the given wind profile $(1-e^{-x})$, we have:

$$y_c = -K\ln(1-C), \qquad y_a = -[K\ln(1-C) - K\ln(1+1/K^2),$$

$$I_1 \simeq \frac{\pi}{2K} + \mathcal{O}(1/K^3), \tag{A.38}$$

$$I_2 \simeq K y_c + O(1/K^2) = -K\ln(1-C) + \mathcal{O}(1/K), \tag{A.39}$$

$$\sin(I_1) \simeq \frac{\pi}{2K}, \qquad \cos(I_1) \simeq 1, \quad e^{-I_2} = (1-C)^K.$$

Normalizing so that $\phi|_0 = 1$, we then obtain

$$\phi_{,y} = \frac{2\sin(I_1)e^{-I_2} - \cos(I_1)e^{+I_2} + i\sin(I_1)e^{+I_2}}{2\sin(I_1)e^{-I_2} + \cos(I_1)e^{+I_2} - i\sin(I_1)e^{+I_2}}\,, \tag{A.40}$$

or

$$\phi_{,y} = -1 + \frac{4\sin(I_1)e^{-I_2}}{2\sin(I_1)e^{-I_2} + \cos(I_1)e^{+I_2} - i\sin(I_1)e^{+I_2}}\,. \tag{A.41}$$

The second term in equation (A.41) is exponentially small when compared to 1 since $I_2 \sim K$; neglecting this term when appropriate then allows $\phi_{,y}$ to be written as

$$\phi_{,y} = -1 + 4i\sin^2(I_1)e^{-2I_2}\,, \tag{A.42}$$

where we have kept only the first term in the expansion of the real and imaginary parts. Plugging in this value of $\phi_{,y}$ in equation (A.17), we obtain, to zeroth order,

$$C_0 = \sqrt{\frac{1-r}{1+r}\frac{G}{K}} = \sqrt{\mathcal{A}_t G/K}\,, \tag{A.43}$$

which corresponds to the gravity wave in the absence of a wind; $\mathcal{A}_t$ is the Atwood number. For our purposes, this is as far as we need to go in analyzing the real part of C.

We next turn to analyzing the imaginary part of C. To obtain the first order in $\mathrm{Im}\{C\} = C_i \ll C_0$ we have:

$$2K(1+r)C_0C_i - rKC_0^2(1+\phi_{,y}) = 0, \qquad C_i = \frac{1}{2}\frac{r}{1+r}C_0(1+\phi_{,y}), \tag{A.44}$$

so that

$$C_i = \frac{2rC_0}{1-r}\sin^2(I_1)e^{-2I_2}, \qquad \text{or} \tag{A.45}$$

$$\mathrm{Im}\{C_1\} = \frac{r\pi^2}{2(1+r)}\frac{1}{\mathcal{A}_t^2 G^2}\left(\frac{\mathcal{A}_t G}{K}\right)^{5/2}\left[\left(1-\frac{1}{\sqrt{K/(\mathcal{A}_t G)}}\right)^{(K/\mathcal{A}_t G)}\right]^{2\mathcal{A}_t G}. \tag{A.46}$$

We note that $(1-1/\sqrt{x})^{2x}$ is a bounded function smaller than one with $q_m = \max(\ln(1-1/\sqrt{x})^{2x}) \simeq -2.45\ldots$, and therefore C_i has a negative exponential dependence on G and the result in 2.34 follows. We note further that this exponential dependence should be independent of the wind profile, and in a more general case — for which $U(y)$ is the wind profile and $U^{-1}(c)$ is its inverse — the growth rate will be proportional to $C_i \sim \exp[-2KU^{-1}(c)]$; this can be re-written as $C_i \sim f(c(K))^{\mathcal{A}_t G}$, with $f(c) \equiv \exp[-2U^{-1}(C)/C]$ a bounded function and $C = C_0$. The interpretation of equation (A.45) is straightforward: it simply states that the growth rate is proportional to the negative exponential of the height of the critical layer, as measured in units of the wavelength.

A.4 Rescaling (3.38-3.41)

Before we begin investigating the amplitude equations we re-scale our system so that we are left with a minimum number of free parameters. By letting $Z = U''/\sqrt{U'}\tilde{Z}$, $Y = \eta/\sqrt{U'}$, $T = \tau/(\sqrt{U'}k)$, $\xi = Kx$ and $\nu = \nu'/\sqrt{U'}$ we obtain the following equation to be solved:

$$\tilde{Z}_{,\tau} + \eta\tilde{Z}_{,\xi} - \tilde{\Psi}_{0,\xi}\tilde{Z}_{,\eta} - \nu'\tilde{Z}_{,\eta\eta} = \tilde{\Psi}_{0,\xi}\,,$$

with

$$J = \frac{1}{2\pi} \int_{-\pi}^{+\pi} \int_{-\infty}^{+\infty} e^{-i\xi} \tilde{Z} d\eta d\xi \,.$$

By rescaling A to $|\mathcal{C}_2|^2/|\mathcal{D}_1|^2 A$, and H to $|\mathcal{C}_2|^2/|\mathcal{D}_1| H$, we can always scale our system so that $\mathcal{D}_1 = 1$ and $\mathcal{C}_2 = -1$. Finally, the coefficient $\mathcal{C}_1$ can always be set to zero by performing a Galilean transformation ($\tau \to \tau + \mathcal{C}_1 \xi$) and shifting the critical layer by $Y \to Y - \mathcal{C}_1$. The last transformation corrects the position of the critical layer to order ϵ. We are left therefore with two independent parameters, $\mathcal{D}_2$ and ν, to investigate. The parameter $\mathcal{D}_2$ gives a measure of the coupling of the critical layer to the wave; ($\mathcal{D}_2 = 0$ gives the evolution of a "free" critical layer uncoupled from gravity waves).

REFERENCES

[1] Gehrz, R. D., Truran, J.W., Williams, R.E., & Starrfield, S. 1998, "*Nucleosynthesis in classical novae and its contribution to the interstellar medium*", PASP, **110**, 3

[2] Livio, M. & Truran, J.W. 1994, "*On the interpretation and implications of Nova abundances– an abundance of riches or an overabundance of enrichments*", Astrophys. J., **425**, 797

[3] Truran, J. W. 1982,"*Essays in Nuclear Astrophysics*, ed. C. A. Barnes, D. D. Clayton, & D. N. Schramm (Cambridge: Cambridge University Press), 467

[4] Starrfield, S.G., Truran, J.W., Sparks, W.M., & Kutter, G.S. 1972, "*CNO abundances and hydrodynamic models of Nova outbursts*", Astrophys. J., **176**, 169

[5] Hernanz, M., José, J., Coc, A., & Isern, J. 1996, "*On the synthesis of Li-7 and Be-7 in novae*", Astrophys. J., **465**, L27

[6] Starrfield, S.G., Truran, J.W., Wiescher, M.C., & Sparks, W.M. 1998, "*Evolutionary sequences for Nova V1974 Cygni using new nuclear reaction rates and opacities*" MNRAS, **296**, 502

[7] Prialnik, D. & Kovetz, A. 1984, "*The effect of diffusion on prenova evolution – CNO-enriched envelopes*" Astrophys. J., **281**, 367

[8] Kovetz, A. & Prialnik, D. 1985, "*CNO abundances resulting from diffusion in accreting nova progenitors*", Astrophys. J., **291**, 812

[9] Kippenhahn, R. & Thomas, H.-C. 1978, "*Accretion belts on White-Dwarfs*" Astronomy & Astrophys., **63**, 625

[10] MacDonald, J. 1983, "*Mixing by shear instabilities in differentially rotating inhomogeneous stars with application to accreting white dwarf models for novae*", Astrophys. J., **273**, 289

[11] Fujimoto, M.Y. 1988, "*Differential rotation and elemental mixing in accreting stars*" Astronomy & Astrophys., **198**, 163

[12] Sparks, W. M., & Kutter, G. S. 1987, "*Nuclear runaways in a C/O white-Dwarf accriting H-riched material possessing angular momentum*", Astrophys. J., **321**, 394

[13] Kutter, G.S. & Sparks, W.M. 1989, "*Modeling the classical nova outburst. I - Exploring the physics of a new mechanism*" Astrophys. J., **340**, 985

[14] Woosley, S.E. 1986, "*In Nucleosynthesis and Chemical Evolution*", Eds. B. Hauck, A. Maeder, & G. Magnet (Savverng, Switzerland: Geneva Observatory Publication), p. 1

[15] Glasner, S.A., Livne, E., & Truran, J.W. 1997, "*Reactive flow in Nova outbursts*", Astrophys. J., **475**, 754

[16] Kercek, A., Hillebrandt, W., & Truran, J.W. 1998, "*Two-dimensional simulations of the thermonuclear runaway in an accreted atmosphere of a C+O White Dwarf* " Astronomy & Astrophys., **337**, 370

[17] Kercek, A., Hillebrandt, W., & Truran, J.W. 1999, "*Three-dimensional simulations of classical novae*", Astronomy & Astrophys., **345**, 831

[18] Rosner, R., Alexakis, A., Young, Y.-N., Truran, J. W., & Hillebrandt, W. 2001, "*On the C/O Enrichment of Nova Ejecta* " Astrophys. J. Letters, **562**, L177

[19] Alexakis, A., Young, Y.-N., & Rosner, R. 2002, "*Shear instability of fluid interfaces: Stability analysis* " Phys. Rev. E, 65, 026313

[20] Alexakis, A., Young, Y.-N., & Rosner, R. 2004, "*Weakly non-linear analysis of wind driven gravity waves*", J. Fluid Mech., **503**, 171

[21] Alexakis A., Calder A.C., Heger A., Brown E.F., Dursi L.J., Truran J.W., Rosner R., Lamb D.Q., Timmes F.X., Fryxell B., Zingale M., Ricker P.M., Olson K., 2004, "*On heavy element enrichment in Classical Novae*", Astrophys. J., **602**, 391

[22] Alexakis A., Dursi L.J., Calder A.C., Rosner R., Truran J.W., Fryxell B., Zingale M., Timmes F.X., Olson k., Ricker P., "*On the non-linear evolution of wind driven gravity waves*", submitted to Phys. Fluids (2004)

[23] Wind-Over-Wave Couplings: Perspectives and Prospects (The Institute of Mathematics and Its Applications Conference Series, New series, 69) by S. G. Sajjadi (Editor), N. H. Thomas (Editor), Julian C. R. Hunt (Editor)

[24] Helmholtz H., 1868 "*Ueber discontinuirliche Flüssigkeitsbewegungen*". Wissenschaftliche Abhandlungen **3**, 146–57.

[25] Lord Kelvin 1910 "*Influence of wind and capillarity on waves in water supposed frictionless*". Mathematical and Physical papers **iv** Hydrodynamics and general Dynamics. 76-85.

[26] Munk, W.H. 1947, "*A critical wind speed for air sea boundary processes*". J. Marine Research **6**, 203-18.

[27] Miles, J. 1957, *On the generation of surface waves by shear flows*", J. Fluid Mech., **3**, 185

[28] Lighthill, M.J. 1962 "*Physical interpretation of the mathematical theory of wave generation by wind*". J. Fluid Mech. **14**, 385–398.

[29] Chandrasekhar, S. 1962, "*Hydrodynamic and Hydromagnetic Stability*", (New York: Dover).

[30] Miles, J. 1959, "*On the generation of surface waves by shear flows*", J. Fluid Mech., **6**, 568.

[31] Miles, J. 1959, "*On the generation of surface waves by shear flows. Part 3. Kelvin-Helmholtz instability* ", J. Fluid Mech., **6**, 583.

[32] Miles, J. 1962, "*On the generation of surface waves by shear flows. Part 4.*", J. Fluid Mech., **13**, 433.

[33] Howard, L.N. 1961, "*Note on a paper of Miles, J.W.*", J. Fluid Mech., **10**, 509.

[34] Miles, J. 1993, "*Surface wave generation revisited*", J. Fluid Mech., **256**, 427.

[35] Davis, P.A., & Peltier, W.R. 1976, "*Resonant parallel shear instability in stably stratified planetary boundary layer*", J. Atmospheric Sci., **33**, 1287.

[36] Chimonas, G. 1970, "*Extension of Miles-Howard theorem to compressible fluids*", J. Fluid Mech.43, 833

[37] Lin, C.C. 1955, "*The Theory of Hydrodynamic Stability*", (Cambridge University Press).

[38] Drazin, P.G. & Reid, W.H. 1981, "*Hydrodynamic Stability*" (Cambidge University Press).

[39] Harris, J. A., Belcher, S. E., & Street, R. L. 1996 "*Linear dynamics of wind waves in coupled turbulent air-water flow. Part 2. Numerical model.*" J. Fluid Mech. **308**, 219.

[40] Belcher, S. E., Harris, J. A., & Street R. L. 1994 "*Linear dynamics of wind waves in coupled turbulent air-water flow. Part 1. Theory*", *J. Fluid Mech.* **271**, 119.

[41] Jenkins, A.D. 1992 "*A quasi-linear eddy-viscosity model for the flux of energy and momentum to wind waves using conservation-law equations in a curvilinear coordinate system*", *J. Phys. Oceanogr.* **22**, 843.

[42] Drazin, P. 1970 "*Kelvin-Helmholtz instability of finite amplitude*", J. Fluid Mech. **42**, 321.

[43] Blennerhassett, P. J. 1980 "*On the generation of waves by wind*, Phil. Trans. R. Soc. Lond. A**298**, 451.

[44] Akylas, T.R. 1982 "*A Nonlinear Theory for the generation of water waves by wind*", Stud. Appl. Math. **67**, 1.

[45] Benney, D., & Bergeron, Jr., R. F. 1969 "*A new class of nonlinear waves in parallel flows*". Stud. Appl. Math. **48**, 181.

[46] Benney, D., & Maslowe, S. 1975 "*The evolution in space and time of nonlinear waves in parallel shear flows*", Stud. Appl. Math. **54**, 181.

[47] Haberman, R. 1972 "*Critical Layers in Parallel Flows*", Stud. Appl. Math. **51**, 139.

[48] Churilov, S., & Shukhman, I. 1987 "*Nonlinear Stability of a Stratified Shear-Flow - A Viscous Critical Layer*", J. Fluid Mech. **180**, 1.

[49] Churilov, S., & Shukhman, I. 1996 "*The nonlinear critical layer resulting from the spatial or temporal evolution of weakly unstable disturbances in shear flows*", J. Fluid Mech. **318**, 189.

[50] Shukhman, I., & Churilov, S. 1997 "*The effect of slight stratification on the nonlinear spatial evolution of a weakly unstable wave in a free shear layer*", J. Fluid Mech. **343**, 197.

[51] Goldstein, M., & Hultgren, L. 1988 "*Nonlinear spatial evolution of an externally excited instability wave in a free shear layer*, J. Fluid Mech. **197**, 295.

[52] Warn, T., & Warn, H. 1978 "*The evolution of a nonlinear critical level*", Stud. Appl. Math. **59**, 37–71.

[53] Balmforth, N., & Piccolo, C. 2001 "*The onset of meandering in a barotropic jet*", J. Fluid Mech. **449**, 85–114.

[54] Reutov V. P. 1980 "*The plasma-hydrodynamic analogy and the nonlinear stage of instability of wind waves*". Izvestiya, Atmospheric and Oceanic Physics. **16**,12, 938–943.

[55] Caponi, E.A., Caponi, M.Z., Saffman, P.G., & Yuen, H.C. 1992 "*A simple model for the effect of water shear on the generation of waves by wind*". Proc. Roy. Soc. Lond. A**438**, 95-101.

[56] Maslowe, S. A., Benney D. J., & Mahoney, D. J. 1994 "*Wave Packet Critical Layers in Shear Flows*", Stud. Appl. Math **91**, 1–16.

[57] Oikawa, M., Chow, K., & Benney, D. J. 1987 "*The propagation of nonlinear wave packets in a shear flow with a free surface*", Stud. Appl. Math **76**, 69–92.

[58] Onishchenko, I.N., Linetskii, A.R., Matsiborko, N.G., Shapiro, V.D., & Shevchenko, V.I. 1970 "*Concerning the Nonlinear Theory of the Excitation of a monochromatic Plasma Wave by an Electron Beam*", Pis'ma v ZhETF. **12**, 8, 407–411.

[59] Balmforth, N. J., & Young, Y.-N. 2002 "*Stratified Kolmogorov flow*", J. Fluid Mech. **450**, 131–167.

[60] del Castillo-Negrete, D., & Morrison, P. 1993 "*Chaotic transport by Rossby waves in shear flow*", Phys. Fluids **5**, 948–965.

[61] Ngan, K., & Shepherd, T. G. 1997 "*Chaotic mixing and transport in Rossby-wave critical layers*", J. Fluid Mech. **334**, 315–351.

[62] *del Castillo-Negrete, D.* 2000 "*Self-consistent chaotic transport in fluids and plasmas*", Chaos **10**, 75–88.

[63] Boffetta, G., Lacorata, G., Radaelli G., & Vulpiani, A. 2001 "*Detecting barriers to transport: a review of different techniques*", Physica D **159**, 58–70.

[64] Latini, M., & Bernoff, A. 2001 "*Transient anomalous diffusion in Poiseuille flow*", J. Fluid Mech. **441**, 399–411.

[65] Lingevitch, J. F., & Bernoff, A. J. 1994 "*Advection of a passive scalar by a vortex couple in the small diffusion limit*", J. Fluid Mech. **270**, 219–249.

[66] Venkataramani, C., Antonsen, M., & Ott, E. 1998 "*Anomolous diffusion in bounded temporally irregular flows*", Physica D **112**, 412–440.

[67] Cheung, T. K., & Street, R. L. 1987 "*The turbulent layer in the water at an air-water interface*", J. Fluid Mech. **194**, 133–151.

[68] Simmen, J. A., & Saffman, P. G. 1985 "*Steady deap-water waves on a linear shear current*", Stud. Appl. Math. **73**, 35–57.

[69] Saffman, P. G., & Yuen, H. C. 1982 "*Finite amplitude interfacial waves in the presence of a current*", J. Fluid Mech. **123**, 389–410.

[70] Leighton R., in preparation, 2004.

[71] Belcher S.E. & Hunt J.C.R. 1998 "*Turbulent flow over hills and waves*", Annu. Rev. Fluid Mech. **30**, 507–538.

[72] Sullivan P.S. & McWilliams J.C. 2002 "*Turbulent flow over water waves in the presence of stratification*", Phys. Fluids **14**, 1182–1195.

[73] Fryxell, B., et al. 2000, "*Flash: an adaptive mesh hydrodynamics code for modeling astrophysical thermonuclear flashes*". Astrophys. J. **131**, 273.

[74] Calder A. C., Curtis B.C., Dursi L.J., Fryxell B., Henry G., MacNeice P., Olson K., Ricker P., Rosner R., Timmes F.X., Tufo H.M., Truran J.W., Zingale M. 2000, "*High Performance Reactive Fluid Flow Simulations Using Adaptive Mesh Refinement on Thousands of Processors*", in Proc. Supercomputing, (IEEE Computer Soc.). `http://sc2000.org/proceedings/`

[75] Calder A.C., Fryxell B., Plewa T., Rosner R., Dursi L.J., Weirs V.G., Dupont T., Robey H.F., Kane J.O., Remington B.A., Drake R.P., Dimonte G., Zingale M., Timmes F.X., Olson K., Ricker P., MacNeice P., Tufo H.M. 2002, "*On validating an astrophysical simulation code*", Astrophys. J. **143** 201–229.

[76] Zingale M., Dursi L.J., Zuhone J., Calder A.C., Fryxell B., Plewa T., Truran J.W., Caceres A., Olson K., Ricker P.M., Riley K., Rosner R., Siegel A., Timmes F.X., and Vladimirova N. 2002 "*Mapping initial hydrostatic models in Godunov codes*", Astrophys. J. Suppl., **143** 539–565.

[77] Michell, J.H. 1893 "*On the highest gravity waves on deep water*", Phil. Mag.(5)**36**, 430.

[78] Williams J.M. 1981 "*Limiting gravity waves in water of finite depth*", Phil. Trans. R. Soc. Lond. A**302**, 139–188.

[79] Longuet-Higgins, M.S. 1997, "*Progress Toward understanding how waves break*", Proc 21st Symp. on Naval Hydrodynamics (Cambridge, Mass) U.S. Govt. Printing Off., 7–27.

[80] Longuet-Higgins, M.S. & Cokelet E.D. 1997, "*The deformation of steep surface waves on water: II Growth of normal modes instabilities*", Proc. R. Soc. Lond.A **364**, 1–28.

[81] Longuet-Higgins, M.S. & Dommermuth, D.G. 1997, "*Crest instabilities of gravity waves .3. Nonlinear development and breaking*", J. Fluid Mech. **336**, 33–50.

[82] MacNeice, P., Olson, K. M., Mobarry, C., de Fainchtein, R., & Packer, C. 1999, NASA Technical Report CR-1999-209483.

[83] MacNeice, P., Olson, K. M., Mobarry, C., de Fainchtein, R., & Packer, C. 2000, "*PARAMESH: A parallel adaptive mesh refinement community toolkit*", Comput. Phys. Commun., 126, 330.

[84] Dimonte, G., et al. 2004, "*A comparative study of the turbulent Rayleigh-Taylor (RT) instability using high-resolution 3D numerical simulations: The Alpha-Group collaboration*", to appear in Phys. Fluids.

[85] Dimonte, G., & Schneider, M. 2000, "*Density ratio dependence of Rayleigh-Taylor mixing for sustained and impulsive acceleration histories*", Phys. Fluids A, 12, 304.

[86] Weaver, T. A., Zimmerman, B.A., & Woosley, S.E. 1978, "*Presupernova evolution of massive stars*", Astrophys. J., **225**, 1021

[87] Rauscher, T., Heger, A., Hoffman, R. D., Woosley, S. E. 2002, "*Nucleosynthesis in Massive Stars with Improved Nuclear and Stellar Physics*", Astrophys. J., **576**, 323

[88] Fujimoto, M. Y. 1982, "*A theory of hydrogen shell flashes on accreting white dwarfs. I - Their progress and the expansion of the envelope. II - The stable shell burning and the recurrence period of shell flashes*", Astrophys. J., **257**, 752

[89] Fujimoto, M. Y. 1982, "*A Theory of Hydrogen Shell Flashes on Accreting White Dwarfs - Part Two - the Stable Shell Burning and the Recurrence Period of Shell Flashes*", Astrophys. J., **257**, 767

[90] Popham, R. & Narayan, R. 1995, "*Accretion disk boundary layers in cataclysmic variables. 1: Optically thick boundary layers* ", Astrophys. J., **442**, 337

[91] Olver, F. 1997 "*Asymptotics and special functions*", A. K. Peters.